Development of a Semi-Automated ZLC System for Rapid Screening of Adsorbents for Carbon Capture

Xiayi Hu

For the Degree of Doctor of Philosophy
School of Engineering
University of Edinburgh

February 2012

Dislaimer

This thesis was prepared as an account of work sponsored by an agency of the United State Government. Neither the United States Government nor any agency thereof, nor any of their employees, makes any warranty, express or implied, or assumes any legal liability or responsibility for the accuracy, completeness, or usefulness of any information, apparatus, product, or process disclosed, or represents that its use would not infringe privately owned rights. Reference herein to any specific commercial product, process, or service by trade name, trademark, manufacturer, or otherwise does not necessarily constitute or imply its endorsement, recommendation, or favoring by the United States Government or any agency thereof. The views and opinions of authors expressed herein do not necessarily state or reflect those of the United States Government or any agency thereof.

ABSTRACT

In this dissertation a novel ZLC setup has been developed as part of a DOE-funded grant in collaboration with UOP, to provide rapid screening of novel adsorbent materials for carbon capture (CC). The key features of the new apparatus that was developed are: the use of 5-15 mg of sample and a dual detector system – a thermal conductivity detector (TCD) for single component measurements and a mass spectrometer for studying the influence of water and other impurities. Improvements over previous ZLC apparatuses include:

1. Extension to lower flowrates, i.e. < 3 cc/min, thereby reducing consumption of gases and allowing to run the system under equilibrium control conditions;
2. A new gas dosing system that allows the use of vapours without a chilled bath and bubbler system;
3. A new switching valve system, which prevents leakages;
4. Automated series of experiments, which are implemented using Labview.

The new ZLC technique was first applied to provide rapid screening capacity ranking of more than 15 MOF materials from the open literature and three typical zeolites for carbon capture. At the point of interest for flue gas application (38°C, 0.1 bar CO_2 partial pressure), Mg/DOBDC was found to outperform significantly all other MOFs and benchmark zeolites at the point of interest in low pressure physisorption of CO_2. The ZLC was also used to investigate steaming on Ni/DOBDC as well as see the effect of forming powders into pellets.

The new ZLC system also enables one to measure micropore and macropore diffusivity. Experiments were carried out on both powders and pellets of typical MOFs and zeolites. For Co/DOBDC crystals, since the system is close to equilibrium control even at the highest flow rate, a low limit of diffusivity can be estimated. For all the formed samples of Ni/DOBDC and 13X pellets, the results indicate that mass transfer is controlled by macropore diffusion. The ZLC technique can also estimate realistic void fraction and tortuosity values for the pellets.

The new ZLC technique was applied to study the stability on the MOF M/DOBDC series. The preliminary water tests showed that all M/DOBDC samples are highly hydrophilic. Therefore in a process design using these MOFs, we conclude that there is a needs to use a guard bed layer to adsorb water or use a gas drying unit before the CO_2 capture section of the plant.

The ZLC system appears to be extremely useful to accelerate the deactivation of samples due to SO_X and NO_X impurities. The key advantages are based on the fact that the treatment can be repeated in situ, in a relatively simple way using a very small sample. The results show that in the presence of impurities and water the candidate MOFs undergo significant deactivation. The Ni based material shows the best resistance to degradation. This result indicates further that there would be a need for a drying unit prior to the carbon capture adsorption process.

ACKNOWLEDGEMENTS

I would like to give my deepest gratitude to my adviser, Prof. Stefano Brandani, for his patience, guidance, encouragement, and tremendous support during my Ph.D. degree studies. I really appreciate his patience when helping me with my mistakes and his encouragement toward my progress. Working with him was indeed a wonderful and learning experience, which I thoroughly enjoyed. I am also grateful to all of the members of the carbon capture group for their company, help, and memorable friendships.

I gratefully acknowledge the U.S. Department of Energy and the National Energy Technology Laboratory for providing funds for this research led by UOP (Award No. DEFC26- 07NT43092). In particular I would like to thank the project collaborators from UOP: Dr. Richard Willis for his efforts in coordinating this project and for the useful discussions during the teleconference meetings and as part of his visit to Edinburgh University; I am also very grateful to Dr. Annabelle I. Benin for supplying the MOF adsorbent materials and for characterising the samples after the ZLC stability experiments. In addition I would also like to thank the University of Michigan (Prof. Adam Matzger) for providing materials; Northwestern University (Prof. Randall Snurr) and Vanderbilt University (Prof. Douglas LeVan and Dr. Jian Liu) for their friendly sharing of information and helpful suggestions during the whole project.

I would like to thank the workshop technicians for their help during the ZLC system setup and development work.

Finally, I want to thank my parents for their unconditional love and encouragement, thank you.

TABLE OF CONTENTS

1. INTRODUCTION 1

1.1 Introduction of CCS 1

1.2 Structure of the dissertation 8

2. ADSORBENTS FOR CARBON CAPTURE 12

2.1 Introduction of adsorbents 12

2.2 Zeolites 13

2.3 Amine supported adsorbents 18

2.3.1 Carbon-based adsorbent 18

2.3.2 Mesoporous silica 19

2.4 MOFs 19

2.5 Conclusions 29

_Toc319872289

3. THEORY OF THE ZERO LENGTH COLUMN (ZLC) TECHNIQUE 30

3.1 Introduction of the zero length column (ZLC) technique 30

3.2 Mathematical models of the ZLC 32

3.3 Equilibrium control 36

3.3.1 Linear equilibrium 37

3.3.2 Langmuir equilibrium 39

3.3.3 Flowrate correction 40

3.3.4 Analysis as breakthrough curves 41

3.4 Kinetic control 44

3.4.1 Micropore diffusion control 44

3.4.2 Macropore diffusion control 47

4. ZLC SYSTEM 49

4.1 Introduction 49

4.2 Traditional ZLC system 50

4.3 Semi-automated ZLC system set up 51

4.4 Dosing system development 55

4.5 Procedure of preparing the mixture 58

4.6 Gas flow and ZLC oven development 60

4.7 Semi-automated control system 63

4.8 Procedure of packing a ZLC column and typical ZLC experiment 68

4.8.1 ZLC column packing 68

4.8.2 ZLC experimental procedures 70

4.9 ZLC system modification during project 72

5. RAPID RANKING OF ADSORPTION CAPACITY 77

5.1 Introduction 77

5.2 Adsorbent synthesis 78

5.3 ZLC ranking measurements conditions 81

5.4 Results and discussion 83

5.4.1 Ranking of materials 83

5.4.2 Heat of adsorption at zero loading on typical adsorbents 98

5.4.3 Ni/DOBDC MOFs ranking after modification 100

5.5 Conclusions 104

6. STUDY OF DIFFUSION BEHAVIOURS OF CO_2 IN NOVEL ADSORBENTS 106

6.1 Introduction 106

6.2 Co/DOBDC Powder 107

6.3 Ni/DOBDC compressed pellets 111

6.4 Ni/DOBDC extrudate 121

6.5 13X zeolite commercial pellet 127

6.6 Conclusion 131

7. SCREENING STABILITY MEASUREMENTS OF NOVEL ADSORBENTS 132

7.1 Introduction 132

7.2 Experiment 133

7.2.1 Adsorbent 133

7.2.2 Experimental setup 134

7.3 Preliminary water experiment 136

7.4 Stability test 141

7.4.1 Water stability 141

7.4.2 Water and CO_2 stability 144

7.4.3 ‘Dry’ flue gas stability 147

7.4.4 Wet flue gas stability 149

7.4.5 SO_2 analysis 154

7.4.6 XRD characterisation 158

7.5 Conclusion 158

8. CONCLUSIONS AND FURTHER WORK 160

References 164

Nomenclature 174

CHAPTER 1

1. INTRODUCTION

1.1 Introduction of carbon capture and storage (CCS)

Yu et al. [1] have shown that eleven out of twelve years (1995–2006) rank among the twelve warmest years in the instrumental record of global surface temperature (since 1850). The linear warming trend over the 50 years from 1956 to 2004 (0.10 to 0.16 °C per decade) is nearly twice that for the 100 years from 1906 to 2004 (Figure 1.1). Carbon dioxide is the most important greenhouse gas leading to global warming. There is an undeniable correlation between the observed temperature rises with enhanced atmospheric CO_2 concentrations. Atmospheric CO_2 concentrations have indeed increased by almost 100 ppm since their pre-industrial level, reaching 384

ppm in 2007. Annual emissions of CO_2 increased between 1970 and 2004 by about 80%, from 21 to 38 Gigatonnes (Gt), which represents 77% of total greenhouse gas emissions in 2004. The trend is shown in Figure 1.1, taken from the IPCC 2007 report [2], and these increasing emissions have become worldwide concerns.

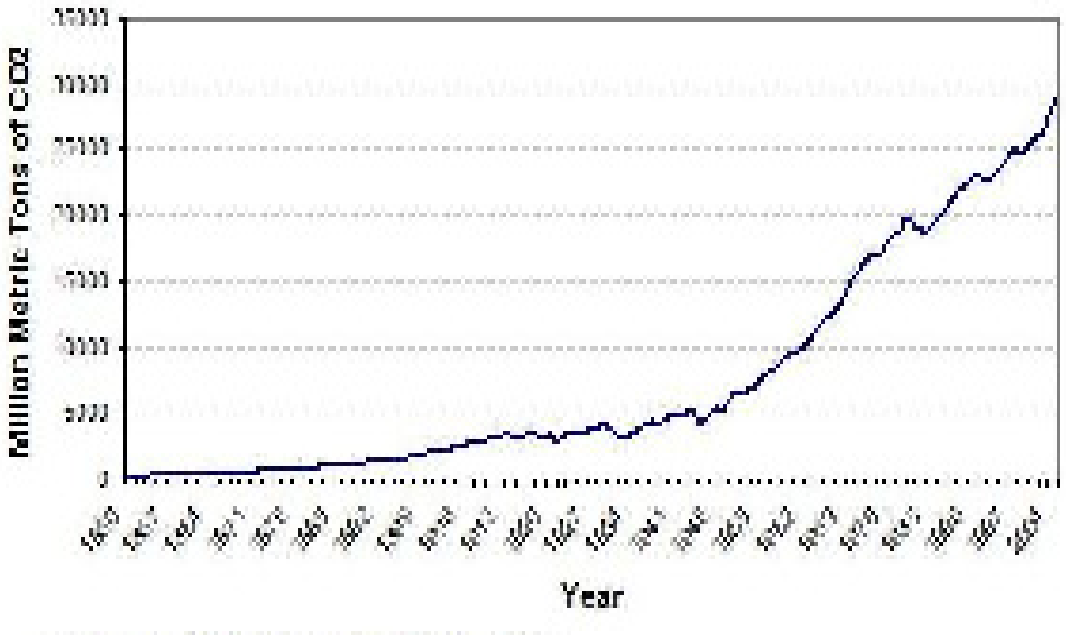

Figure 1.1 CO_2 emission per millions of metric tons from 1850 to 2004 [2].

The unpublished estimates on the global carbon dioxide (CO_2) emissions for 2010 do not make good news. Between 2003 and 2008, emissions have been rising at a rate faster than anytime in history. However, the global recession slowed the growth of emissions considerably, and in fact they actually declined slightly from 29.4 Gt CO_2 in 2008, to 29 Gt in 2009. But 2010 saw the largest single-year increase in global human CO_2 emissions from energy (fossil fuels), increasing 1.6 Gt from 2009, to

30.6 Gt. As can be seen in Figure 1.2, in 2009 we had dropped into the middle of the IPCC Special Report on Emissions Scenarios (SRES) scenarios, but the 2010 increase has come back to the worst case scenarios once again [3].

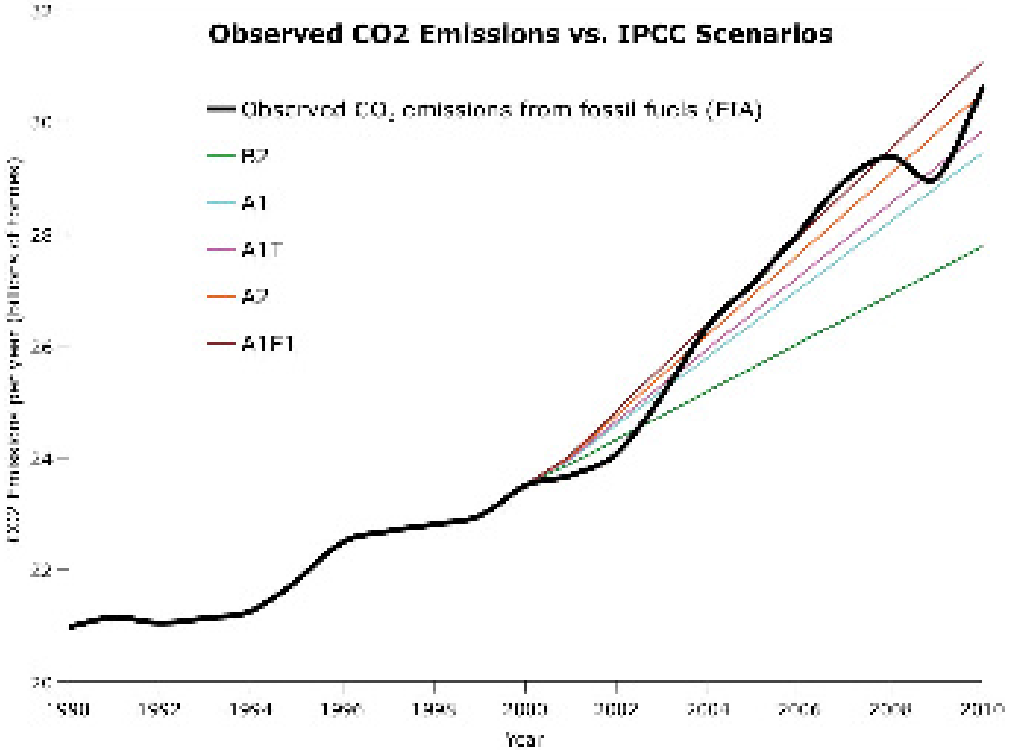

Figure 1.2 US Energy Information Administration (EIA) global human CO_2 annual emissions from fossil fuels estimates vs. IPCC SRES scenario projections. The IPCC Scenarios are based on observed CO_2 emissions until 2000, at which point the projections take effect [3].

In order to understand the importance of reducing CO_2 levels, it is essential to recognise the sources and the magnitude of CO_2 emissions at the present time. From Figure 1.3 it can clearly be seen that CO_2 emissions are mainly caused by the burning of fossil fuels (56.6%) to meet worldwide energy demands. However, there is no new

energy resource that can fully replace fossil fuels. A forecast energy report shows that for the period of 2004–2030 the global primary energy demand will rise by 53%, leading to a 55% increase in global carbon dioxide emissions related to energy, and the fossil fuels will be the dominating source of worldwide energy supply, meeting 83% of the increase in energy demand; and emissions from power generation will account for 44% of global energy-related emissions by 2030, as demand for electricity rises [4].

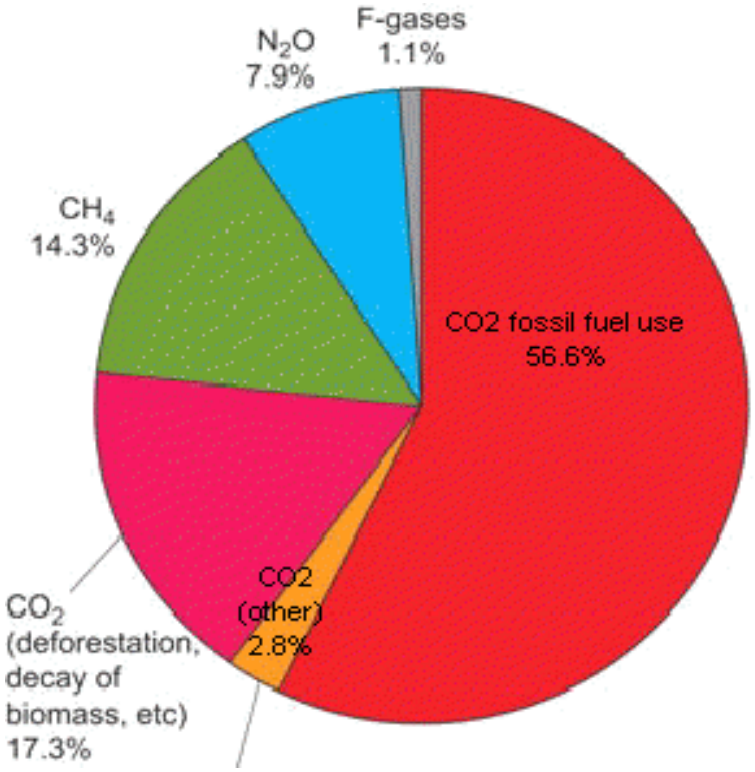

Figure.1.3 CO_2 emission chart, showing the emissions primarily from burning fossil fuels [2].

As a result, achieving reduction in emissions without compromising our economic growth, national security and living standards, has become an important issue.

Carbon dioxide capture and storage (CCS) which involves separation, liquefaction and storage of CO_2 to reduce emissions on a large scale is an effective technology, which plays a significant role in mitigating the effect of CO_2 on climate change. The U.S. Department of Energy (DOE) issued a carbon sequestration program in 2009 aiming to achieve 90% CO_2 capture at an increase in the cost of electricity of no more than 35% by 2020 [5]. Coal-fired power plants produced about one third of CO_2 emissions and as such are attractive targets for capture technologies. Normally the power plants produce flue gas at 1 bar with a CO_2 concentration of about 10-16% in ambient conditions [6]. There are three kinds of capture technologies that have been developed and tested, including post combustion, pre-combustion and oxyfuel combustion [7].

1. Post-combustion capture: to capture CO_2 in the exhaust gases once the fuel has been completely burnt with air.

2. Oxy-fuel combustion: involves combustion in O_2 with recycling of exhaust gases plus separation of mainly H_2O and CO_2 mixture.

3. Pre-combustion capture: to capture CO_2 in a synthesis gas after conversion of CO into CO_2.

Current commercial carbon capture technology is based on using chemisorption by liquid alkaline solutions (*e.g.* amine), which is an effective technology to remove CO_2 from flue gas. Figure 1.4 shows CO_2 post-combustion capture at a plant in

Malaysia funded by of Mitsubishi Heavy Industries. This plant employs a chemical absorption process to separate 0.2 Mt CO_2 per year from the flue gas stream of a gas-fired power plant for urea production. However, the degradation of chemical solvent and the high energy requirement in the regeneration process and the corrosion in the system motivates alternative approaches [8].

Figure 1.4 CO_2 post-combustion capture at a plant in Malaysia. This plant employs a chemical absorption process to separate 0.2 Mt CO_2 per year from the flue gas stream of a gas-fired power plant for urea production [9].

Given the glaring disadvantages of the conventional methods, there is room for alternative methods that can bring about a step-change in the efficiency of CO_2 capture. These limitations have prompted significant investigation of physisorption for CO_2 separation, which requires a porous material with high CO_2 affinity and

capacity [10, 11]. Adsorption processes for gas separation via selective adsorption on solid media are also well-known, and are commonly applied in industrial separation processes, such as air separation for O_2 and N_2, and dehydration and sweetening of natural gas [12, 13]. The adsorbents can operate via weak physisorption processes or strong chemisorption interactions. Solid adsorbents are typically employed in cyclic, multi-module processes of adsorption and desorption, with desorption induced by pressure (PSA), vacuum (VSA) or temperature swing (TSA) and these are very promising for separation and recovery processes. PSA is based upon a reduction in the partial pressure, which gives the driving force to desorb; while TSA is based on the principle of temperature change in an adsorbent bed, and hence the exothermic character of adsorption is the driving force for desorption. Compared to TSA, the advantages of PSA are that the energy requirement is lower and its cycle times are significantly shorter. Some solid CO_2 adsorbents have been tested in post combustion and pre-combustion capture processes [10, 14]. Unlike liquid adsorbents, solid adsorbents can be used over a wider temperature range, yield less waste during cycling, and the spent solid adsorbents can be disposed of without undue environmental precautions [15]. Adsorption can be considered as an application to capture CO_2 due its lower energy requirement.

Since adsorption is a process where molecules from the gas phase bind to a condensed layer or a solid surface (adsorbent) in the design of an adsorption-based separation process, the choice of the adsorbent is the most crucial design consideration [16-18].

In this chapter the global warming situation was reviewed and the carbon capture process, as well as the current capture technology and the limitations were introduced. The adsorption process can be a potential technology to capture CO_2 from coal fired power plants, but the choice of adsorbents is the crucial consideration.

1.2 Structure of the dissertation

The project was funded by the US Department of Energy, in collaboration with UOP LLC, a Honeywell Company, Vanderbilt University (VU), University of Michigan (UM), Northwestern University (NU) and University of Edinburgh (UE) to develop novel microporous metal organic frameworks (MOFs) for the removal of CO_2 from post-combustion coal-fired power plant flue gas. The University of Michigan and UOP focused on synthesis of MOFs, the organic components associated with the production of MOFs and materials development and manufacturing; Northwestern University worked on molecular modelling of the adsorption; Vanderbilt University and the University of Edinburgh characterised the adsorption properties of the materials. This dissertation presents the work of developing a semi-automated ZLC system for characterising novel adsorbents.

In chapter 2, the main classes of adsorbents are introduced. There are an unlimited number of possible MOF adsorbent structures that can be prepared, and a good candidate for carbon capture should have desirable characteristics, such as a low energy requirement for regeneration, good thermal stability, tolerance to

contaminants, attrition resistance, and low cost. Therefore there is a need to develop novel laboratory measurements. An experimental technique should allow us to:

- Rank CO_2 capacity of materials rapidly
- Use only small samples
- Interpret the results easily
- Determine kinetics
- Test the materials with water
- Test the materials with SO_x and NO_x

A properly designed ZLC system can deliver all of these requirements.

In Chapter 3, the basic theory underlying the ZLC method is summarized, as well as some literature research of ZLC model development and some other studies accomplished using the ZLC technique.

In Chapter 4, the semi-automated ZLC system is presented as well as the development of the technique. The key features for the applications are: the use of 5-15 mg of sample and a dual detector system – a thermal conductivity detector (TCD) for single component measurements and a mass spectrometer for studying the influence of water and other impurities. Improvements over previous ZLC apparatuses include: (1) extension to lower flowrates, i.e. < 3 cc/min, thereby reducing consumption of gases; (2) a new gas dosing system that allows the use of vapours without a chilled bath and bubbler system; (3) the new switching valve,

which prevents leakages; and (4) automated series experiments, which are compatible with the Labview programme language.

In Chapter 5, the new ZLC setup has been applied to provide rapid screening of novel adsorbent materials for carbon capture (CC). ZLC measurements have been carried out on zeolites and metal-organic frameworks (MOFs) at a point of interest for flue gas application (38°C, 0.1 bar CO_2 partial pressure). Mg/DOBDC significantly outperforms all other MOFs and benchmark zeolite at low pressure physisorption of CO_2; these have also confirmed the literature data, showing that the ZLC system is an effective method of ranking and selecting adsorbents. Additionally, the heat of adsorption of the two best MOFs and a reference zeolite are calculated and the different types of Ni/DOBDC sample are compared.

Chapter 6 focuses on applying the semi-automated ZLC technique to investigate the diffusion behaviour of CO_2 in a sample of metal organic frameworks: Co/DOBDC powder and Ni/DOBDC compressed pellets and extrudate and commercial 13X zeolite pellet, which have potential uses in carbon capture because of their very high CO_2 adsorption capacity at point of interest pressure and temperature, i.e. flue gas from power plant (38 ºC, 0.1bar CO_2 partial pressure) as well as the diffusion of molecules in their pores. The diffusivity range is estimated on Co/DOBDC crystals and for Ni/DOBDC MOFs; macropore diffusion control is confirmed in both the Ni/DOBDC compressed pellet and extrudate. A reasonable void fraction and tortuosity are estimated. The macropore diffusion control is also confirmed on the 13X pellet sample.

In Chapter 7, the semi-automated ZLC technique is used to study the stability of the novel adsorbents against water and impurities, i.e. SO_x and NO_x. The tests are carried out on the most promising materials of the M/DOBDC (M = Co, Ni, Mg) MOFs, as well as comparison with the 13X zeolite. The experimental results indicate that even if the DOBDC family shows high CO_2 adsorption capacity at low partial pressure at ambient conditions, purities like SO_x and NO_x can have some affect on their structure, and 13X is a promising material for separation of CO_2 from flue gases. The present work not only provided useful information for the development of MOFs, but it also showed that the new ZLC system appears to be a useful technique when trying to accelerate the deactivation of the samples due to SO_x and NO_x impurities.

A general conclusion of the work and the possible future developments is presented in Chapter 8.

CHAPTER 2

2. ADSORBENTS FOR CARBON CAPTURE

2.1 Introduction of adsorbents

The main classes of adsorbents for CO_2 capture include zeolites, activated carbons, calcium oxides, hydrotalcites, supported amines and metal organic frameworks (MOFs). The present project is focusing on developing metal organic frameworks (MOFS), and also some zeolites were studied as reference materials.

There are many available adsorbents that can recover CO_2. The quality or utility of these adsorbents can be described by several important factors. In general, rapid adsorption and desorption kinetics, high adsorption capacity, good regenerability and stability, and a wide, yet tunable range of operating conditions might define an ideal, hypothetical adsorbent. Although the best outcome is to develop an ideal adsorbent, in reality no single ideal adsorbent is likely to be invented. Rather, weaknesses and strengths of each adsorbent type must be considered in the context of a practical adsorption process for effective CO_2 separation. Ultimately, winning adsorbents will be those that effectively work within a practical and efficient CO_2 separation process.

2.2 Zeolites

Zeolites are crystalline aluminosilicalites which can be found in nature or produced synthetically. In zeolites, the framework consists of interlocking tetrahedrons of SiO_4 and AlO_4 joined together in various regular arrangements through shared oxygen atoms. They have open crystal lattices containing pores with molecular dimensions, into which molecules can penetrate. The negative charge created by the substitution of an AlO_4 tetrahedron for a SiO_4 tetrahedron is balanced by exchangeable cations (*e.g.*, Na^+, K^+, Ca^{2+}, Mg^{2+}), which are located in the channels and cavities throughout the structure.

The adsorption and gas separation properties of zeolites are dependent on the size, charge density, and distribution of these cations in the structure [19]. Today there are more than 170 topologies indexed by the International Zeolite Association (IZA) [20].

The CO_2 adsorption properties of zeolites are also influenced by the porous characteristics of the framework. From a comparative study of the CO_2 adsorption capacities on a number of commercially available zeolites, the high CO_2 adsorption capacities were observed in LTA and FAU zeolite , UOP is one of the largest zeolite manufactures in the world and has supplied the zeolite samples used in this study. Figure 2.1 shows the structure of Zeolite A (Linde Type A). It has a 3-dimensional pore structure with pores running perpendicular to each other in the x, y, and z planes. The pore diameter is defined by an eight member oxygen ring and is small at 4.2Å. This leads into a larger cavity of minimum free diameter 11.4Å. The cavity is surrounded by eight sodalite cages (truncated octahedra) connected by their square faces in a cubic structure. The unit cell is cubic (a = 24.61Å) with Fm-3c symmetry. Zeolite A has a void volume fraction of 0.47, with a Si/Al ratio of 1.0. It thermally decomposes at 700ºC [20].

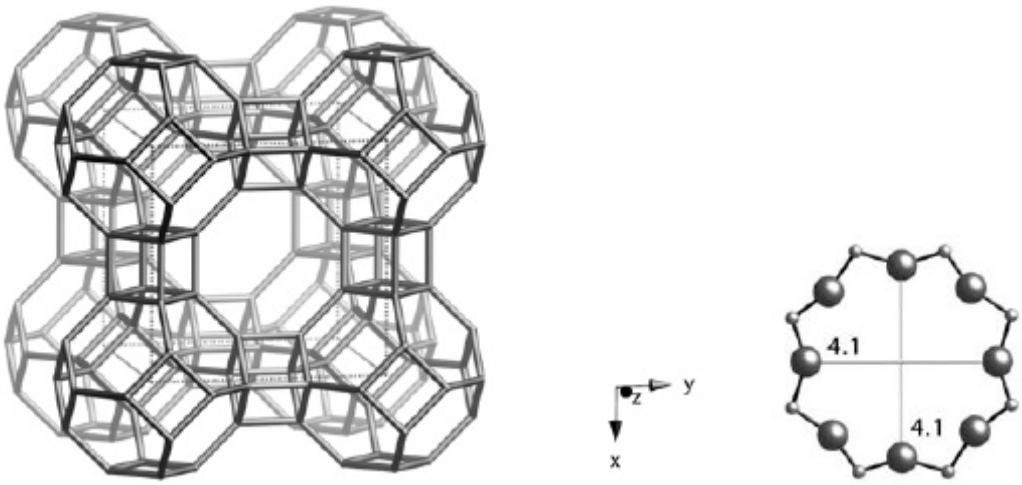

Figure 2.1 Framework of Zeolite A Framework (left) and 8-membered oxygen rings of free diameter 4.1A (right) [20].

Figure 2.2 shows a typical topology of FAU (faujasite) zeolite. Zeolite X and Y exhibits the FAU structure. It has a 3-dimensional pore structure with pores running perpendicular to each other in the x, y, and z planes similar to LTA. The pore diameter is large at 7.4Å since the aperture is defined by a 12 member oxygen ring, and leads into a larger cavity of diameter 12Å. The cavity is surrounded by ten sodalite cages (truncated octahedra) connected on their hexagonal faces. The unit cell is cubic (a = 24.7Å) with Fd-3m symmetry. The X and Y structures differ only in the Si/Al ratio [20].

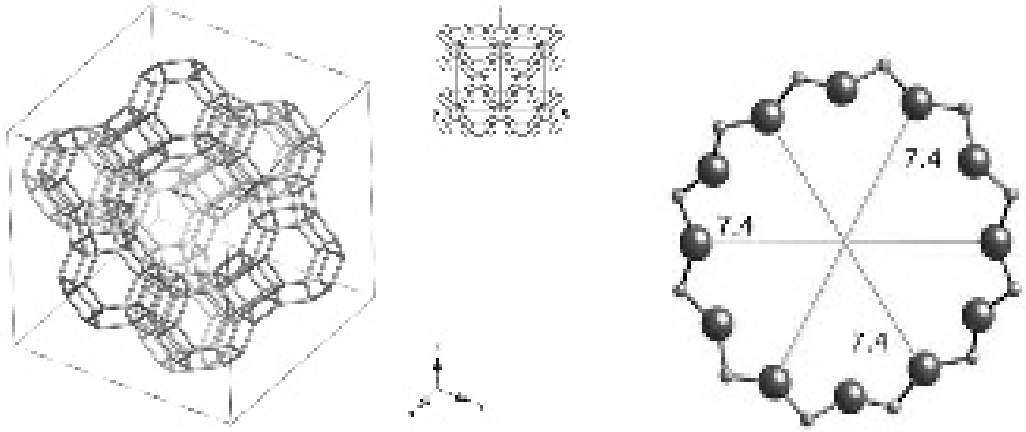

Figure 2.2 Framework of 13X Zeolite (left) and 12-membered oxygen rings of free diameter 7.4 A (right) [20].

The structure of zeolites enables them to adsorb several gas molecules, including acidic gas molecules such as CO_2. The CO_2 adsorption mechanism on zeolites has

been investigated and revealed that the physisorption of CO_2 occurs with CO_2 in a linear orientation by an ion–dipole interaction [21].

$$(\text{metal ion})^{x+} \cdots\cdots {}^{\delta-}O{=}C{=}O^{\delta+}$$

Figure 2.3 the physisorption of CO_2 occurs with CO_2 in a linear orientation by an ion–dipole interaction [21].

Generally speaking, separation of CO_2 by zeolites depends on three factors: structure and composition of the framework, cationic form, and zeolite purity [22]. A number of zeolites, especially with highly crystalline and high surface area, as well as three-dimensional pore structures, have been investigated, including zeolite X, Y, A, β, ZSM, CHA and natural zeolites (*e.g.* ZAPS, ZNT, ZN-19) [23]. Table 1.1 presents the varying values of CO_2 adsorption capacities of zeolite. These results have employed different experimental methods.

Harlick and Tezel [24] carried out an experimental screening study of the selection of a suitable adsorbent for CO_2 removal from flue gas (mixture of CO_2 and N_2), the limiting heats of adsorption, and Henry's Law constants for CO_2 with a N_2 carrier of various synthetic zeolite adsorbents, including 13X, NaY, HiSiv-1000 (a commercial NaY zeolite with a SiO_2/Al_2O_3 ratio >20), HY-5, ZSM-5-30 (MFI), and HiSiv-3000 (a commercial zeolite based on the ZSM-5 structure with a large SiO_2/Al_2O_3 ratio >1000), and concluded that the most important adsorbent characteristics are a near linear CO_2 isotherm and a low SiO_2/Al_2O_3 ratio with cations that have a strong

electrostatic interaction with CO_2. Siriwardane [25] reported the CO_2 adsorption capacity for zeolites 13X and 4A at ambient temperature and 1 atm of CO_2 partial pressure and found that the adsorption capacity of CO_2 for molecular sieve 13X was higher than that for molecular sieve 4A at all pressure ranges. Siriwardane [26] also found the highest CO_2 adsorption capacities in zeolite 13X, the material with the largest pore diameter and volume among commercially available zeolites including 4A, 5A (both LTA), 13X, APG-II, and WE-G 592 (all FAU). Inui [27] investigated the relationships between properties of zeolites and their adsorption-desorption behaviours for CO_2 and claimed that CHA and 13X were the most appropriate for CO_2 separation among the zeolites studied. Merel [28] studied the CO_2 capture properties of zeolites 13X and 5A by indirect thermal swing adsorption, and found 5A to give the best performance in various operating conditions including one with nitrogen purge during desorption. Calleja [29] reported that the adsorption capacity of the adsorbent for polar molecules (*e.g.* carbon dioxide and ethylene) increases as the Si/Al ratio decreases due to the higher surface heterogeneity and the stronger electrostatic field inside the pores of the zeolite.

In terms of practical applications, flue gas contains 1-5% moisture; it may compete with CO_2 for the active adsorption sites, so is a challenge to the zeolite adsorbent. Gallei and Stumpf [30] have studied the adsorption of carbon dioxide and the co-adsorption of carbon dioxide and water on CaY- and NiY-zeolite by means of *in situ* infrared spectroscopy. The results show that the physical adsorption of carbon dioxide on CaY- and NiY-zeolite is very limited in the presence of water, because water is preferentially adsorbed onto these surfaces. Brandani and Ruthven [12, 31] using the ZLC technique observed that the presence of water in the mixture has a

strong effect on the CO_2 adsorption capacity on type X zeolites. Rege and Yang [12, 31] found similar affect on X zeolite by FTIR technique. In addition, H_2O may have a detrimental effect on the stability of zeolite frameworks. In the presence of CO_2, the acidic conditions may cause partial or total destruction of the zeolite structure. Ertan and Çakicioğlu-Özkan [32] studied CO_2 adsorption on acid-treated zeolites (HCl, HNO_3, H_2SO_4, H_3PO_4), and found that their CO_2 adsorption capacities decreased after the acid treatment.

2.3 Amine supported adsorbents

2.3.1 Carbon-based adsorbent

Carbon-based adsorbents are low cost, high surface area, high amenability to pore structure modification and surface functionalization, and relative ease of regeneration. Looking at the CO_2 adsorption capacity they are generally characterized by lower values than Zeolites at low CO_2 partial pressure but higher in high pressure region [23]. One of the most interesting research issue in carbon materials is the attempt of increase the adsorption properties by the introduction different surface functional groups. Adding basic chemical groups has simultaneously the advantage of an increase of the CO_2 affinity and the disadvantage of likely decrease of the available surface area for adsorption. Modification of the surface functionalities of activated carbons has been pursued either by removing the oxygen-containing groups with heat

treatment at temperatures above 973 K in inert atmosphere, or by replacing the surface groups with other constituents such as amines [33].

2.3.2 Mesoporous silica

The properties of mesoporous silica can be easily tailored by surface modification to prepare materials with desired properties and applications, and the high surface areas of mesoporous silicas (500 to 1500 $m^2\ g^{-1}$) provide an open, accessible backbone for the stabilization of a large number of active adsorption sites [34]. As a resuilts, amine active sites bonded on the surface of mesoporous solid can capture carbon dioxide through the formation of carbamates and carbonates, resembling the technological process of CO_2 scrubbing by liquid alkanolamines [35]. The new amine modified mesoporous solid sorbents could take advantage of high selectivity to carbon dioxide together with high gas flux and mass transfer within mesoporous solid. The advantage of having large and uniform pores is that it is possible to introduce surface modification avoiding any steric hindrance of the adsorption sites.

2.4 MOFs

Recently, metal organic frameworks (MOFs) constructed from organic electron donor linkers and metal cations, are a new family of porous materials [36, 37]. These kinds of crystalline materials have received much attention due to their extremely high surface areas, controllable pore structures, and versatile chemical compositions [38]. MOFs are crystalline materials with structures based on classical coordination

bonds between metal cations and electron donors. Their rigid pores do not collapse upon removal of solvent or other “guest” molecules occupying the pores following synthesis. The presence of both inorganic and organic components enables both the pore size and chemical environment to be tailored to achieve specific properties. One type of MOF structure (indium soc-MOF) is shown in Figure 2.4, structure of MOF-5 derivatives called IRMOFs (Isoreticular Metal Organic Frameworks) and associated bidentate ligands, central spheres represent open pore spaces. Figure 2.5 is a SEM image of the crystals.

Compared with zeolites, which are also crystalline and microporous, zeolites are fully inorganic and thus lack synthetic flexibility, unlike MOFs [39]. An increasing number of MOFs are now being explored for their interesting properties, including optic, magnetic, and electronic properties, as well as their various potential applications such as catalysis, ion exchange, sensing, polymerization, and drug delivery [23].

Besides the pre-design in synthesis, post-synthetic modifications have also been successfully used to modify chemically MOFs after the crystalline materials have already been formed [23]. A general scheme illustrating the concept of post-synthetic modification of porous MOFs is shown in Figure 2.6. This remarkable and easy re-design ability is quite different from that of traditional porous materials, such as zeolites and activated carbon. It allows facile optimization of the pore structure, surface functions, and other properties for specific applications as porous material [23].

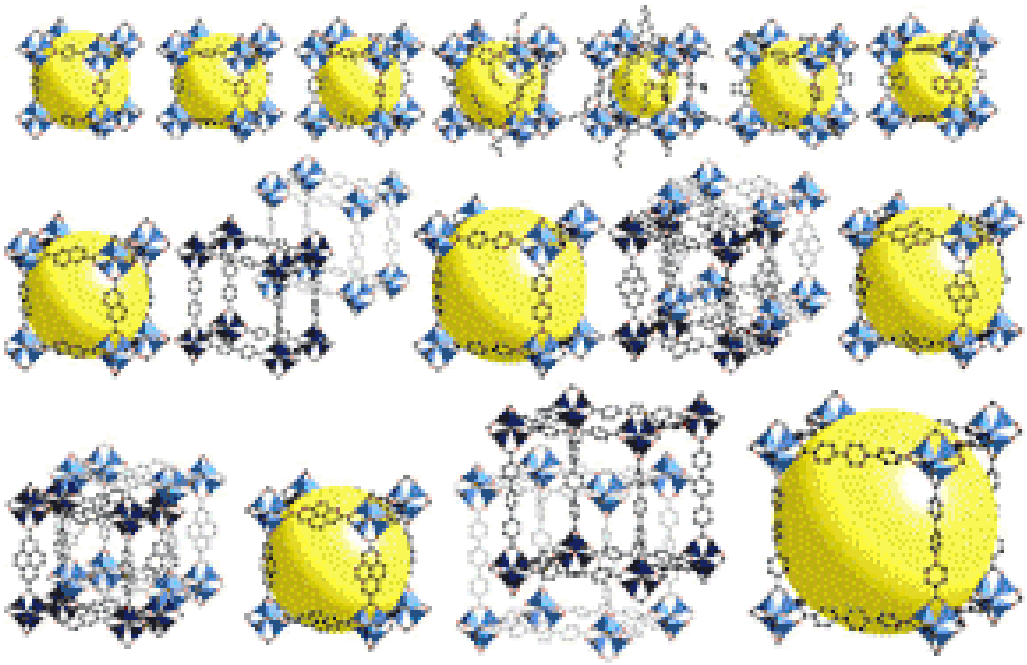

Figure 2.4 Structure of MOF-5 derivatives called IRMOFs and associated bidentate ligands, central spheres represte open pore spaces.

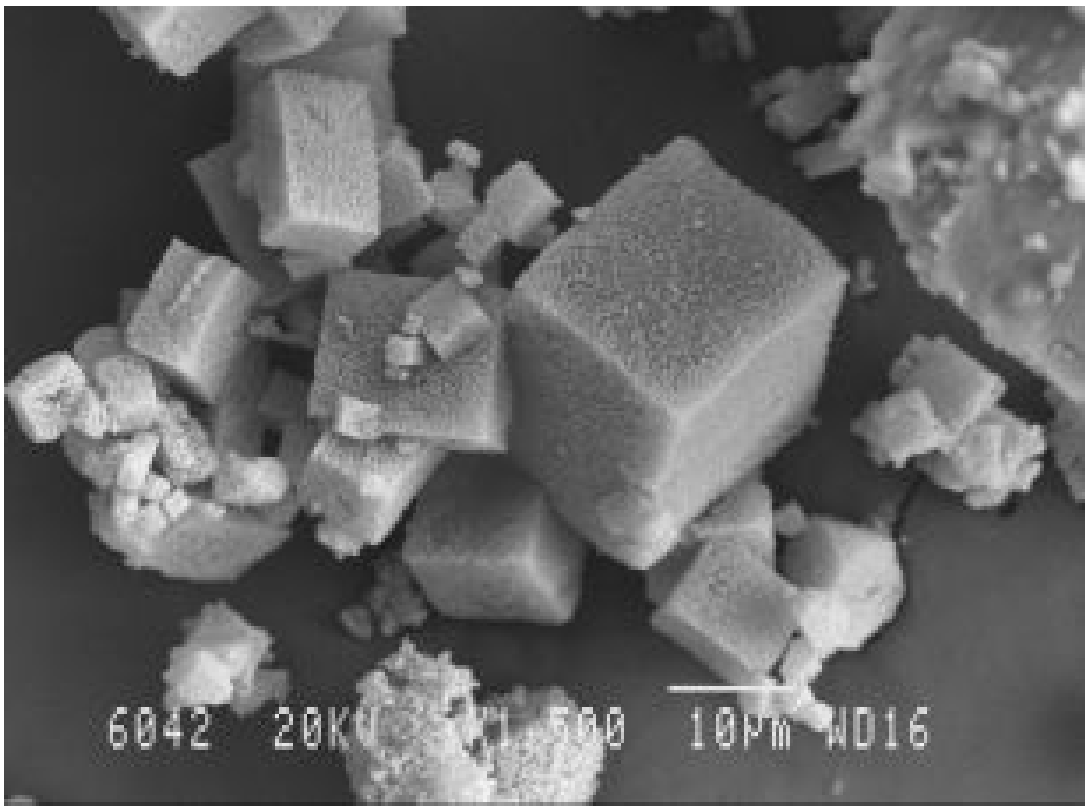

Figure 2.5 Morphology of crystals from MOF-5 samples determined by SEM analysis [23].

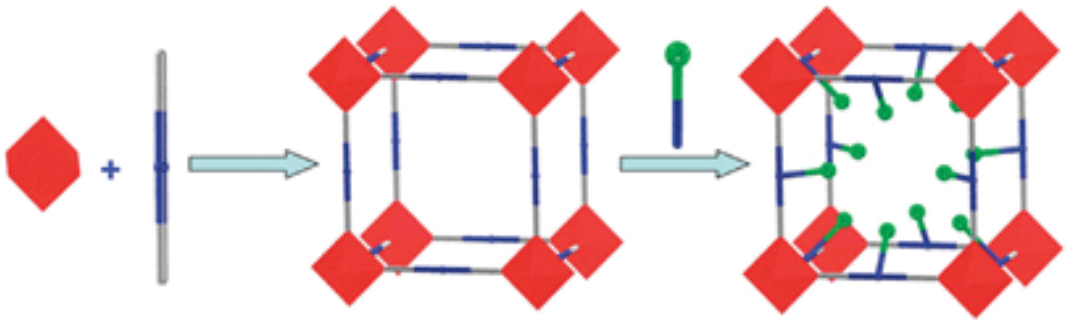

Figure 2.6 A general scheme illustrating the concept of postsynthetic modification of porous MOFs [23].

As a result, the properties of MOFs make them good candidates in separation processes, catalysis and gas adsorption applications. Most of the recent studies have been concentrated on hydrogen and methane storage because of their high surface areas, which increase van der Waals interactions needed for uptake of weakly interacting gases, and exploit the tunability of MOF pore dimensions to control relative rates of adsorption and transport through the pores [40-42].

MOFs are also attracting increasing attention in CO_2 capture due to these properties. This DOE funded project is focusing on developing MOFs for CO_2 capture. Some MOF materials show extremely high CO_2 capacity and very desirable isotherm shapes, which is an essential feature for CO_2 capture. Millward [43] reported that MOF-177 has the highest CO_2 capacity of any porous material reported (Figure 2.7), at 35 bar, a container filled with MOF-177 could capture nine times the amount of CO_2 in the container compared to that without the adsorbent. The isotherm for MOF-177 displayed behaviour that involved an induction step in their adsorption isotherms, where a small increase at low pressures, and then a sharp increase in the slope of the isotherm occurred at some pressure and the isotherm resumed Langmuir-like behaviour. Llewellyn [44] found that the uptake of CO_2 in MIL-101 (MIL means material from Institut Lavoisier) has been shown to occur with a record capacity of 40 mmol g^{-1}at 50 bar and 30 °C. Dybtsev showed that the MOFs composed of Mn (II) and formate ions are stable enough to maintain single crystallinity after the complete guest removal at 150 °C under a reduced pressure. It also selectively adsorbs H_2 and CO_2, but not N_2 and other gases with larger kinetic diameters, which appears to be due to the small aperture of the channels [44-46].

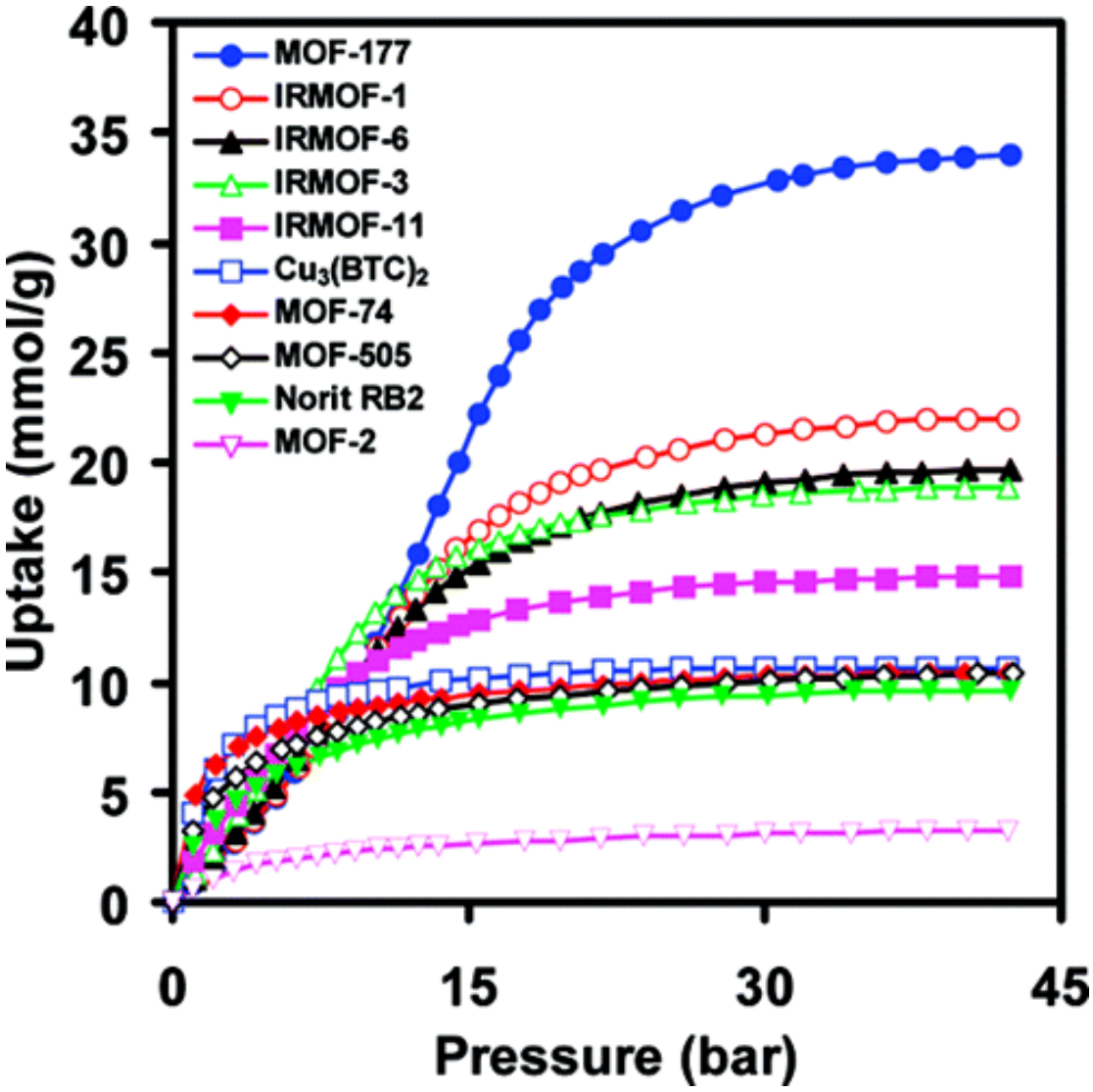

Figure 2.7 Comparison of CO_2 capacities for several MOFs at ambient temperature and pressures up to 42 bar [43].

In order to capture CO_2 from post combustion coal-fired power plants, MOFs should fulfil the following requirements: high CO_2 capture capacity, high selectivity for CO_2 over other gas in the flue gas, good stability. To date, MOFs have shown high CO_2 uptake under equilibrium conditions with pure CO_2, most of them show little capacity in the low pressure regime, however, in the CO_2 post-combustion process, it

is more important to understand CO_2 adsorption in MOF materials at the low pressure regime than at high pressures. There are three ways to increase their CO_2 capture selectivity while maintaining or improving their capture capacity under equilibrium conditions: (a) metal clusters, (b) organic linkers, or (c) novel combinations of both [23].

For the metal cluster, creating open metal sites has been proven to be an efficient approach. These open metal sites formed after the removal of axial ligands of metal atoms by thermal activation or other methods (Figure 2.8). They can offer extra binding sites to the guest gas molecules, especially at low pressures [19, 47]. Britt [48] reported that Mg-MOF-74 (also known as Mg/DOBDC or CPO-27-Mg, Mg_2(DOT); DOT: 2,5-dioxidoterephthalate) with open magnesium sites rivals competitive materials in CO_2 capture, with 8.9 wt. % dynamic capacity, and is able to release CO_2 at a significantly lower temperature, 80 °C. It offers an excellent balance between dynamic capacity and regeneration. Caskey [49] also found the exceptional uptake of the Mg/DOBDC material for CO_2 at ambient temperature and low pressure conditions to be particularly relevant for capture of flue gas from coal-fired power plants. The results demonstrate that physisorptive materials can achieve affinities and capacities that are competitive with amine sorbents. Demessence [50] functionalized the triazolate-bridged MOF-1 (Cu-BTTri) with ethylenediamine, and obtained a very high CO_2 adsorption capacity at low pressures. This material also displayed a record isosteric heat of 90 kJ mol^{-1}. Yazaydin [51] showed that water

molecules coordinated to open-metal sites significantly increase CO_2 adsorption in Cu-BTC by simulation study.

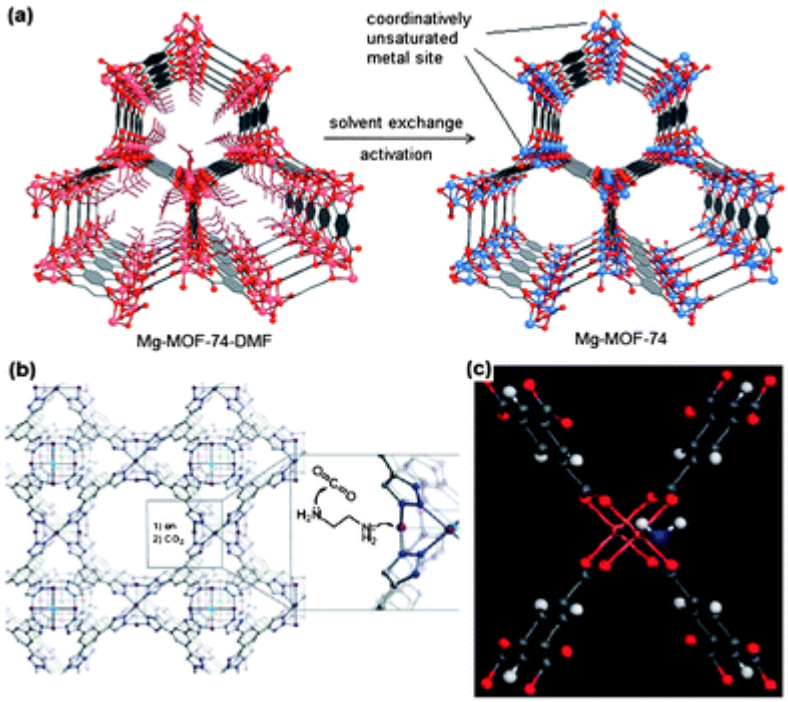

Figure 2.8 (a) Single crystal structure of Mg-MOF-74, formed by reaction of the DOT linker with Mg $(NO_3)_2 \cdot 6H_2O$. C atoms are shown in grey, O atoms in red, 6-coordinate Mg atoms and terminal ligands in pink and 5-coordinated Mg atoms in blue. H atoms and terminal ligands on the fragment in the top right are omitted for clarity. (b) A portion of the structure of the sodalite-type framework of Cu-BTTri (**1**) showing surface functionalization of a coordinatively unsaturated Cu^{2+} site with ethylenediamine, followed by attack of an amino group on CO_2. Purple, green, grey, and blue spheres represent Cu, Cl, C, and N atoms, respectively; framework H atoms are omitted for clarity. (c) Hydrated Cu-BTC (4 wt %) with a coordinated water

molecule from DFT. Cu atoms are orange, O red, C grey, and H white. The oxygen atom of the coordinated water molecule is shown in blue [39].

with the modification of organic linkers, Bae [52] studied the carborane-based metal–organic framework with and without unsaturated metal sites and found high selectivities for CO_2 over CH_4 (~17) especially in the material with open metal sites.

For gas adsorption, the isosteric heat of adsorption is another definitive property that is directly related to the separation and storage ability. The heats of adsorption for CO_2 stretch across a large range, between 20 and 50 kJ/mol [23], an ethylenediamine-functionalized MOF reported by Long also exhibits an isosteric heat of CO_2 adsorption of 90 kJ/mol, this chemisorption interaction is the strongest reported to date for a metal−organic framework and points toward the potential utility of alkylamine-appended frameworks for the postcombustion capture of CO_2 from low-pressure flue gas streams [53]. In most cases, the heat of adsorption decreases with increased loading, and that a high heat of adsorption is not necessarily good in the CO_2 separation application, as the large energy requirement associated with the regeneration (i.e. desorption) of the materials [54].

Much attention has also been paid to the synthesis of novel MOFs with both high CO_2 capture capacity and desired stability. Recently, a new class of MOFs known as zeolitic imidazole frameworks (ZIFs), having high chemical and thermal stabilities

(up to 500 °C) and a unique framework structure composed of large cages connected by small windows, was announced by Yaghi's group [56]. The crystal structures of ZIF are based on the nets of seven distinct aluminosilicate zeolites: tetrahedral Si(Al) and the bridging O are replaced with transition metal ion and imidazolate link, respectively [55]. A typical structure of ZIF is shown in Figure 2.9. Moreover, ZIFs are a very promising type of material for selective adsorption of CO_2, and they are twice as efficient as BPL carbon at 1 bar and 298K (a commercially available carbon product of Calgon) [55]. They may seem promising when compared to BPL carbon but they have less than one fifth of the adsorption capacity of commercial zeolites such as X, Y and 5A and are comparable to silicalite.

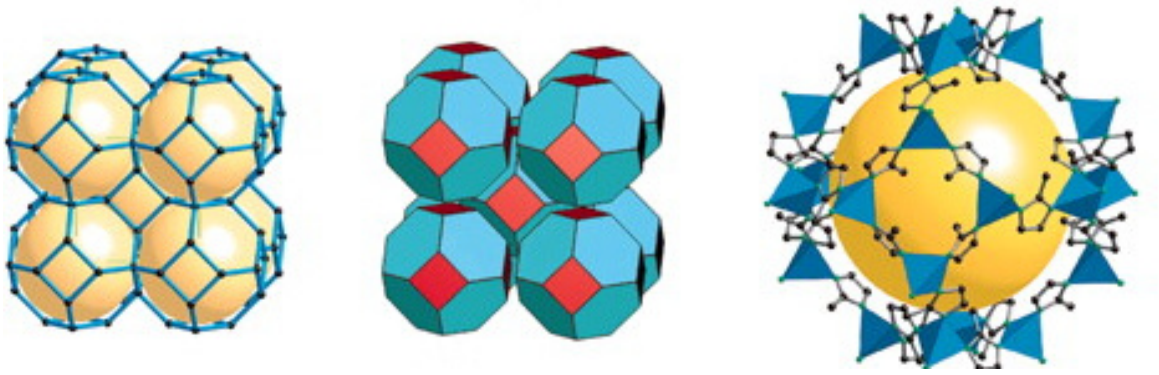

Figure 2.9 The single crystal x-ray structures of ZIFs. (left and center*)*, the net is shown as a stick diagram *(*left*)* and as a tiling (center). (right)The largest cage in each ZIF is shown with ZnN_4 tetrahedra in blue, H atoms are omitted for clarity [56].

Most of MOFs have good thermal stability, but in terms of hydrothermal sensitivity, a large number of MOFs, especially those constructed by Zn_4O cluster nodes, decompose upon contact with humid air [56, 57]. It should be pointed out that the

synthesis of stable MOFs, especially those being water stable, is still one of biggest challenges in the research field of MOFs for their practical applications [23].

The cyclic and thermal stability of MOFs during adsorption and desorption cycle is also very important when connected to application process. Lu reports that in cyclic CO_2 physisorption the capacity of the MOF-5 ($Zn_4O(BDC)_3$) crystals to be 3.61 wt% when cycled between 30 °C and 300 °C through 10 separate capture and release cycles. Above 400 °C MOF-5 underwent thermal decomposition and were no longer capable of capturing CO_2 [58].

2.5 Conclusions

In this chapter, the main classes of adsorbents for carbon capture were introduced. There are an unlimited number of possible MOF structures that can be prepared, and a good candidate for carbon capture should have desirable characteristics, such as a low energy requirement for regeneration, good thermal stability, tolerance to contaminants, attrition resistance, and low cost. Therefore there is a need to develop novel laboratory measurements for rapid screening of adsorbents.

CHAPTER 3

3. THEORY OF THE ZERO LENGTH COLUMN (ZLC) TECHNIQUE

3.1 Introduction of the zero length column (ZLC) technique

With strongly adsorbed species, determination of intracrystalline diffusivity from conventional uptake rate measurements becomes increasingly difficult. Such effects may be minimized by using large crystals and very small adsorbent samples, but for most zeolites, crystals greater than about 100μm are not available and the minimum sample size is limited by the sensitivity of the equipment to a few milligrams. For accurate measurement of the rapid intracrystalline diffusion process with strongly

adsorbed species; with the intrusion of extraneous heat and mass transfer resistance, an alternative experimental technique was invented, known as the Zero Length Column (ZLC) method [59].

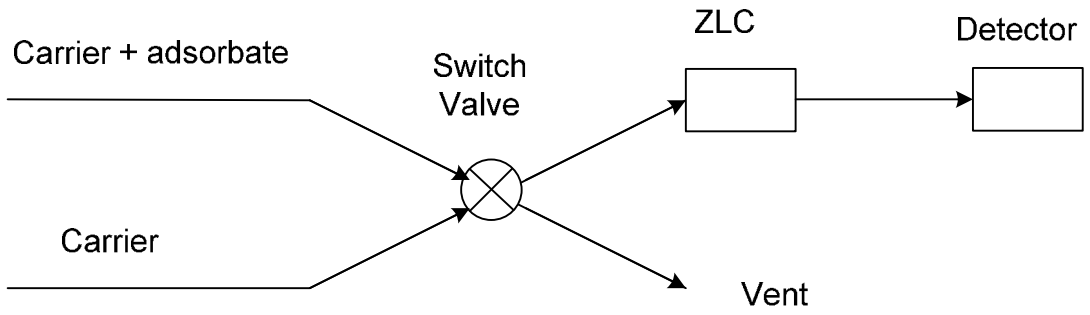

Figure 3.1 simplified schematic of original ZLC system.

The original idea for the ZLC system dates back to the late 1970s, but it was not until the late 1980s that the well known Eic and Ruthven [17, 59] paper appeared. It is a simple and relatively straight forward technique of measuring diffusion coefficients in zeolite particles. The zero length column technique retains the main feature of the conventional chromatographic methods and eliminates the effect of axial dispersion [17, 59]. The ZLC is a differential bed of porous particles, which is first equilibrated with the fluid mixture containing the adsorbed species; at time zero the adsorbing gas is switched to a carrier gas (normally inert gas) flow through the ZLC at sufficiently high flow rate. The desorption curve is analyzed in terms of concentration of adsorbate versus time. Figure 3.1 shows a schematic diagram of a ZLC system, the column consists of only a few layers of adsorbent and it can be considered as a well mixed cell. This method is widely applied to gaseous systems [60].

3.2 Mathematical models of the ZLC

The mathematical model describing the ZLC system is based on the following assumptions (shown in Figure 3.2):

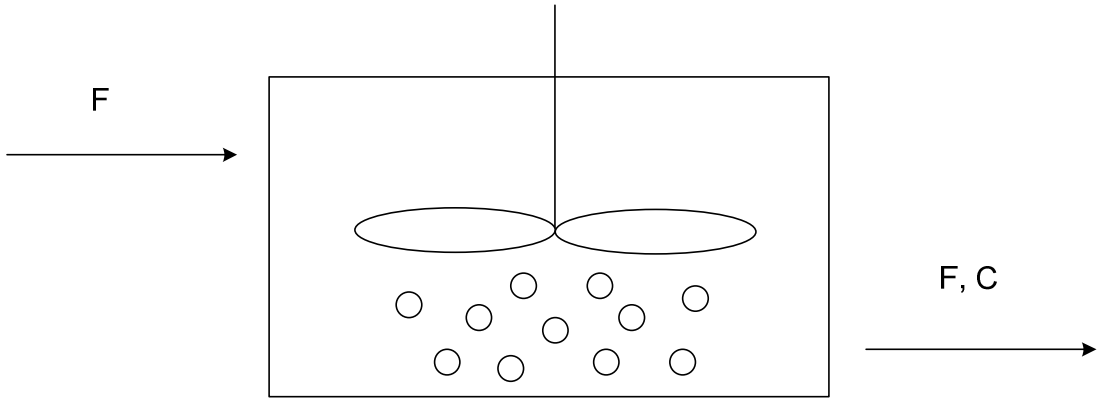

Figure 3.2 Schematic for the ZLC model

(1) The adsorbent material has a porous structure.

The ZLC was specifically developed for microporous adsorbents, in particular zeolites [59].

(2) Fick's law of diffusion is valid;

This assumption can be checked experimentally through the use of the partial loading experiment and by carrying out multiple tests with adsorbents of different sizes [60]. Here it is needed to define the mathematical model to be used in the mass balance in the solid.

(3) The adsorption equilibrium isotherm is linear;

This assumption is one of the most difficult to ensure under real experimental

conditions. Linearity is a requirement in order to obtain an analytical solution, but numerical solutions can be found also with nonlinear isotherms and experimental checks can be carried out. Brandani Jama and Ruthven [61] discuss in great detail the effect of this assumption in the interpretation of ZLC experiments.

(4) There is no film resistance at the adsorbent external surface;

This assumption reflects the fact that for gas systems the bulk diffusivity is relatively high and hence the mass transfer resistance is dominated by the internal mass transfer kinetics [62].

(5) The ZLC cell is considered equivalent to a continuous stirred tank adsorber;

This assumption is justified by the fact that a normal dispersed plug-flow model for a column with Danckwerts' boundary conditions is dominated by axial dispersion when the length of the column becomes very small. In this limit of short columns, the full dispersed plug-flow model becomes equivalent to a CSTR [11]. This assumption can also be checked experimentally by repeat experiments with different sample masses, but it is likely to be a potential problem only for very strongly adsorbed components [18].

(6) Crystals have spherical geometry;

The definition of the geometry is needed to arrive at a formulation that can then be solved. In adsorption and catalysis with finite particles, the spherical model is often assumed and for non-spherical particles an equivalent radius based on the surface to volume ratio is used. ADD ref to Ruthven 1984

(7) Isothermal operation is assumed.

This assumption is generally valid for small particles. Only for pellets with strongly adsorbed molecules one has to ensure that conditions of isothermality are met. Brandani et al. [63] have analysed the case of non isothermal ZLC in detail and all our experiments met the conditions needed for this assumption to be valid.

The differential mass balance is given by

$$V_S \frac{d\bar{q}}{dt} + V_g \frac{dc}{dt} + Fc = 0 \tag{3.1}$$

Where V_g is the volume of gas in the ZLC cell; V_s represents the volume of solid in the ZLC cell; F is the flowrate; $\bar{q}$ is the average adsorbed phase concentration and c is the sorbate concentration in the gas phase. During the experiment the gas phase concentration is measured and the flowrate is assumed that the carrier flowrate remains constant, to obtain the correct V_s value a good balance is needed and for V_g careful blank runs are needed.

The differential solid (crystal) mass balance is given by

$$\frac{\partial q}{\partial t} = D\left(\frac{\partial^2 q}{\partial r^2} + \frac{2}{r}\frac{\partial q}{\partial r}\right) \tag{3.2}$$

and

$$\frac{\partial q}{\partial t}(0,t)=0 \tag{3.3}$$

$$q(R,t)=Kc(t) \tag{3.4}$$

$$q(r,0)=q_0=Kc_0 \tag{3.5}$$

The original model proposed by Eic and Ruthven [17, 59] did not take into account the hold up of sorbate in the fluid phase. Brandani and Ruthven [60] derived a solution to the model that includes fluid phase hold up for more accurate results.

$$\frac{c}{c_0}=2L\sum_{n=1}^{\infty}\frac{\exp(-\beta_n^{\,2}Dt/R^2)}{[\beta_n^{\,2}+\left(L-1-\gamma\beta_n^{\,2}\right)^2+L-1+\gamma\beta_n^{\,2}]} \tag{3.6}$$

Where the β_n are the positive roots of:

$$\beta_n\cot\beta_n+L-1-\gamma\beta_n^{\,2}=0 \tag{3.7}$$

and，

$$\gamma=\frac{V_g}{3KV_s} \tag{3.8}$$

where the parameter γ can be characterized as the ratio of external to internal holdup. When γ < 0.1, the effect of the extra particle hold-up is negligible.

$$L = \frac{1}{3}\frac{F}{KV_s}\frac{R^2}{D} \tag{3.9}$$

This parameter represents the ratio between the diffusional time constant and the "washout" of the solid phase. At high purge flow rates or low sample mass (large values of L) the desorption rate is controlled by the diffusion of the sorbate out of the particle. At low purge flow rate or large sample mass, contact time is large compared with the diffusion time (R^2/D) and the desorption rate is determined by convection under equilibrium conditions.

The analytical solutions presented above are only strictly valid if all the assumptions made hold. For the systems studied in this work, the only assumption that has to be considered carefully is that of the isotherm linearity. This will not have a significant effect on diffusivity measurements [63] but obviously is very important if equilibrium data is extracted from the ZLC curves. If this is the case, then one has to start from the original cell mass balance as discussed in detail in sections 3.3.2 and 3.3.3.

3.3 Equilibrium control

When the parameter L is small the system becomes controlled by adsorption equilibrium and the response curve does not contain kinetic information. The use of the ZLC technique to rank materials is based on equilibrium capacity measurements.

The experiments have to be carried out at low flow rates and high sample mass to achieve equilibrium control.

3.3.1 Linear equilibrium

If the system is under equilibrium control and the adsorption isotherm is linear, one can assume:

$$\bar{q} = q^* = Kc \tag{3.10}$$

In this case the Eq. (3.1) becomes

$$\left(V_f + KV_s\right)\frac{dc}{dt} = -(Fc)_{out} \tag{3.11}$$

The desorption curve reduces to a simple exponential decay [64], curves should overlap when plotted as c vs. Ft (shown in Figure 3.3 and 3.4).

$$\ln\frac{c}{c_0} = \frac{-Ft}{KV_S + V_g} \tag{3.12}$$

This expression can be derived directly from eq. (3.1) and this equation is a good approximation for L < 0.5.

A plot of ln (c/c_0) vs. time (or the product Ft) should yield a straight line through the origin with slope $\frac{-F}{KV_S + V_g}$ (or $\frac{-1}{KV_S + V_g}$). For strongly adsorbed species (K large, $KV_S >> V_g$) the slope yields directly the value of the dimensionless Henry constant

(K). For weakly adsorbed species KV_S is of the same order of magnitude of V_g but the dead volume of the cell can be easily obtained by blank runs, i.e. performing an experiment with no adsorbent in the ZLC. In this case, a plot of $\ln(c/c_0)$ vs. Ft yields directly the value of V_g. From Eq. (3.12) it is easy to see that in a plot of $\ln(c/c_0)$ vs. Ft the ZLC response curve under equilibrium control is invariant with the flowrate, hence varying the purge flow rate is a simple and direct experiment method to check if the system is under kinetic or equilibrium control.

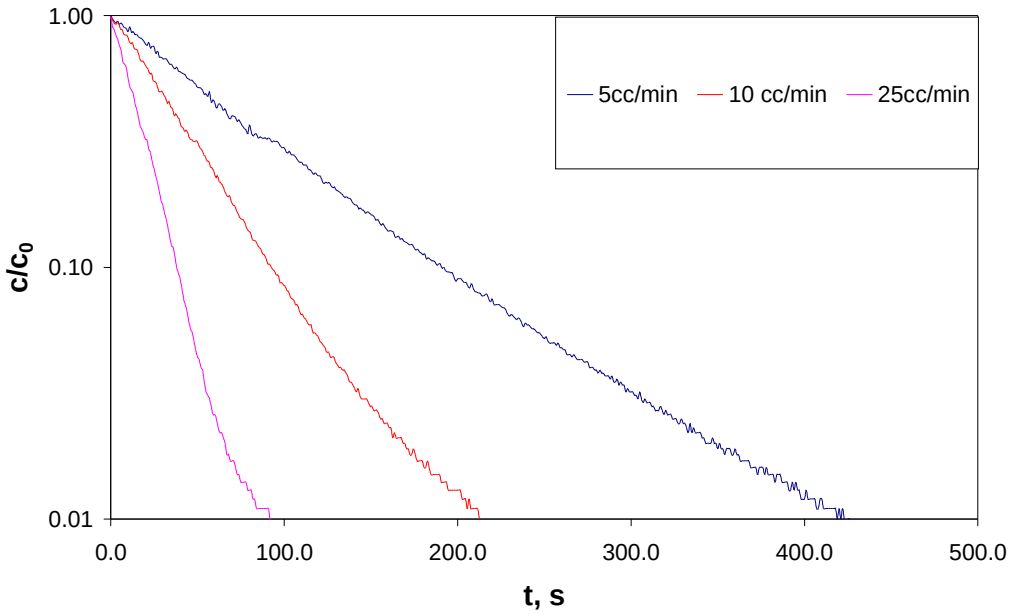

Figure 3.3 Typical experimental ZLC response curves at different flowrates under equilibrium control. (Ni/DOBDC powder at 0.1bar of CO_2 in Helium, 38 °C, 5, 10 and 25 cc/min)

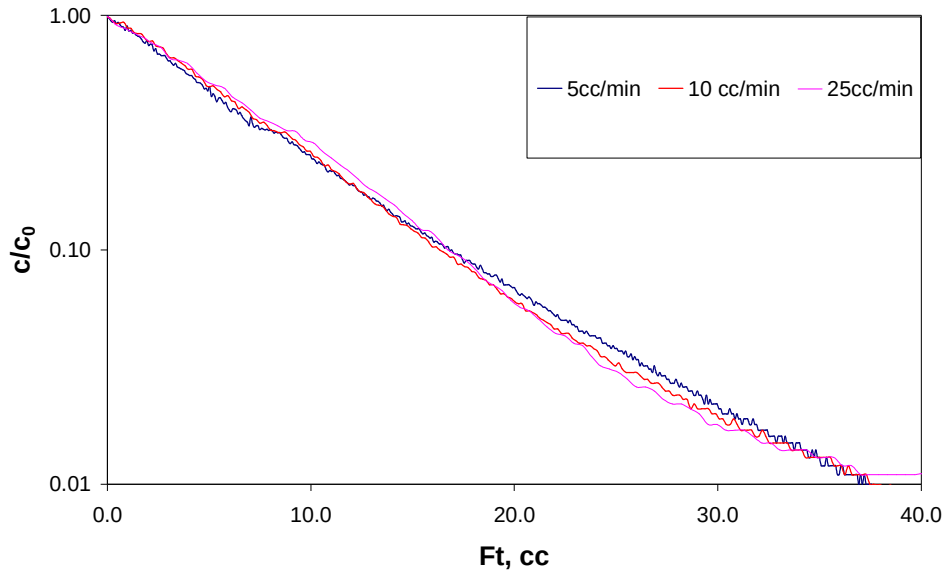

Figure 3.4 Typical ZLC Ft plot at different flowrates under equilibrium control (Ni/DOBDC powder at 0.1bar of CO_2 in Helium, 38 °C, 5, 10 and 25 cc/min)

3.3.2 Langmuir equilibrium

Beyond the Henry's Law region the isotherm may be approximated by the Langmuir expression:

$$\frac{q^*}{q_s} = \frac{bc}{1+bc} \tag{3.13}$$

Under these conditions the desorption curve solution is

$$\ln\frac{c}{c_0} = \frac{-Ft}{KV_S + V_g} - \frac{KV_s}{KV_S + V_g}\left[\frac{1}{1+bc} - \frac{1}{1+bc_0} + \ln\left(\frac{1+bc_0}{1+bc}\right)\right] \tag{3.14}$$

In the long time region, the plot ln (c/co) vs. Ft approaches a linear asymptote of slope $\frac{-1}{KV_S + V_F}$, which represents the linear response, with negative intercept given

by $\frac{KV_s}{KV_S + V_g}\left[1 - \frac{1}{1+bc_0} + \ln(1+bc_0)\right]$. The Henry law constant can therefore be found from the slope of the long time asymptote. However, for highly non-linear systems (bc_0>>l) this may not be practical as the long time asymptote will be buried in the baseline.

3.3.3 Flowrate correction

The common assumption in the analysis of ZLC experiments is that the carrier flowrate remains constant. Since the inlet flow of the ZLC desorption experiment is a pure inert purge flow, this means that the outlet flowrate is approximated by:

$$(Fy)_{out} = \frac{F_{in}}{1-y} y_{out} \tag{3.15}$$

Where y is the mole fraction of the adsorbing species and this is better than the constant flowrate assumption， y can obtain from $\frac{c}{c_0} = \frac{y}{y_0}$.

The mass balance can be rewritten as

$$V_S \frac{d\overline{q}}{dt} + V_g C \frac{dy}{dt} + F_{in} C \frac{y}{1-y} = 0 \tag{3.16}$$

Therefore it is possible to obtain the complete isotherm by integration of eq.(3.16):

$$q^* = \int_0^\infty \frac{FCy}{V_s} dt - \int_0^t \frac{FCy}{V_s} dt - \frac{V_g C}{V_s} y \tag{3.17}$$

The first term is the adsorbed-phase concentration in equilibrium with c_0 and the second one is $q^*(t)$. Due to the desorption of the adsorbate the total effluent flowrate F is not constant, so it's possible to rearrange eq. (3.17) referring to the flowrate (F_c) of the purge gas which is approximately constant:

$$q^* = \frac{F_C}{V_s} \int_0^\infty \frac{Cy}{1-y} dt - \frac{F_C}{V_s} \int_0^t \frac{Cy}{1-y} dt - \frac{V_g C}{V_s} y \tag{3.18}$$

Eq. (3.18) can be also normalized plotting the concentration vs. Ft/V_s or Ft/M; in this way it is possible to compare directly different samples: the area under the curve is proportional to the amount of sorbate adsorbed.

$$q^* = \int_0^\infty \frac{Cy}{1-y} d\left(\frac{F_C t}{V_s}\right) - \int_0^t \frac{Cy}{1-y} d\left(\frac{F_C t}{V_s}\right) - \frac{V_g C}{V_s} y \tag{3.19}$$

3.3.4 Analysis as breakthrough curves

The ZLC can also be seen as a breakthrough experiment, especially for strong adsorbed components. Based on the mass balance, the total accumulation in the column can be written as

$$\left[\varepsilon\frac{d\bar{c}}{dt}+(1-\varepsilon)\frac{d\bar{q}}{dt}\right]V=(Fc)_{IN}-(Fc)_{OUT} \tag{3.20}$$

With the assumption that gas and solid phase are at equilibrium; ideal gas behaviour; and an isothermal system, the eq. (3.20) can be rewritten in terms of the carrier gas flowrate and the adsorbate mole fraction as

$$[\varepsilon+(1-\varepsilon)K]V\frac{d\bar{y}}{dt}=\left(F_{Carr}\frac{y}{1-y}\right)_{IN}-\left(F_{Carr}\frac{y}{1-y}\right)_{OUT} \tag{3.21}$$

Where $K=\frac{(q_1-q_0)}{(c_1-c_0)}$ represents the slope of the secant of the adsorption isotherm between the two end points.

Assuming a constant carrier flowrate, eq. (3.21) is integrated to obtain

$$-[\varepsilon+(1-\varepsilon)K]=\frac{F_{Carr}}{(y_1-y_0)V}\int_0^{\infty}\left(\frac{y_1}{1-y_1}-\frac{y}{1-y}\right)dt$$

(3.22)

Eq. (3.22) is only suitable for small step changes and the carrier flowrate can be assumed to be constant. Because in Eq. (3.15), $\frac{F_{in}}{1-y}$ cannot be valid for very large

concentration changes (i.e. when if $y = 1$ then $\frac{F_{in}}{1-y} = \infty$), to consider the mass balance for the carrier gas

$$-[\varepsilon + (1-\varepsilon)K_{Carr}]V\frac{d\bar{y}}{dt} = (F_{Carr})_{IN} - (F_{Carr})_{OUT} = \Delta F_{Carr} \tag{3.23}$$

The integral of the difference in carrier flowrate over the entire experiment is:

$$\int_0^\infty \Delta F_{Carr}\, dt = \Delta V_{Carr} = -[\varepsilon + (1-\varepsilon)K_{Carr}]V(y_1 - y_0) \tag{3.24}$$

This result shows that only for small step changes the carrier flowrate can be assumed to be constant and eq. (3.24) should yield a close approximation to the true carrier flowrate.

$$\Delta F_{Carr} \approx \Delta V_{Carr}\frac{y - y_1}{\int_0^\infty (y - y_1)dt} \tag{3.25}$$

The equilibrium isotherm can be obtained from breakthrough curves by using the following equations:

Desorption:

$$\varepsilon + (1-\varepsilon)K = \frac{F_{Carr}}{(y_1 - y_0)V}\int_0^\infty \left[\frac{y_1}{1-y_1} - \left(\frac{y_1}{1-y_1}\right)\frac{y}{1-y}\right]dt \tag{3.26}$$

Adsorption

$$\varepsilon + (1-\varepsilon)K = \frac{F_{Carr}}{y_1 V}\int_0^\infty \left[\frac{y_1}{1-y_1} - \left(1+\frac{\Delta F_{Carr}}{F_{Carr}}\right)\frac{y}{1-y}\right]dt \tag{3.27}$$

Based on the analysis and the set of simulations reported by Wang et al. [23], it is possible to identify the range of conditions where flowrate approximations based on the measured concentrations are valid. Under typical dilute ZLC experimental conditions, the two approximate flowrates are valid even for weakly adsorbed components. For systems where the Henry law constant, K, is greater than 100 the flowrate corrections are reliable even when considering step changes of 50% in concentration [23].

3.4 Kinetic control

3.4.1 Micropore diffusion control

At low purge flow rate, contact time is large compared with the diffusion time (R^2/D) and the desorption rate is determined by convection under equilibrium conditions, however, at high purge flow rates (large values of L) the desorption rate is controlled by the diffusion of the sorbate out of the particle [60]. To measure the diffusional

time constant the experiments are therefore carried out at high flow rates and low sample mass under conditions of kinetic control. For gaseous systems we can neglect the hold up and eq. (3.6) reverts to eq. (3.28).

$$\frac{c}{c_0} = 2L\sum_{n=1}^{\infty}\frac{\exp(-\beta_n{}^2 D_0 t / R^2)}{[\beta_n{}^2 + L(L-1)]} \tag{3.28}$$

$$\beta_n \cot \beta_n + L - 1 = 0 \tag{3.29}$$

In the long time region, the ZLC curves show an exponential decay, equation (3.28) can be rewritten as

$$\frac{c}{c_0} = \frac{2L}{\beta_1 - L(L-1)}\exp\left(\frac{-\beta_1{}^2 Dt}{R^2}\right) \tag{3.30}$$

In a Ft plot, the curves should split and the ZLC plot should therefore yield a linear asymptote in the long time region, D/R^2 and L can be obtained directly from the slope and intercept of the semi-logarithmic plot of c/c_0 vs. t. (a typical plot shown in Figure 3.5 and 3.6) This method is known as the long time (LT) analysis, which is the basic model generally used to extract the diffusional time constant from the ZLC curve.

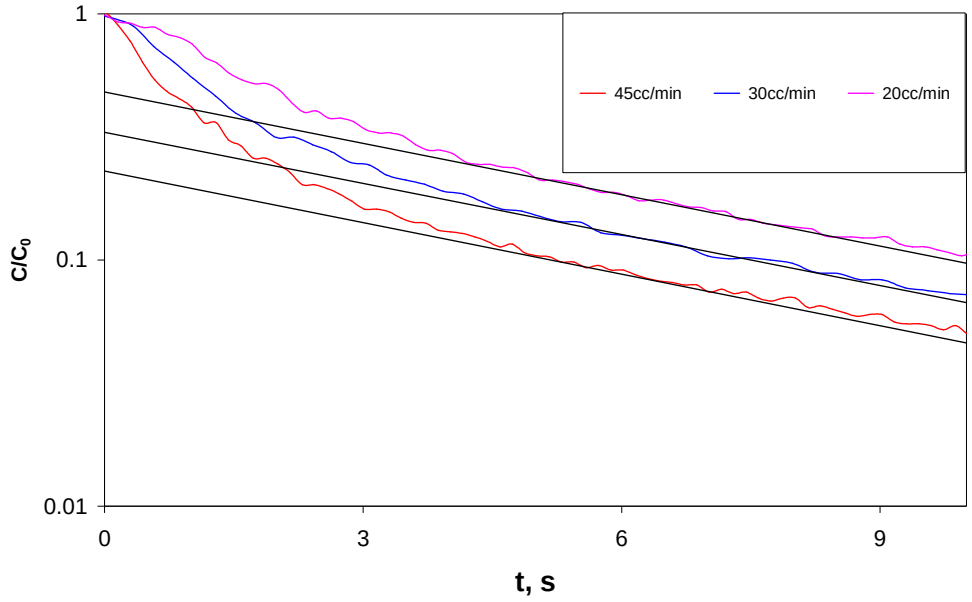

Figure 3.5 Typical experimental ZLC response curves at different flowrates under kinetics control. (Ni/DOBDC pellet (R = 0.79 mm) at 0.1bar of CO_2 in Helium, 38 °C, 20, 30, 45 cc/min)

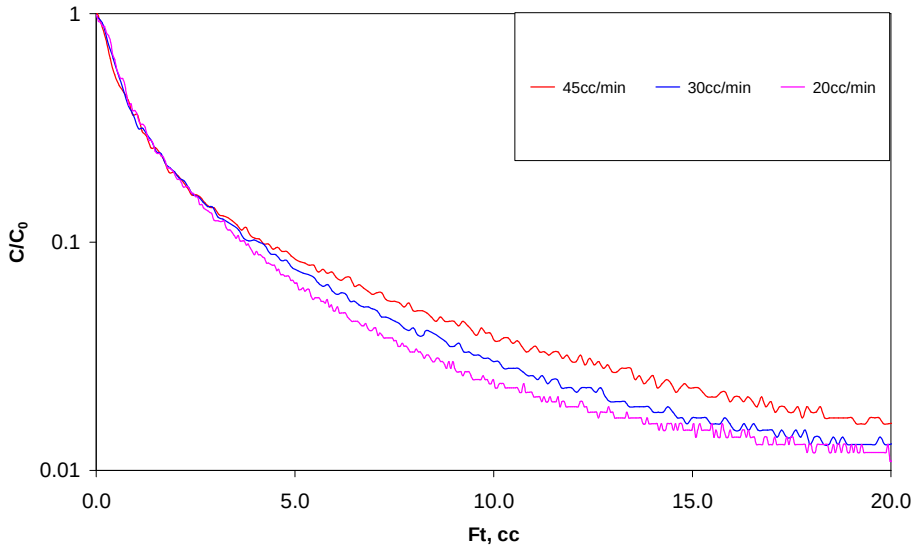

Figure 3.6 Typical ZLC Ft plot at different flowrates under kinetics control. (Ni/DOBDC pellet (R = 0.79 mm) at 0.1bar of CO_2 in Helium, 38 °C, 20, 30, 45 cc/min)

3.4.2 Macropore diffusion control

The ZLC technique can also be applied to the study of intraparticle diffusion. Ruthven and Xu [65] have used the ZLC to study the diffusion of N_2 and O_2 in 5A zeolite pellets. The mass balance in a pellet is:

$$(1-\varepsilon_P)\frac{\partial \bar{q}}{\partial t}+\varepsilon_P \frac{\partial c_P}{\partial t} = \frac{\varepsilon_P}{\tau} D_m \frac{\partial^2 c_P}{\partial z^2} \tag{3.31}$$

where D_m is the molecular diffusivity of CO_2 in the carrier gas and can be estimated from standard correlations based on the kinetic theory of gases [66]； ε_P is the void fraction of the pellet; τ is the tortuosity of the macropores, and assuming that the adsorbed phase in the micropores is at equilibrium with the gas in the macropores, i.e. q = Kc, then

$$[(1-\varepsilon_P)K+\varepsilon_P]\frac{\partial c_P}{\partial t} = \frac{\varepsilon_P}{\tau} D_m \frac{\partial^2 c_P}{\partial z^2} \tag{3.32}$$

which can be rearranged to obtain Fick's diffusion equation and the effective macropore diffusivity

$$\frac{\partial c_P}{\partial t} = D_P \frac{\partial^2 c_P}{\partial z^2} \tag{3.33}$$

$$D_P = \frac{\varepsilon_P D_m / \tau}{\varepsilon_P + (1 - \varepsilon_P) K} \tag{3.34}$$

and there was an explicit recognition of the observation that the tortuosity generally increased as porosity decreases [7], and

$$\tau \approx \frac{1}{\varepsilon_P} \tag{3.35}$$

The denominator in the macropore diffusivity, which represents the Henry law constant K, can be estimated from the Ft plots (Eq. 3.12).

CHAPTER 4

4. ZLC SYSTEM

4.1 Introduction

Given the large number of possible MOF topologies, linkers, and metal nodes, there are an almost unlimited number of MOFs that could be synthesized [42]. As a result, there is a requirement to develop a technique to characteristic materials rapidly and interpret the results easily. Adsorption equilibrium measurements have traditionally been carried out by gravimetric, volumetric, or piezometric methods, these techniques are straightforward and accurate, but they are time-consuming and are therefore not well-suited to adsorbent screening studies. The purpose of the present

research was to develop the semi-automated ZLC system based on its potential and to study novel adsorbents of carbon capture.

4.2 Traditional ZLC system

Figure 4.1 shown below is the traditional ZLC system, which consists of a gas chromatograph (GC) oven, and an on-line quadrupole mass spectrometer. The flow rates of both feed and purge streams are controlled by mass flow controllers, the bubbler in the system is used to feed vapours. Figure 4.2 shows the detail inside the GC oven, highlighting the ZLC cell. The switch valve is placed in a separate oven; the sorbate mixture in a traditional system is for using on-line gas mixing system. There are some drawbacks in the traditional ZLC setup. The GC oven is limited to 300°C, which is sometimes not sufficient to regenerate fully adsorbents; the bubbler used to feed vapour may cause leaks; the flowrate is greater than 10 cc/min, high flowrates may not allow reaching the equilibrium control. Based on these limitations of the traditional system, the new ZLC system was developed.

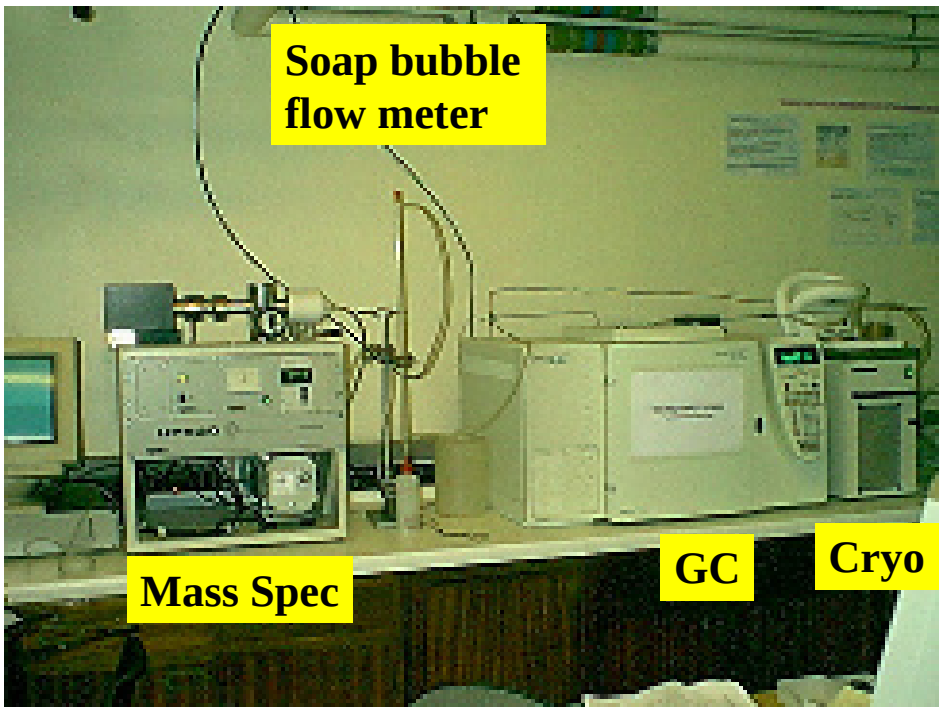

Figure 4.1 overview of traditional ZLC system

4.3 Semi-automated ZLC system set up

The experimental set-up was subject to several modifications during the project resulting from changes in the experimental requirements or by feedback derived from analysis of the preliminary experimental results. Figure 4.4 shows a simplified schematic diagram of the semi-automated ZLC/ breakthrough apparatus used in the experiments to measure CO_2 capacity of adsorbents. This new ZLC experimental set up was constructed in house at the University of Edinburgh and has some improvements over the traditional ZLC system.

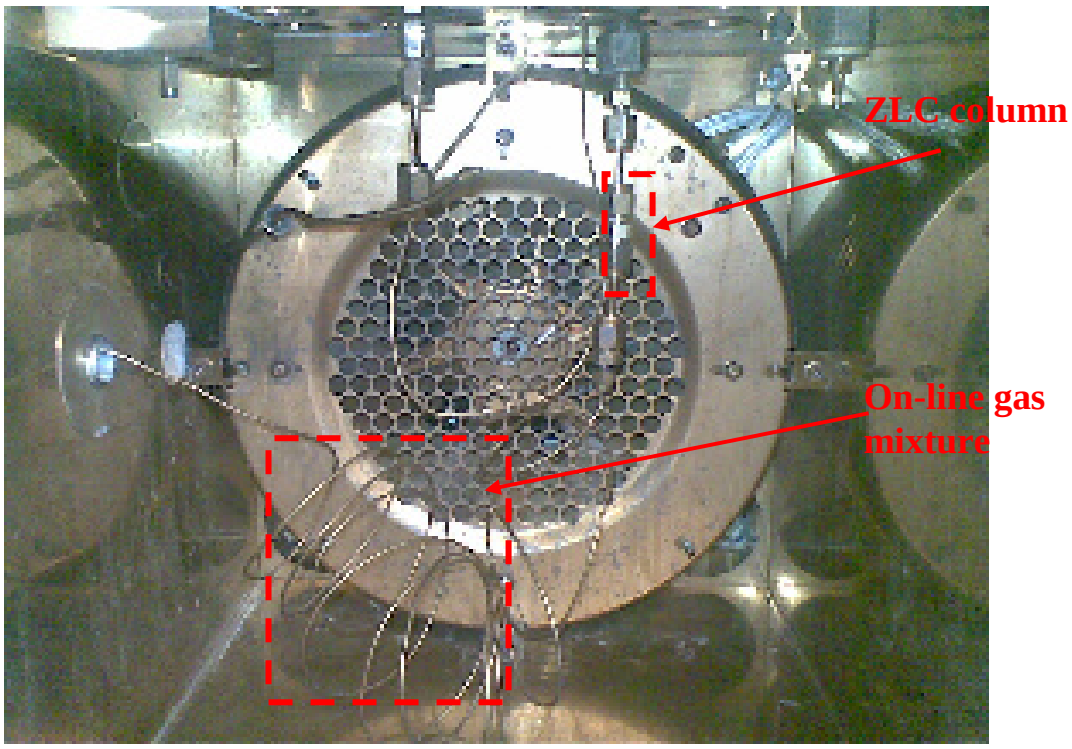

Figure 4.2 inside view of GC oven includes ZLC column

Table 4.1 shows the specification of the new ZLC system and Figure 4.4 shows the overall view of the ZLC apparatus. The apparatus includes gas dryers; a new gas dosing system; a flow control system; a preheat oven; a set of four on-off valves to switch the gas flows, the ZLC oven and detectors.

Table 4.1 the specification of ZLC measurements.

Specification of Zero Length Column system		
Temperature Range	30-400ºC	
Pressure Range	Atmospheric (carbon dioxide partial pressure in helium up to 1 bar)	
Adsorbents Sample Size	1-3 mg	Kinetic experiments
	10-15 mg	Equilibrium experiments
	up to gram quantities	Breakthrough experiment

Figure 4.3 Image of the zero length column (ZLC) system setup

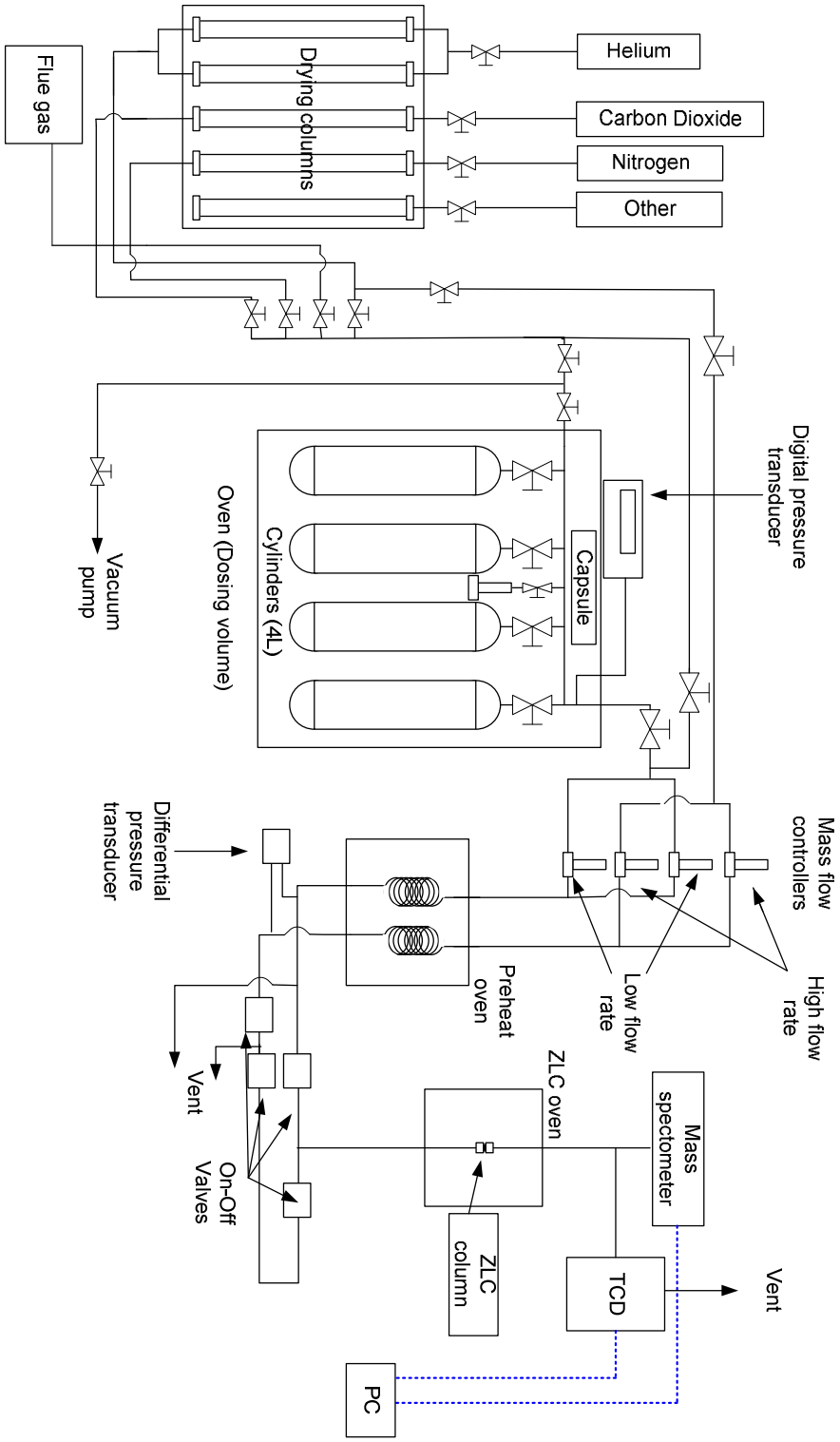

Figure 4.4 Simplified schematic diagram of Zero Length Column (ZLC) system setup

4.4 Dosing system development

Figure 4.5 (a) shows the front view of the dosing system, the four stainless steel cylinders (1L each) and the capsule in the drying oven (Sanyo MOV-212) are the dosing volume where the gas mixtures or gas mixture containing water or other vapours are prepared. As it is important to pay careful attention for hydrophilic adsorbents, individual drying columns, packed with silica gel and zeolite in each of the pure gas lines are utilized to remove just before the inlet to the dosing oven any residual water coming from the cylinder of the gas supplier. To prepare a gas mixture, the dosing volume was first filled with helium and flushed three times using a vacuum pump (Edwards 5 oil free pump) connected to the dosing volume. A pressure indicator was applied to measure the amount of gas introduced into the volume. The procedure followed was to introduce first partially the inert gas, then to add the desired amount of sorbate, finally topping up the volume with helium to the desired pressure.

The capsule (Figure 4.5 (d)) connected to the dosing volume is used for dosing water vapour (or other solvents) into the system by using an elevated temperature inside the oven. This process involves double checking the pressure change in the dosing system and weighing the capsule before and after adding water to the system, using a Mettler-Toledo balance (XS205). A mixture containing an accurate partial pressure of vapour can be prepared.

Compared to the gravimetric experiments, the ZLC offers some advantage in terms of the time required for the measurements, but where it becomes very useful is in the determination of the effect of water. The developed ZLC system with dosing system is able to carry out experiments without any water and then expose the sample to water and CO_2 and or other impurities and then measure the resulting CO_2 capacity.

The pressure gauge installed on the top of the dosing oven connected with stainless steel lines led to the formation of a cold spot where water vapour would condense, even when the lines outside the oven had been heated up, because the design temperature of the gauge was limited to 55-60 °C. With this cold spot water would condense when the concentration was above 1% v/v. Therefore, a digital pressure transducer was installed and connected directly above the oven to eliminate the cold spot. Furthermore, the digital pressure transducer has an accuracy of ±0.01 bar, which is much better than the reading from the pressure gauge.

The oil pump was also replaced by an oil-free vacuum pump to avoid contamination during the mixture preparation. Compared to the traditional ZLC, the new system contains a closed dosing volume connected to the pressure transducer and a capsule. The gas mixture is of known concentration (i.e. 0.1-10% CO_2 in Helium). The gas with vapour can be prepared accurately. This modification avoids leakage which can happen in the glass bubbles placed in a bath chiller used normally to prepare the gas mixture with water vapour.

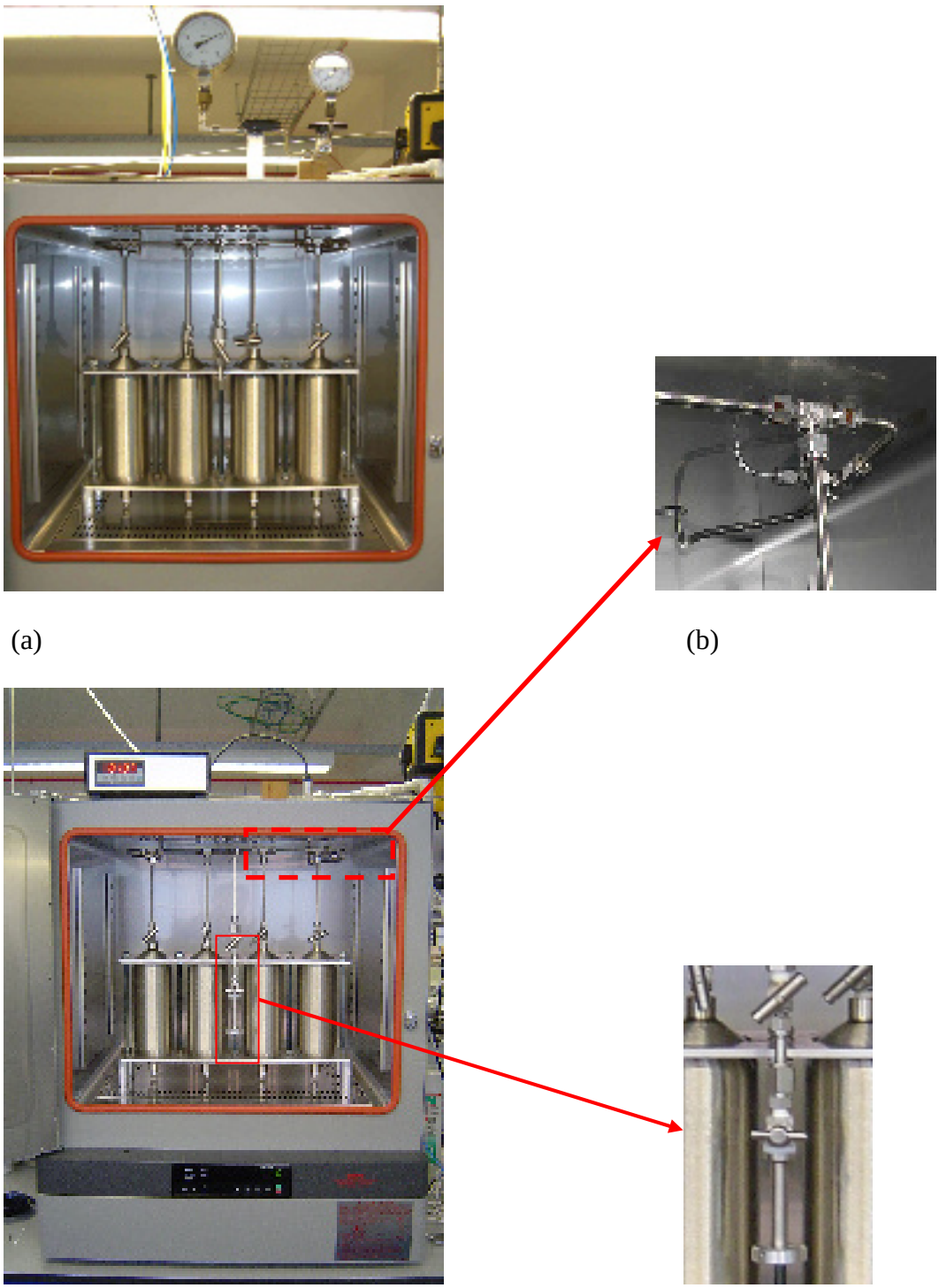

(a) (b)

(c) (d)

Figure 4.5 old front view of the dosing system (a), improved view of dosing system (b), specific view of pressure transducer connection (c), specific view of capsule with needle valve (d).

4.5 Procedure of preparing the mixture

Figure 4.6 shows the schematic diagram of the dosing volume. To prepare a normal gas mixture the procedure is summarised.

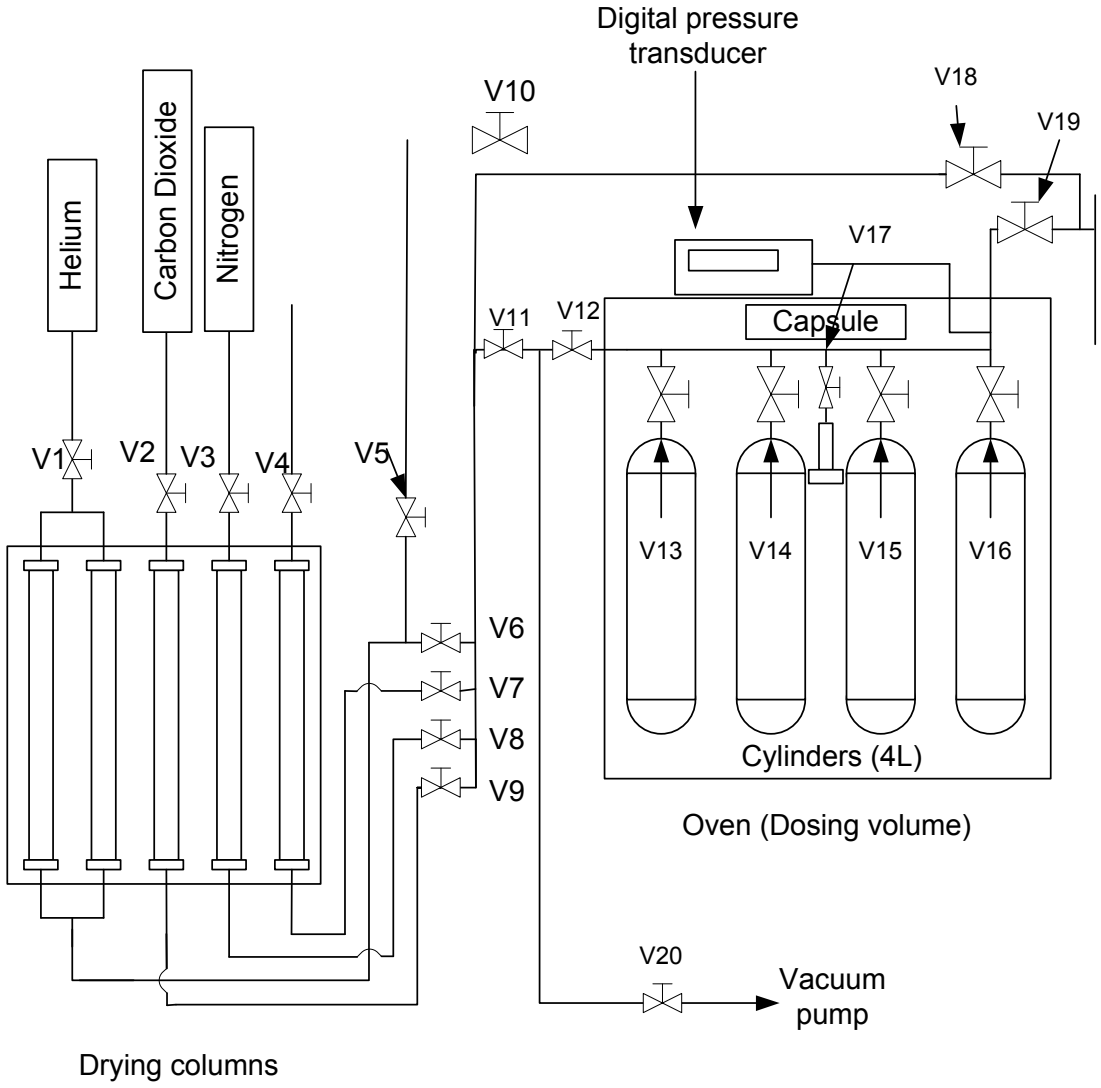

Figure 4.6 Simplified schematic diagram of dosing volume

• Dosing volume purge

First of all, V1, V2, V12, V13, V14, V15, V16, V17 and V20 are opened with the vacuum pump switched on, the rest of valves are closed, and this is used to evacuate the dosing volume. Then, V20 is closed and V11 is opened, followed by V6 opening slightly to refill helium (0.5 bars) in-to the dosing volume. Then V6 and V11 are closed, V20 is opened slowly (avoid damaging vacuum pump) to evacuate the dosing system again. This filling and emptying procedure is applied a further two times to make sure there is no residual gas in the dosing volume. If the system was working with vapour mixture before, an elevated temperature (100ºC) in the oven is needed in this procedure.

• Gas mixture (i.e. 10% CO_2 in He total 4 bars)

To prepare a typical mixture with 10% CO_2 in helium, V20 is closed and V6, V12 are opened to fill helium into the system (1 bar). Then V6, V12 are closed V20 is opened to vacuum. After that, V20 is closed, V9 and V12 are opened to feed CO_2 into the dosing volume (0.4 bars). Then V9 and V12 are closed, V20 is opened to vacuum again, and this is followed by closing V20 and then opening V6, V12 to top up the helium gas (2.6 bars) in the volume. Finally, V12 and V11 are closed, to obtain 10% CO_2 in a gas mixture (total 4 bars) with helium.

• **Gas mixture with vapour (i.e. 10%CO_2, 1% H_2O in He total 4 bars)**

The weight of the capsule filled with distilled water is first measured on the balance. The capsule is connected to the dosing volume, V17 is opened and the volume is evacuated as described above. The temperature of the oven is elevated to an appropriate temperature (below boiling point at 0.5 bar), then, V20 is closed and V6, V12 are opened to fill helium into the system (0.5 bar). and 1 hour are allowed to reach thermal equilibration. After this, the capsule valve is opened slowly to allow the water vapour to evaporate into the dosing volume. The capsule valve is closed once the pressure reaches 0.54bar, which means that the water vapour amount is enough, disconnect the capsule and remove from the dosing oven. Wait until the capsule is fully cooled down to room temperature, re-weigh it and the different weight of the capsule (water loss) is a good way to double check and confirm the correct water amount is in the system. Then dose helium and CO_2 as described previously to obtain the final mixture.

4.6 Gas flow and ZLC oven development

Figure 4.7 shows the front view of the ZLC apparatus. In the flow control part (top left), two sets of mass flow controllers were installed on the system. Both high flowrates (0-50 cc/min) and low flowrates (0-3 cc/min) can be applied to the measurement, depending on kinetic or equilibrium control. Since the traditional ZLC is using a high flowrate mass flow controller, it is therefore possible in the new system to reach conditions of equilibrium easily by using smaller flowrates (low L

value). The use of small flowrates reduce the gas consumption in the experiment and this is an important feature when special gas mixtures are used, i.e. synthetic flue gas is quite expensive from a gas supplier, i.e. a typical 5L cylinder with 200 bars synthetic flue gas costs more than £400. In a normal breakthrough experiment, one cylinder can only last for one week and one sample test, but the ZLC system only consumes a few bars in a week-long measurement.

A differential pressure readout (below the mass flow controllers) was installed to measure the pressure difference in gas lines (not an issue for the low flowrate). All lines in the system are heated to avoid water condensation when vapour mixture experiments are carried out and the heating temperature is adjusted by an electronic controller (small blue box at the bottom).

There is a preheat oven (left white box) placed before the ZLC oven (right white box) in order to preheat the gas sufficiently to ensure isothermal condition of gas flow into the ZLC oven at a set temperature. The two ovens are controlled by two independent control units (bottom centre).

Two needle valves are connected after the ZLC and on the vent line to balance the pressure in order to avoid uneven flows when the valves (mounted below the horizontal plate) are switched. The 4 on-off switching valves (black unit below the oven stage) are installed between the preheat and the ZLC ovens.

In this system, both the Ametek quadrupole mass spectrometer (MS) detector (behind the units to the right) and the GOW-MAC thermal conductivity detector (TCD) (mounted above the ZLC) are connected to the ZLC.

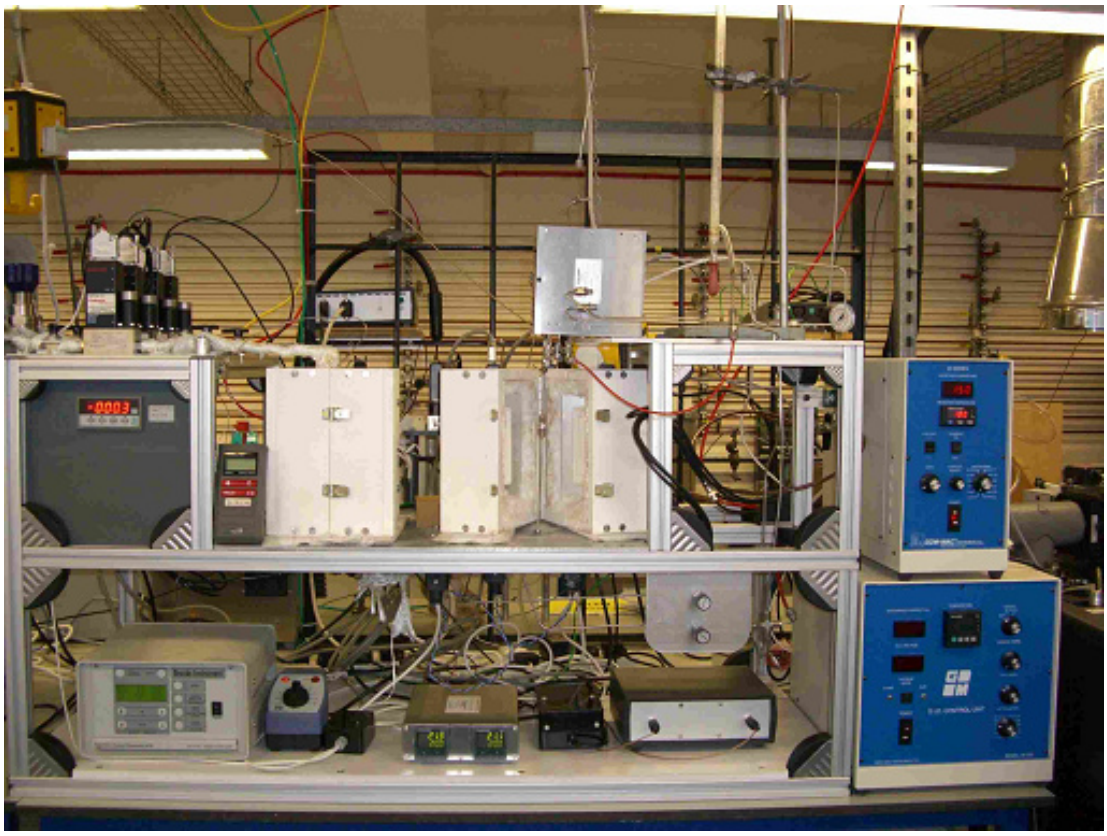

Figure 4.7 Front view of ZLC apparatus.

Compared to the traditional ZLC system, which uses a multiport switching valve, on-off switch valve can prevent the pressure change when switching flows. Moreover, the new oven can be heated up to 400ºC compared to 300 ºC of the GC oven. The ZLC cell mounted in the middle of ZLC oven is made of a Swagelok 1/8 in. union (Figure 4.8 (b)), and shown in the picture is also a thermocouple used to detect the actual temperature. The ZLC column oven has enough space, therefore the system can be easily modified to mount a larger column (grams of adsorbent) and run

breakthrough experiments. Finally, all the connections in the ZLC system were periodically inspected for leaks. The most effective procedure was to pressurize the system and to check the fittings with a soap solution.

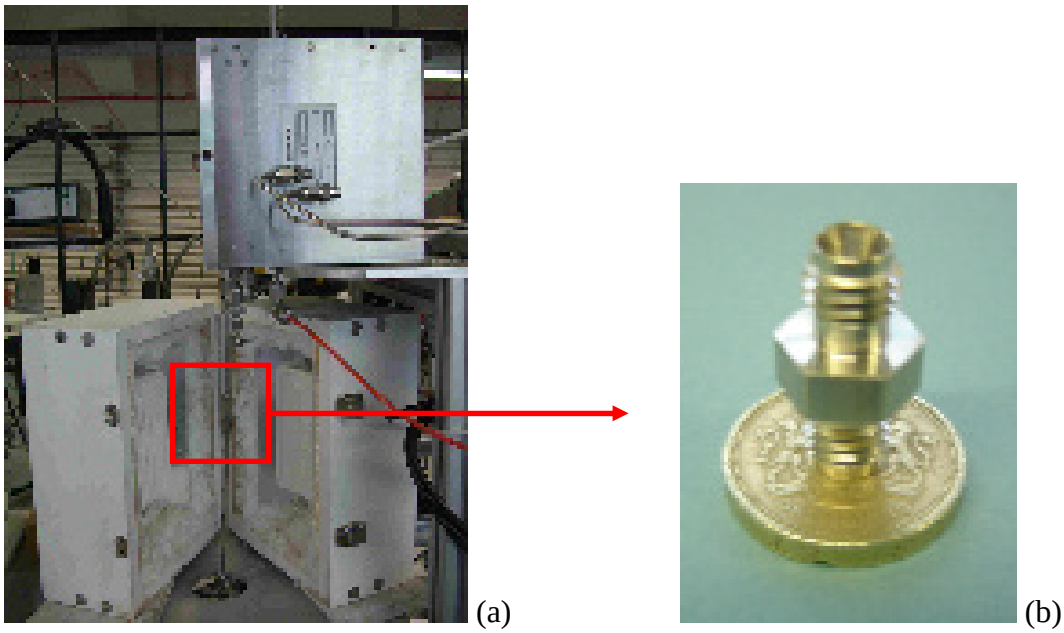

(a) (b)

Figure 4.8 Front view of the ZLC oven (a), specific view of ZLC column (b).

4.7 Semi-automated control system

The Mass flow controllers are connected to a PC and are controlled using Labview (National Instruments, USA) software. The analog signal from the TCD was connected to a PC use analog to digital convertor. When using the TCD (GOW-MAC) as the detector Labview was used to acquire real-time data. As the inlet flowrate requirement for the TCD is at least 30cc/min, as showed in Figure 4.9, the

original system configuration was sending 30cc/min of 10% CO_2 in helium to ZLC and TCD. When operating with lower flowrates, the configuration of system was modified since the TCD detector operates well at approximately 30cc/min flows. Therefore a make-up stream was added, but this diluted the concentration by up to 30 fold. The resulting response signals were very small and the signal to noise ratio was low, especially considering that the ZLC relies on a semi-logarithmic plot of the concentrations and at least two orders of magnitude of signal are needed. To resolve this, a solid state amplifier and 50 Hz mains frequency signal filter was added to boost the signal and reduce the effect of noise from the electrical supply. The signal was then further processed using a multistage noise filter in Labview (Laboratory Virtual Instrumentation Engineering Workbench) resulting in good TCD signals even for the low flowrate runs with high dilution. A flowchart of the Labview program used for real-time TCD signal monitoring, and for the automatic pre-set experimental running and recording is shown in Figure 4.10, as well as automatic thermal regeneration or thermal desorption of strongly adsorbed species.

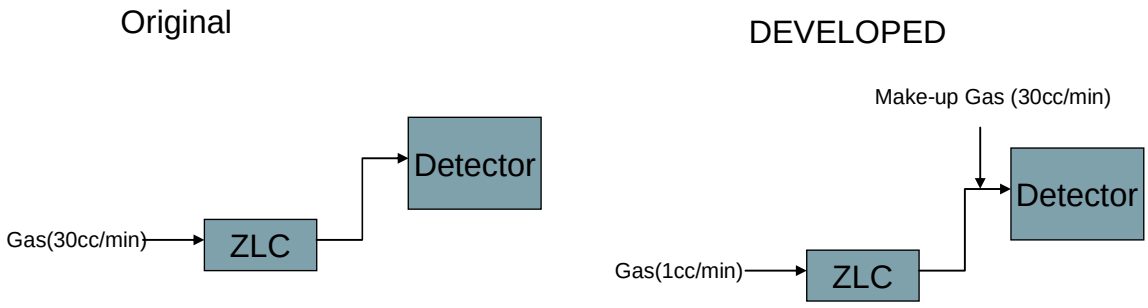

Figure 4.9 ZLC system improvements with GOW-MAC TCD detector

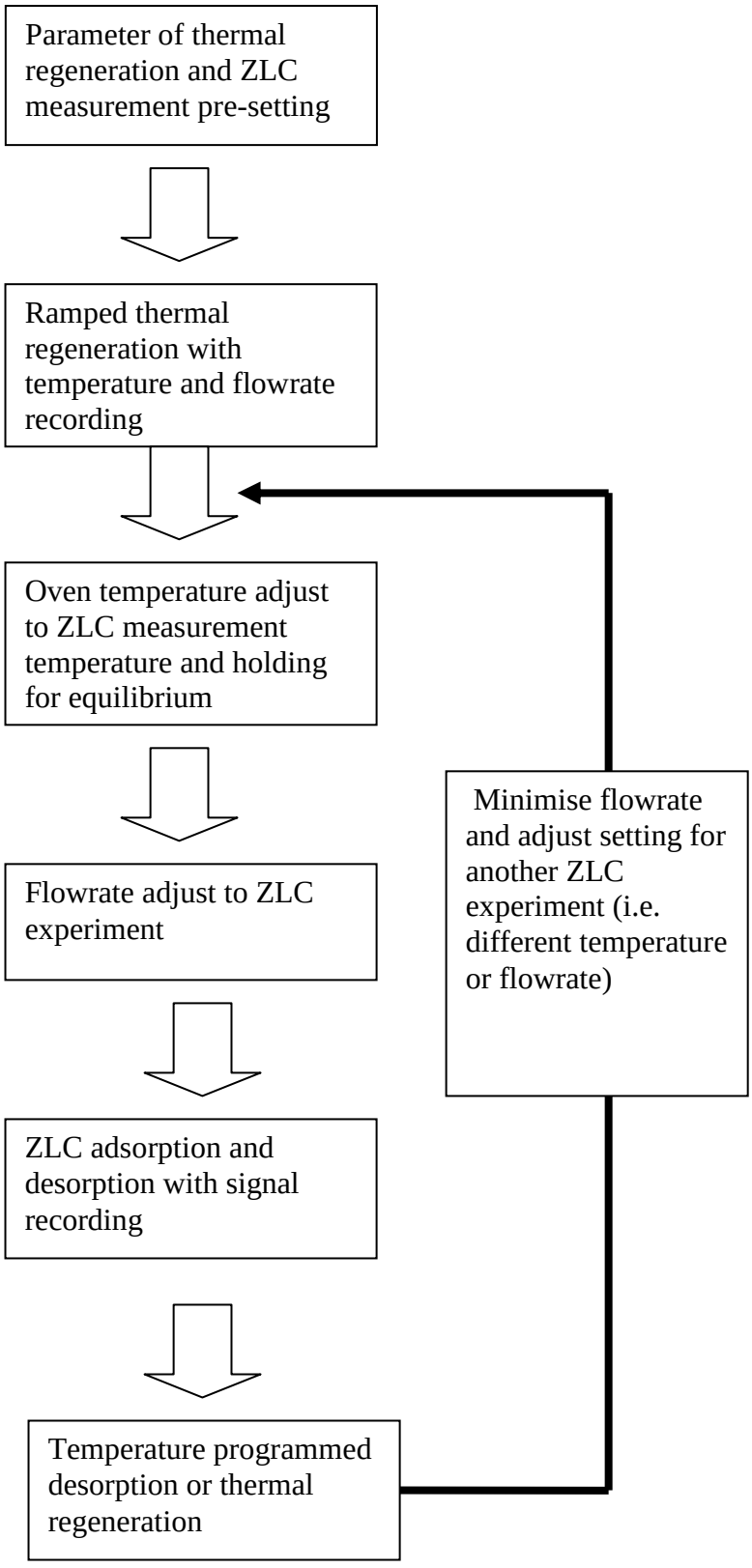

Figure 4.10 Flowchart of Labview programme for semi-automatic experiment

The interface of the Labview program used for real-time TCD signal monitoring, and for the automatic pre-set experimental running and recording is shown in Figure 4.11. The interface allowed also automatic thermal regeneration or thermal desorption of strongly adsorbed species. The semi-automated ZLC experiment takes less than an hour to measure one typical sample at a general temperature requiring only small amounts of sample. This makes the ZLC a good technique for rapid screening of novel adsorbents.

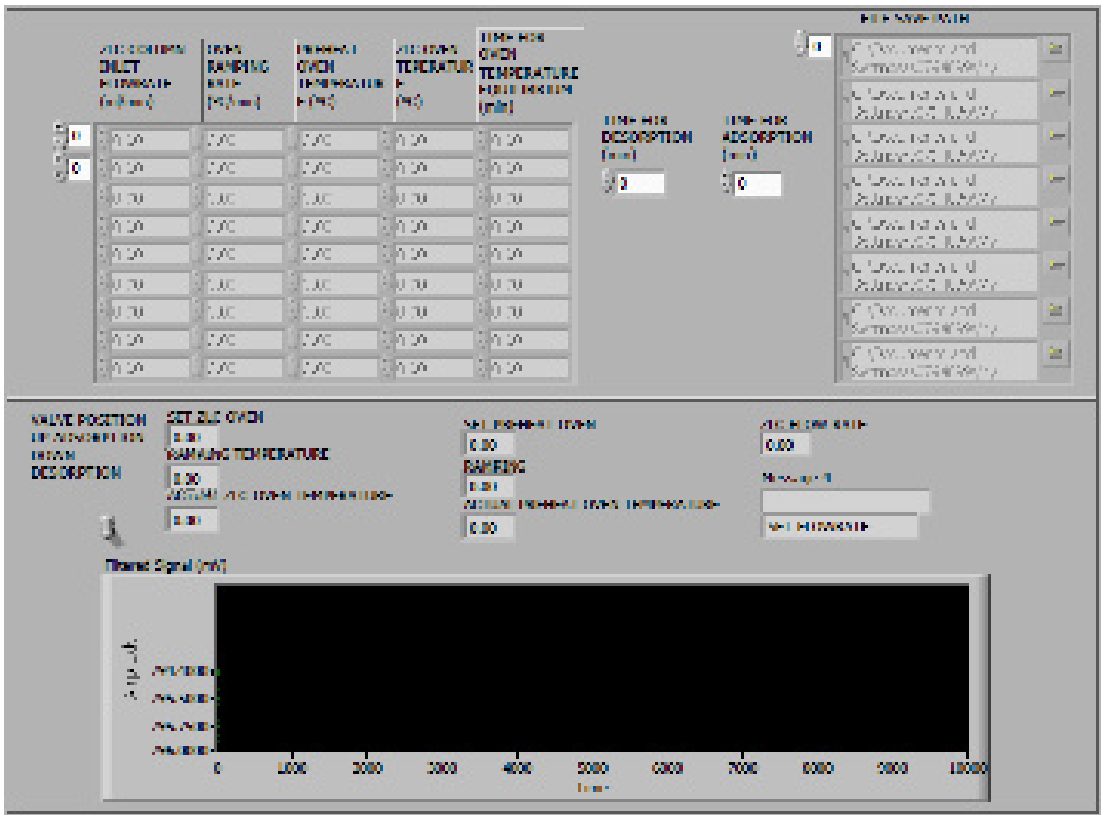

Figure 4.11 Labview interface of semi-automatic experiment setting

The original experimental response is shown in Figure 4.12 (a), and should be normalized by using the following equation:

$$\frac{c(t)}{c_0} = \frac{\sigma(t) - \sigma_\infty}{\sigma_0 - \sigma_\infty} \qquad (4.1)$$

Where σ_0 is the value of the signal at saturation level (initial level) and σ_∞ is the value of the signal when desorption is completed (baseline). This has to be carefully set when taking the baseline signal value, because it has to correspond to full desorption, otherwise the calculated adsorption capacity is not correct.

Figure 4.12 (b) shows the normalised curve with two flowrates plotted in semi-logarithmic scale.

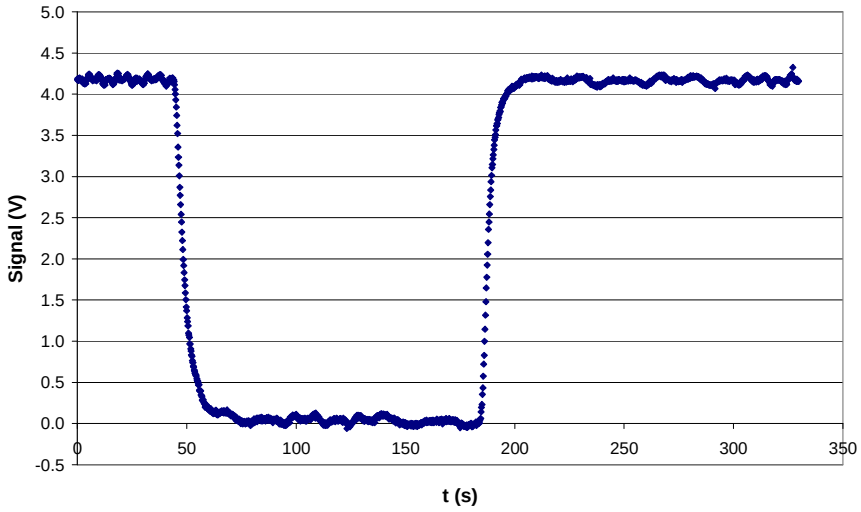

(a)

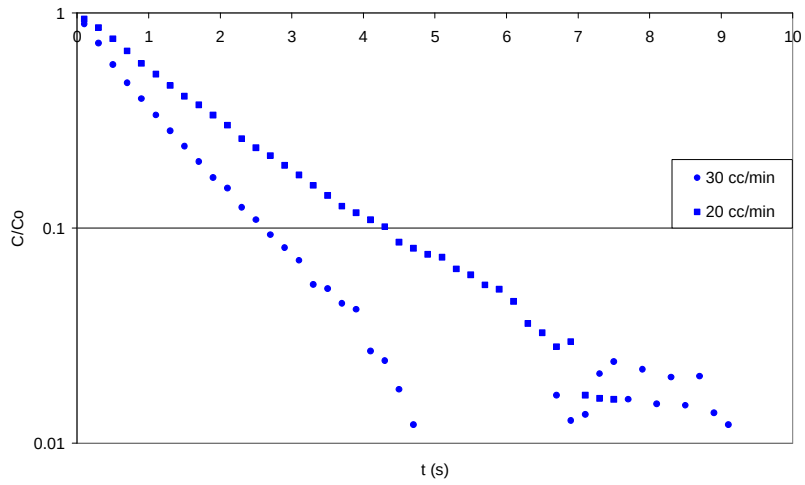

(b)

Figure 4.12 original experiment signals (a), normalised concentration vs. time plot (b)

4.8 Procedure of packing a ZLC column and typical ZLC experiment

4.8.1 ZLC column packing

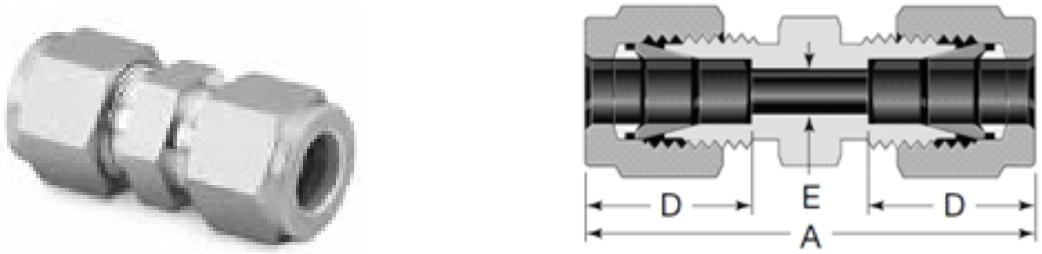

Figure 4.13 Swagelock union (A = 1.40 in, D = 0.50 in, E = 0.09 in – 1 in = 25.4 mm)

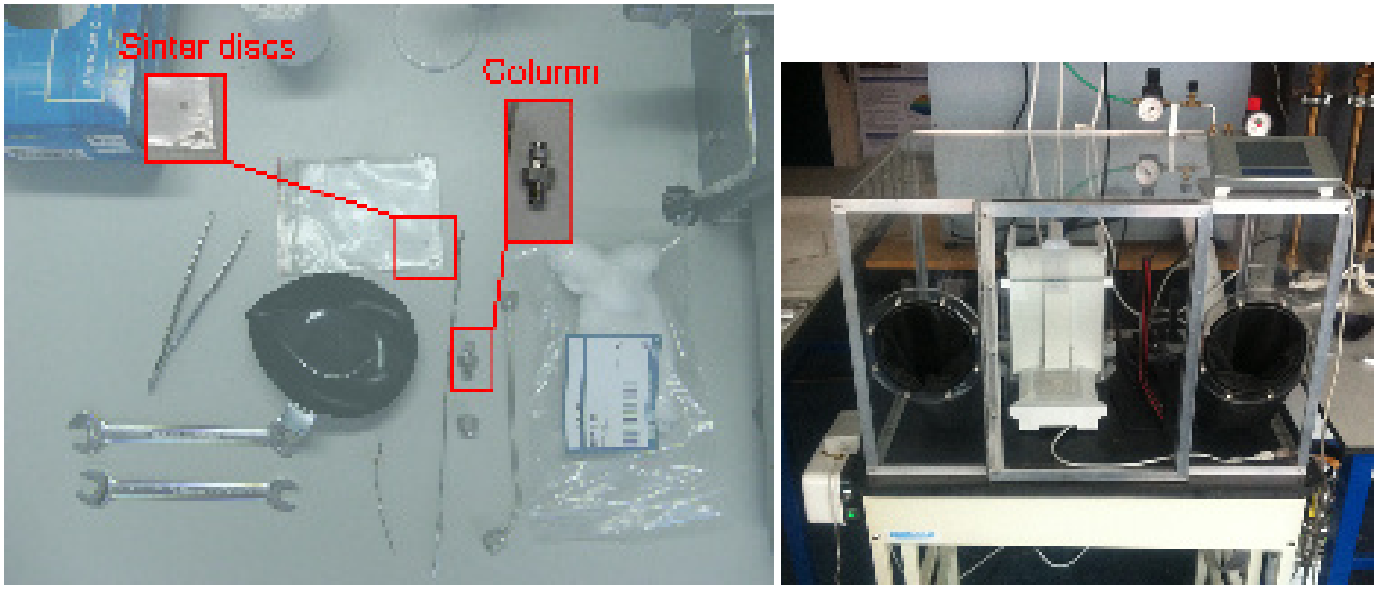

Figure 4.14 View of ZLC column and sinter disc and the glove box with balance.

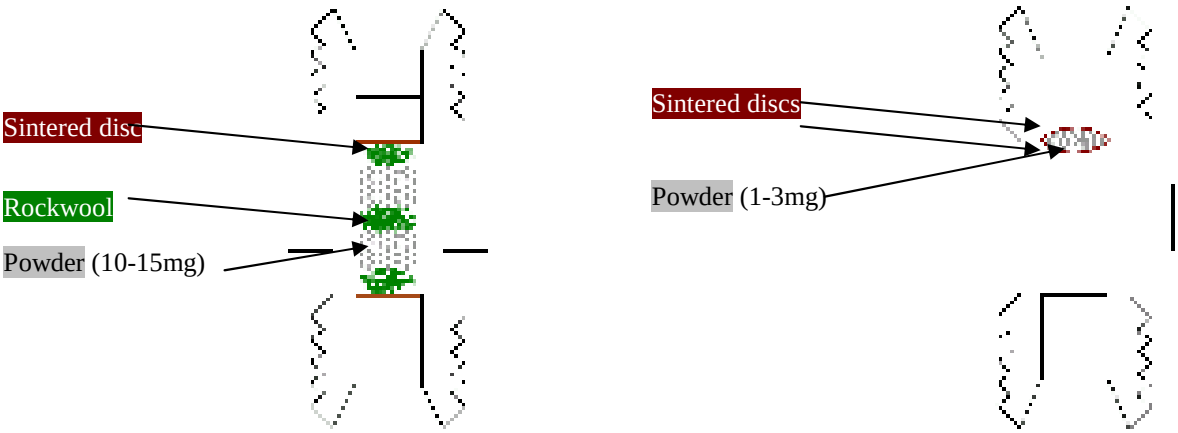

Figure 4.15 schematic of ZLC column

The ZLC is housed inside a 1/8" Swagelok union (Figure 4.13); Figure 4.14 shows the ZLC column, sinter discs (VICI, porosity of 1 micron) and the glove box (with nitrogen filled when preparing hydrophilic sample), rockwool and packing tools. A 1/8" nickel sinter disk is placed on one end of the union and made seal by tightening with a piece of tubing and a nut. After that, a layer of rockwool is placed on the sinter disc and the column is placed on a steel plate, put through an antistatic guard and weighed with a Mettler-Toledo balance to obtain the initial weight. Then 3-5 mg of adsorbent sample is loaded onto the rockwool, and another layer of rockwool is placed on the sample. After that, one more layer of sample and rockwool is loaded into the ZLC column. Finally, on the remaining open end of the union, a second disk is added to complete the cell. The result is a few layers of adsorbent material sandwiched in between the two sinter disks, the layer of rockwool is not active and can help reduce the pressure drop in the column. If the amount of adsorbent required is less than 3 mg, the powder is sandwiched directly at one end of the union by two sinter discs. To minimize the intrusion of thermal effects and/or extra particle

resistance to mass transfer, the adsorbent quantity used is small, i.e., 10−15 mg for equilibrium measurements and 1−3 mg for kinetic measurements (Shown in the Figure 4.15). This small amount of adsorbent required in the measurements is good for rapid ranking of novel adsorbents.

4.8.2 ZLC experimental procedures

In this project, by different settings, the semi-automated ZLC system was applied to carry out three different measurements: ranking of adsorbents (equilibrium control); diffusivity measurements (kinetics control); and stability tests.

• Ranking of adsorbents

Prior to the experiment, the ZLC column was regenerated with a temperature ramping rate of 1°C/min to the required temperature and then held at this temperature for a fixed period of time at a very low flow rate of the helium purge gas, i.e., 1 cc/min. After regeneration, the oven temperature is reduced to the measurement temperature and usually held for 30 minutes. This holding time should ensure that the final temperature is reached in the ZLC. During an experiment, the sample was first equilibrated with inert stream containing a known concentration of CO_2 prepared in the dosing volume. At time zero, the flow is switched to a pure helium purge stream at the same flow rate. The sorbate concentration at the outlet of the ZLC can be conveniently followed using a detector. For each sample, ZLC experimental runs at 2 different low flow rates were performed, the low flowrate

provide conditions for the ZLC desorption process to be controlled by equilibrium (low L value).

• Diffusivity measurements

In the study of diffusivity, smaller samples (i.e. 1-3 mg) are packed between two porous stainless steel sinter discs held at one end of a Swagelok 1/8 in. union. The regeneration processes and ZLC experiments were similar to the ranking experiments. To reach kinetic control; high flow rates (10-50cc/min) were used. To measure the kinetics of pelletized samples, the dimension of the sample was first measured and then packed inside the column with sinter discs on both ends of the Swagelok union.

• Stability measurements

In stability measurements, the dosing volume was applied to prepare certain concentrations of water vapour in the gas mixture. After regeneration of fresh samples, normal ZLC runs were first carried out with known concentration of CO_2 to check the original adsorption capacity. After a certain time of exposing the sample to mixtures gas, the sample was regenerated and normal ZLC was then repeated. This is allowed to measure to check the residual CO_2 adsorption capacity. Several exposure runs were applied on the sample until the sample ether did not show a residual capacity or had a stable capacity.

4.9 ZLC system modification during project

The dead volume (V_g) in the ZLC system represents the sum of the volume of the cell and the volume of the piping between the switching valves and the detector. V_g is determined by performing a ZLC experiment with no adsorbent in the column. For strong adsorbed components, the dead volume can be negligible but for low capacity adsorbents, V_g needs to be taken in account for calculating the accurate capacity, and also, for measuring the diffusivity. Blank experiments are quite important. In Figure 4.16 the blank response curves are shown for the new ZLC system. The length of the pipe between the ZLC oven and the detector was first reduced. After modification, the detector was connected directly to the outlet of the ZLC oven – this is indicated a "no external pipe" in Figure 4.16. It is clear that the blank volume has been reduced significantly, but the tail is still a problem. Therefore to improve the blank response, the source of the long tail was found in the switching valves. At very low flow rates, the volume in the valves plus a short pipe becomes a Stefan diffusion tube. After adding a fitting inside the switching valve to reduce the volume, the blank response improved to the point where accurate adsorption capacity measurements were possible.

An on-line quadrupole mass spectrometer (Ametek Quadrupole Gas Analalyzer Model No. TMU 071 P) with a turbomolecular pump plus a diaphragm pump) was installed and connected to the ZLC system in order to provide the capability of carrying out binary experiments of CO_2 adsorption in the presence of water or other impurities. The gas leaving the cell is sampled continuously through a silica capillary

(heated to 180ºC by a heating jacket) connected to the chamber of the mass spectrometer.

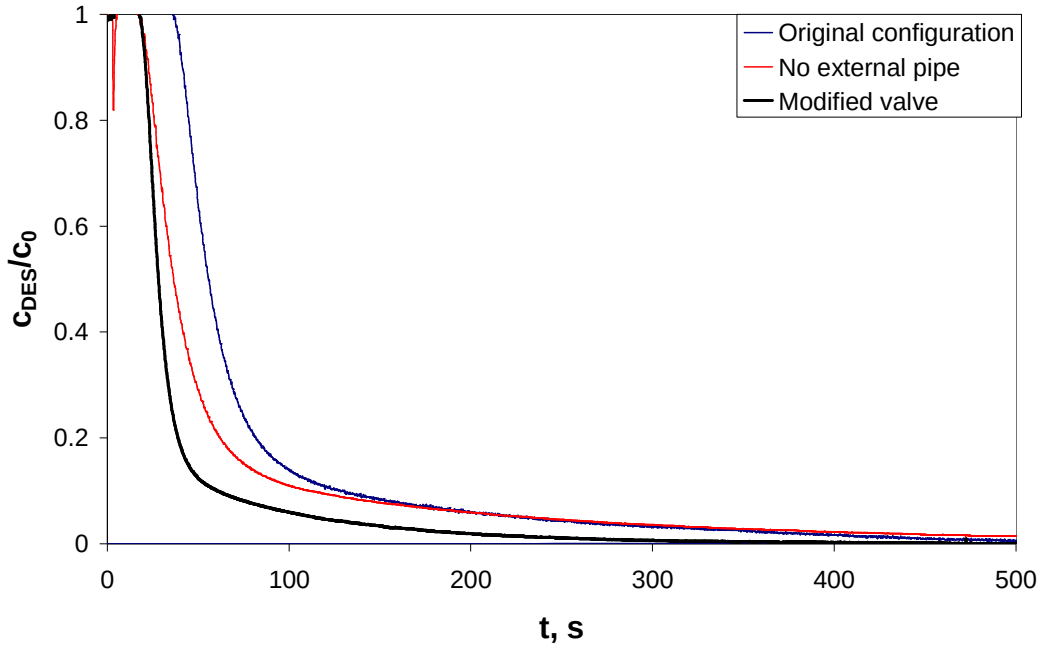

Figure 4.16 System blank improvements (linear plot)

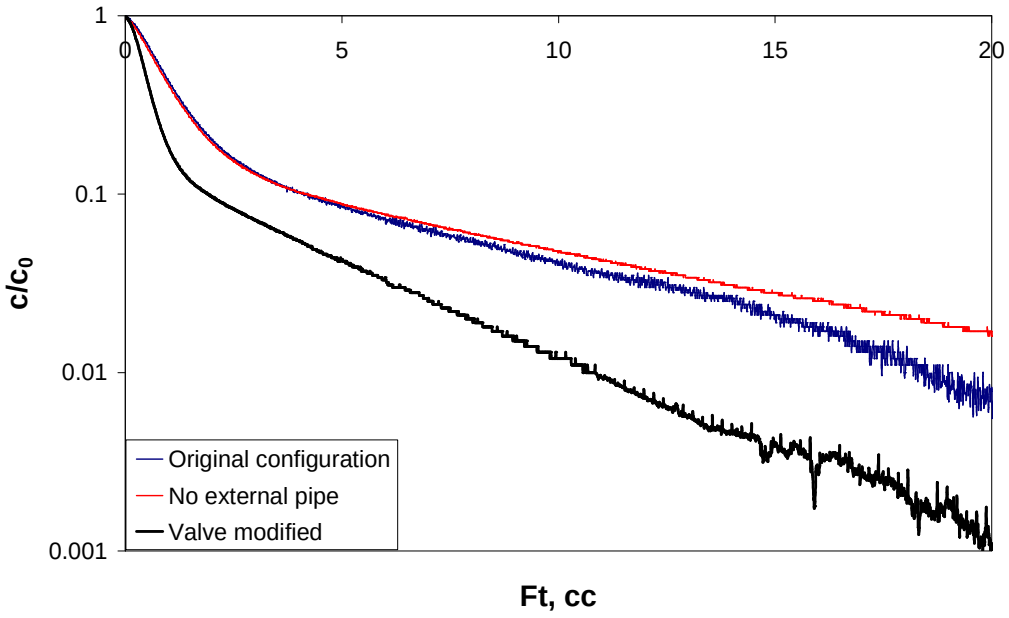

Figure 4.17 System blank improvements (semi-logarithmic plot)

Figure 4.18 shows the comparison of the blanks measured using the TCD and the new MS and the improvement of MS response by varying the capillary diameter. The MS has an overlapped response with the TCD curve by using a 0.06mm OD capillary in the blank experiment. What is important also is the fact that since the capillary to the Ametek MS requires less than 1 cc/min of sample, there is no need to add a make-up gas flow as for TCD detector so the signal is not diluted. Special care needs to be taken at the lower flows to avoid the possibility of back flow or diffusion of air into the ZLC system. To avoid this, a short section of 1/16" tubing was added at the outlet and masses 32 and 28 were monitored with the MS to check for air leaks.

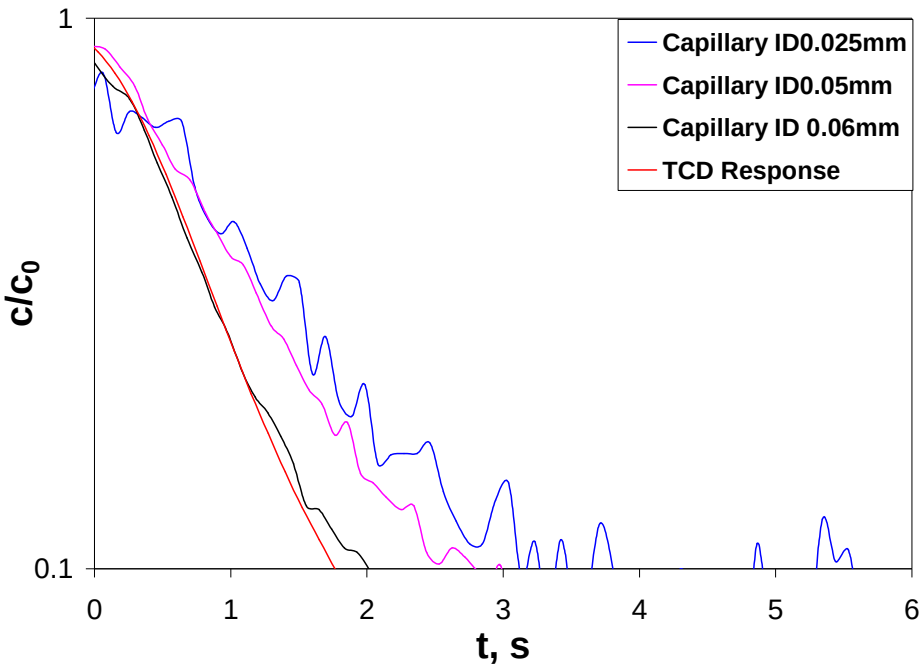

Figure 4.18 ZLC responses of blank runs with the two detectors.

Figure 4.19 shows the check of the system using 5A. Once the difference in the blanks is accounted for, the CO_2 measured by both detectors is effectively the same.

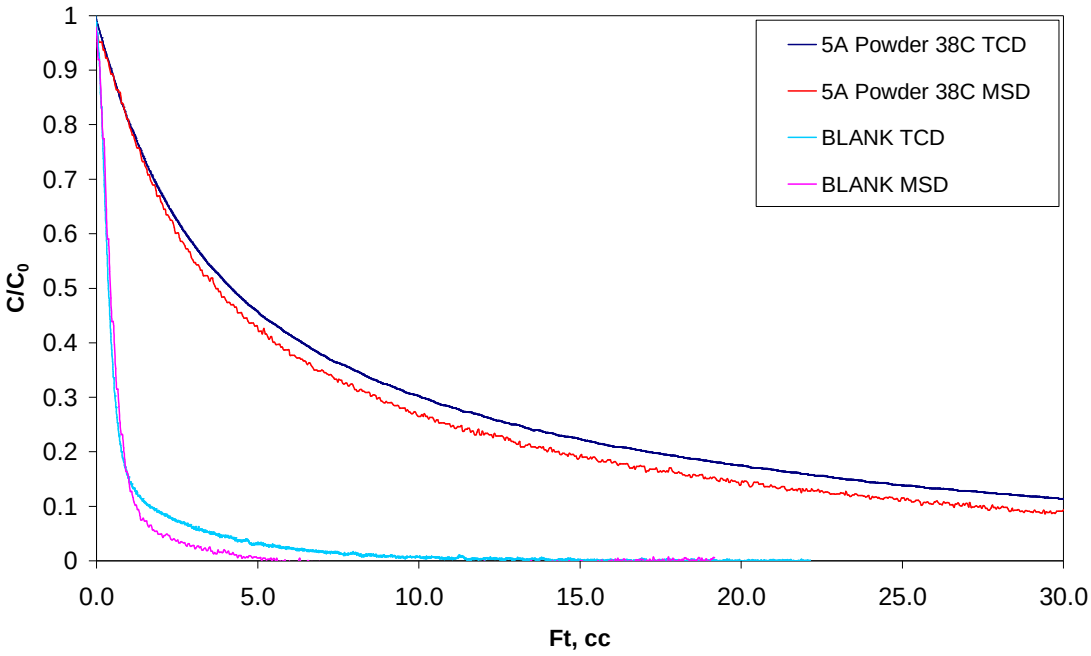

Figure 4.19 Comparison of the two detectors on 5A zeolite.

For pure CO_2 capacity ranking, the TCD is quite satisfactory, and the Ametek quadrupole mass spectrometer is developed for the multi-component system studies (stability tests). The MS can be used also to monitor the sample regeneration to check if the regeneration is complete. Figure 4.20 shows an example of the water signal monitored on the MS upon regenerating a MOF Ni/DOBDC sample at 125 °C and 3cc/min by dry helium flow. From Figure 4.20 it is clear that more than 4 hours are needed to regenerate properly the sample. The MS can also be used to do a composition scan as shown in Figure 4.21. In this way, the by-products coming out from the sample during regeneration can be monitored. If the regeneration temperature is too low, then residual water or solvent may not come out; or if it is too high, then the sample can be deactivated or has decomposed)

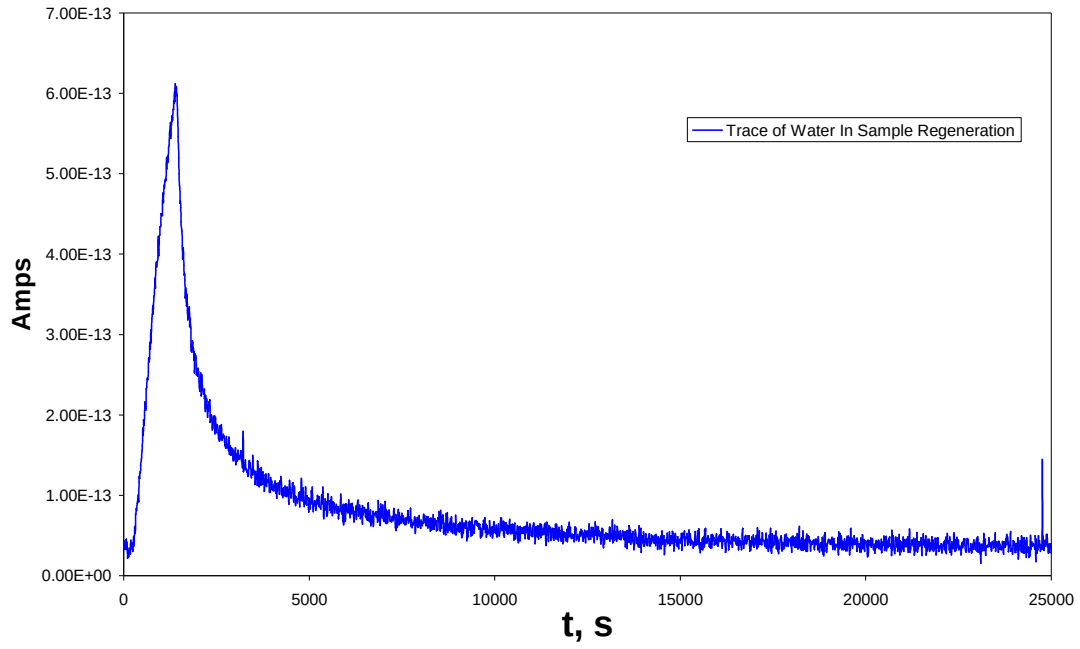

Figure 4.20 an example of the regeneration of Ni/DOBDC.

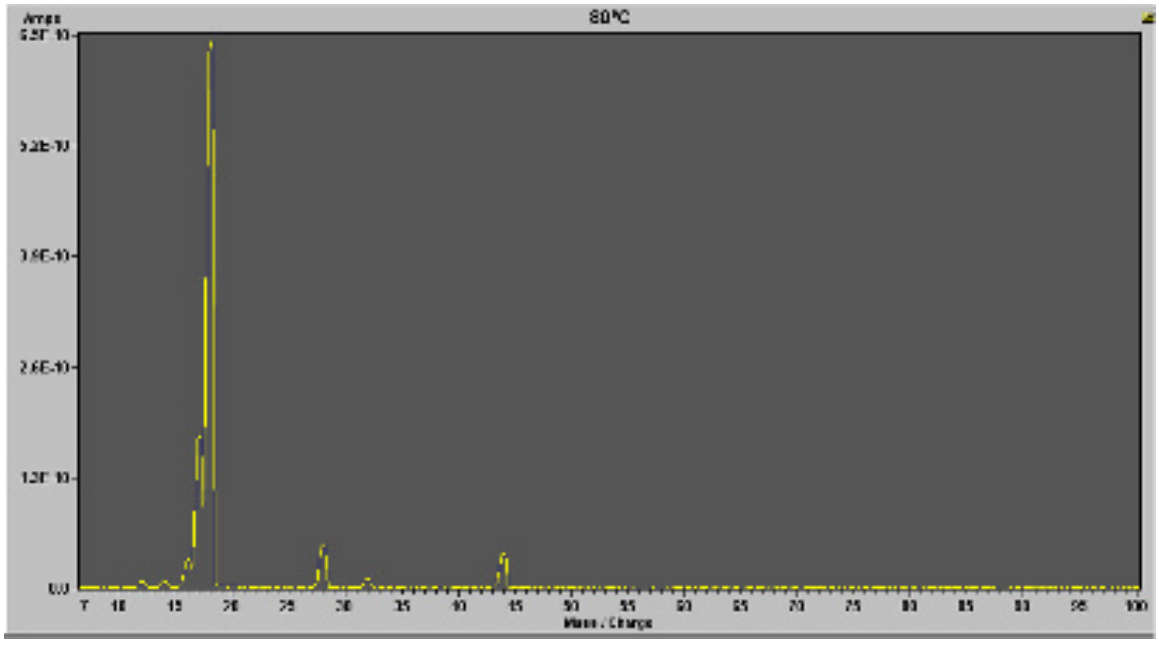

Figure 4.21 composition scan of outlet by mass spectrometer.

CHAPTER 5

5. RAPID RANKING OF ADSORPTION CAPACITY

5.1 Introduction

MOFs show potential in becoming good candidates for separation processes; however, even if some MOF materials have good CO_2 uptake, it is more important to understand CO_2 adsorption in MOF materials in the low pressure region than at high pressures for their applications to remove CO_2 from flue gases [43, 67, 68]. Typical cooled flue gases from fossil fuel-fired plants contain 3 to 16% CO_2 by volume at ambient conditions and 37.8 º C (100ºF), the low partial pressure and high flow rates make this a challenging separations problem [6, 69-71]. There are almost unlimited MOFs and other adsorbents can be synthesized. However, a good candidate for carbon capture should have desirable characteristics, especially good working

capacity; since pure CO_2 adsorption equilibrium measurement on materials is the most fundamental step for their application as CO_2 adsorbents. This chapter will show how the developed ZLC system can be used for ranking CO_2 capacity of novel adsorbents. In the adsorbents ranking part, the point of interest, 10% CO_2 by volume in 1 bar at 38ºC (the anticipated partial pressure of CO_2 and temperature in flue gas) was selected as the ZLC standard conditions.

5.2 Adsorbent synthesis

Most MOF materials in the project were synthesized through solvothermal reactions. The synthesis procedures for the MOF samples used in our research are modified from the literature [72]. Both the MOFs and the commercial zeolite are supplied by UOP (Des Plaines, Illinois) and the University of Michigan. Here are list the process and conditions for adsorbents in the project. The adsorbents tested in the projected were selected by the UOP, based on the literature research, the selected sample are having potential to capture CO_2 from flue gas.

Mg/DOBDC was synthesized by the Matzger group at the University of Michigan [73]. Linker precursor 2, 5-dihydroxyterephthalic acid (2.98 g) was dissolved in 180 mL 1-methyl-2-pyrrolidinone (NMP) + 20 mL deionized water using sonication. Mg (OAc) 2. $4H_2O$ (6.44 g) was added to a 0.5 L jar. The 2, 5-dihydroxyterephthalic acid solution was filtered into the jar. The solution was sonicated to dissolve completely the magnesium acetate and the jar was placed in a 120 °C oven for 20 hours. The mother liquor was decanted while still hot and the yellow solid was washed with

methanol (3 × 200 mL). The methanol was decanted and replaced with fresh methanol (200 mL) 3 times over the course of 3 days. The yellow solid was evacuated at 250 °C for 16 hours and then transferred to a glove box for storage. One batch produced ~3 g of Mg/DOBDC.

Ni/DOBDC [74], nickel(II) acetate (18.7 g, 94.0 mmol, Aldrich) and 2,5-dihydroxyterephthalic acid (DOBDC, 37.3 g, 150 mmol, Aldrich) were placed in 1 L of mixed solvent consisting of equal parts tetrahydrofuran (THF) and deionized water. The mixture was then put into a 2 L static Parr reactor and heated at 110 °C for 3 days. The as-synthesized sample was filtered and washed with water. Then the sample was dried in air, and the solvent remaining inside the sample was exchanged with ethanol 6 times over 8 days. Finally, the sample was activated at 150°C under vacuum with nitrogen flow.

Co/DOBDC [74], the reaction of cobalt(II) acetate and 2,5-dihydroxyterephthalic acid ($C_8H_6O_6$) in a mixture of water and tetrahydrofuran (molar ratio 2:1:556:165) under autogenous pressure at 110°C in a Teflon-lined autoclave (50% filling level). This yielded a pink-red, needle-shaped crystalline substance $[Co_2(C_8H_2O_6)(H_2O)_2]8H_2O$. After the hypothetical removal of the noncoordinating solvent molecules in the channels, the empty channels occupy 49 % of the total volume of the unit cell, and the average cross-sectional channel dimensions are 11.08×11.08 $Å^2$. The empty volume increases to 60% if the coordinating water is also removed. The water molecules excluding and including the coordinating water account for 29.2% and 36.6% of the mass, respectively.

HKUST-1(Cu-BTC) [42] was produced by an electrochemical procedure, which is a new synthetic method compared to the previously reported synthesis under hydrothermal conditions. The crystals obtained have double sided pyramidal shape and a size of maximum 6 μm.

The ZIF-8 pellets and Z1200 powder were made by and purchased from BASF.

The 5A and Silicalite power and 13X pellet were supplied by UOP, 13X-APG adsorbent is the sodium form of the Type X molecular sieve and an alkali metal aluminosilicate. 13X-APG adsorbent will adsorb molecules with critical diameters up to 8 angstroms.

Since the MOFs are potential candidates for CO_2 capture from flue gas. In order to assess the stability of MOFs as adsorbents for long term usage, steam was used to condition the Ni/DOBDC MOF samples. The steaming work on the MOFs was carried out by UOP. Hydrothermal stability was achived in an "accelerated" manner by exposing MOFs to steam at significantly higher concentration and at higher temperature than would be expected in the flue gas application. After the solvent-exchanged, dried MOF material was used as received (if in powder form) or placed through a mesh screen if the material contains chunks. A small quantity (< ½ cm height) was loaded into each of the quartz tubes and the material is heated to a specified temperature (150°C) overnight in flow of nitrogen. The tubes are allowed to cool to the designated steam temperatures (100°C), and steam (in nitrogen) is

introduced at the desired level (5%, 10% and 15%) for 2 hours. Each tube is maintained at 60 °C in the absence of steam for 1 hour before being quickly removed from the oven and loaded into a GADDs XRD plate.

Some samples were also formed into pellets, Palletised Ni and Mg MOF samples were pressed from pure powder samples without any binder, and Ni/DOBDC extrudate was made from powder which was first mixed with solvent and then extruded by syringe. After proper drying, the extrudate was formed. CO_2 capacity were measured by ZLC and compared for the samples before and after these processes.

5.3 ZLC ranking measurements conditions

In the capacity ranking experiment, a mixture of 10% CO_2 in helium was prepared. Low flowrates were applied to the measurement to make the system reach equilibrium control. Prior to the experiment, the sample was thermally regenerated at the required temperature (Table 5.1). Through this activation procedure, still occluded solvent molecules and adsorbed moisture were removed. After regeneration, the oven temperature was reduced to the ZLC experiment temperature (i.e. 38°C or 50°C, 65°C) and the ZLC measurements were carried out.

Table 5.1 Regeneration conditions of adsorbents.

Adsorbents	**Regeneration conditions**
Ni/DOBDC powder	110 ^{o}C, 3cc/min Helium Flow, 1h then 150^{o}C,3cc/min Helium Flow, 12h
Ni/DOBDC pellet	110 ^{o}C, 3cc/min Helium Flow, 1h then 150^{o}C,3cc/min Helium Flow, 12h
Ni/DOBDC powder 5% steam	110 ^{o}C, 3cc/min Helium Flow, 1h then 150^{o}C,3cc/min Helium Flow, 12h
Ni/DOBDC powder 10% steam	110 ^{o}C, 3cc/min Helium Flow, 1h then 150^{o}C,3cc/min Helium Flow, 12h
Ni/DOBDC powder 15% steam	110 ^{o}C, 3cc/min Helium Flow, 1h then 150^{o}C,3cc/min Helium Flow, 12h
Ni/DOBDC powder room temperature regeneration	25 ^{o}C, 3cc/min Helium Flow, 12h
Ni/DOBDC extrudate	110 ^{o}C, 3cc/min Helium Flow, 1h then 150^{o}C,3cc/min Helium Flow, 12h
Co/DOBDC powder	110 ^{o}C, 1cc/min Helium Flow, 1h then 125^{o}C,1cc/min Helium Flow, 12h
Mg/DOBDC powder	110 ^{o}C, 3cc/min Helium Flow, 1h then 200^{o}C,3cc/min Helium Flow, 12h
Mg/DOBDC pellet	110 ^{o}C, 3cc/min Helium Flow, 1h then 200^{o}C,3cc/min Helium Flow, 12h
Cu-BTC powder	110 ^{o}C, 1cc/min Helium Flow, 1h then 150^{o}C,1cc/min Helium Flow, overnight
ZIF-8 pellet	Room temperature + 1cc/min Helium Flow, 5h then 260^{o}C + 1cc/min Helium Flow, overnight
13X pellet	110 ^{o}C, 3cc/min Helium Flow, 1h then 300^{o}C, 3cc/min Helium Flow , 15h
5A powder	110 ^{o}C, 3cc/min Helium Flow, 1h then 400^{o}C, 3cc/min Helium Flow , 12h
Silicalite powder	110 ^{o}C, 3cc/min Helium Flow, 1h then 400^{o}C, 3cc/min Helium Flow , 6h
Z1200 powder	Room temperature + 1cc/min Helium Flow, 5h then 260^{o}C + 1cc/min Helium Flow, overnight
IRMOF-1 powder	110 ^{o}C, 3cc/min Helium Flow, 1h then 200^{o}C,3cc/min Helium Flow, 12h

5.4 Results and discussion

5.4.1 Ranking of materials

Table 5.2 Adsorbents ranking value at point of interest (0.1 bar CO_2 at 38ºC)

Adsorbents	**Page NO.**	**CO_2 capacity at 0.1 bar, 38ºC (mol/kg)**	**Isotherm shape**	**ΔH (kJ/mol)**
13X pellet	83	3.2	Non-Linear	37
Ni/DOBDC powder	82	2.814	Linear	38
Ni/DOBDC steamed pellet	83	2.062	Linear	
Ni/DOBDC powder 5% steam	84	2.363	Linear	
Ni/DOBDC powder 10% steam	84	0.41	Linear	
Ni/DOBDC powder 15% steam	85	0.44	Linear	
Ni/DOBDC powder room temperature regeneration	85	0.45	Linear	
Ni/DOBDC extrudate	86	1.891	Linear	
Co/DOBDC powder	86	1.66	Linear	
Mg/DOBDC powder	87	4.647	Non-Linear	44
Mg/DOBDC pellet	87	4.323	Non-Linear	
Cu-BTC powder	88	0.294	Linear	
ZIF-8 pellet	88	0.1	Linear	
5A powder	89	2.274	Non-Linear	
Silicalite powder	89	0.204	Non-Linear	
Z1200 powder	90	0.15	Linear	
IRMOF-1 powder	90	0.13	Linear	

Table 5.2 shows the ranking results information for all the adsorbents, Figure 5.1, 5.2, 5.3 and 5.4 show the typical normalised c/c_0 vs. t plot and c/c_0 vs. Ft plots for

Ni/DOBDC MOF and 13X zeolite from the ZLC experiment for CO_2 response at 0.1 bar and 38°C. The overlap of curves in the Ft plot shows that the system approaches equilibrium and the desorption rate is controlled by the convective flow. There is no useful kinetic information under these measurement conditions. From the Ft plot it is quite clear that the response of Ni/DOBDC is close to linear in the semi-logarithmic plot which indicates a linear isotherm but the 13X zeolite presents a clear non-linearity. Figures 5.5-5.19 show the experimental Ft plot for all other adsorbents which confirmed that the system was under equilibrium control.

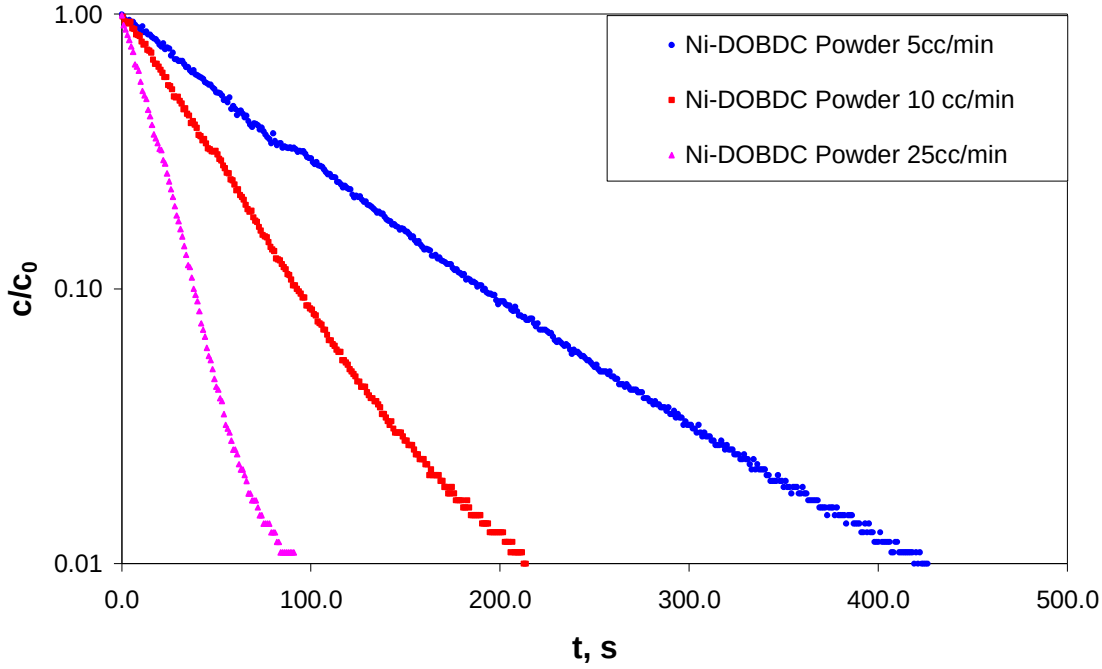

Figure 5.1 Experimental ZLC response curves of Ni/DOBDC powder at 0.1bar of CO_2 in Helium, 38 °C, 5, 10, 25cc/min

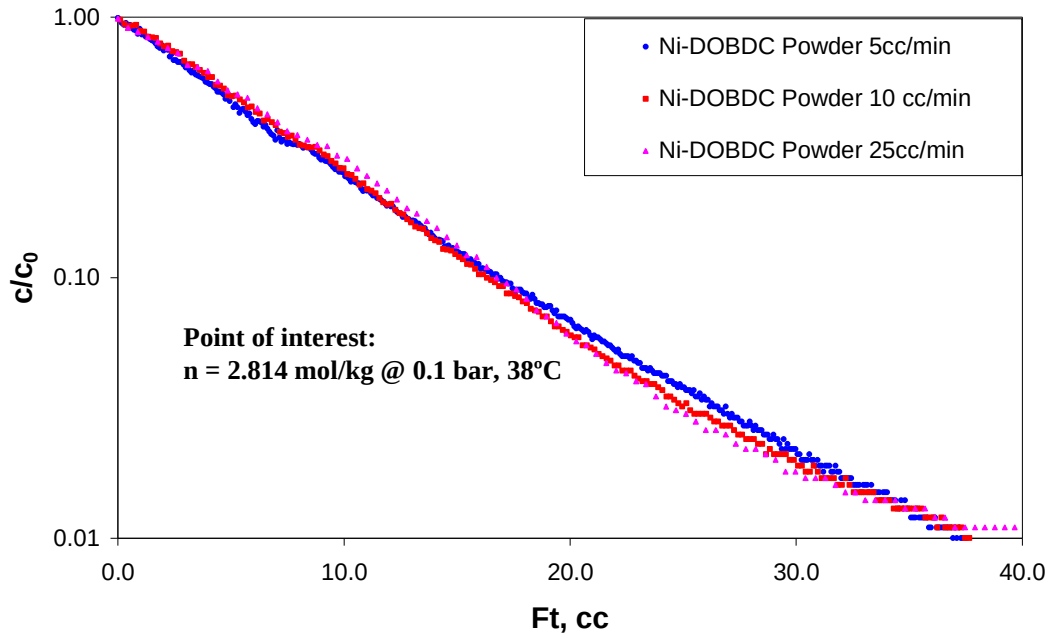

Figure 5.2 Experimental Ft plot of Ni/DOBDC powder at 0.1bar of CO_2 in Helium, 38 °C, 5, 10 and 25 cc/min

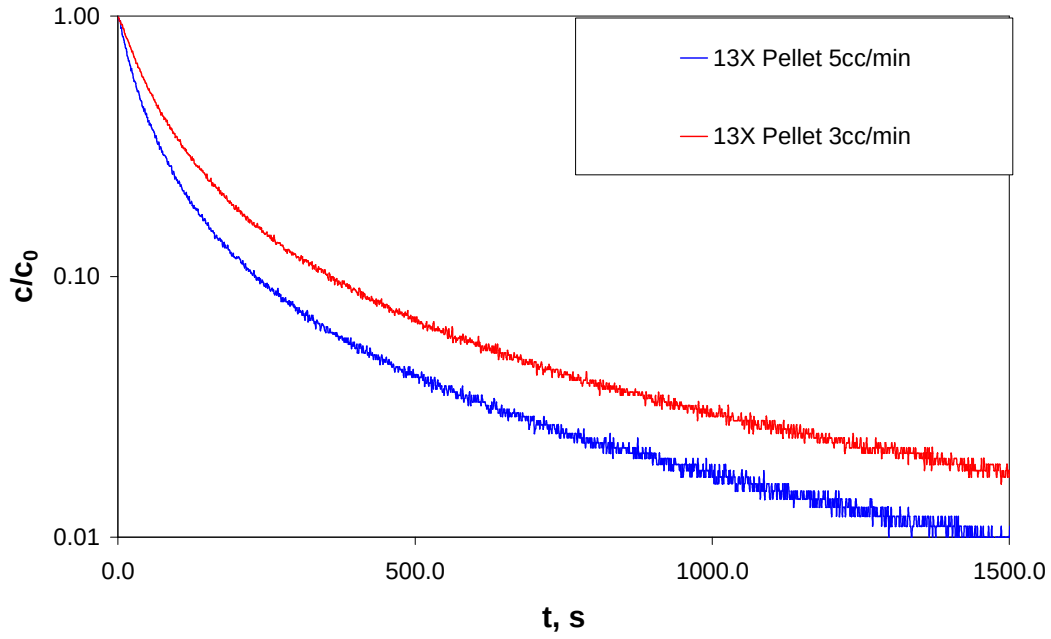

Figure 5.3 Experimental ZLC response curves of 13X pellet at 0.1bar of CO_2 in Helium, 38 °C, 3 and 5 cc/min

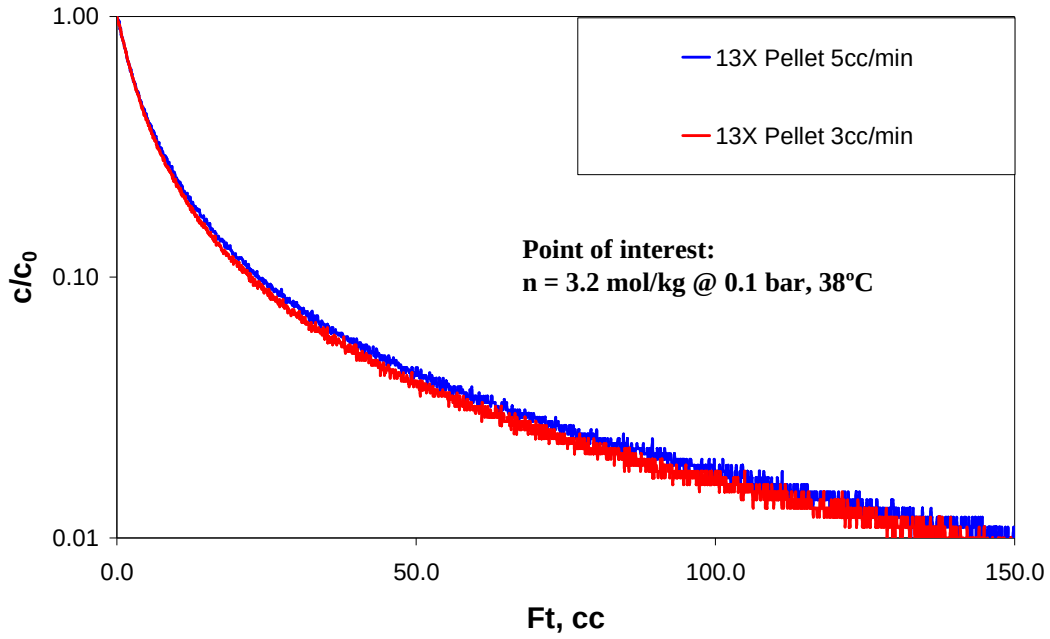

Figure 5.4 Experimental Ft plot of 13X pellet at 0.1bar of CO_2 in Helium, 38 °C, 3 and 5 cc/min.

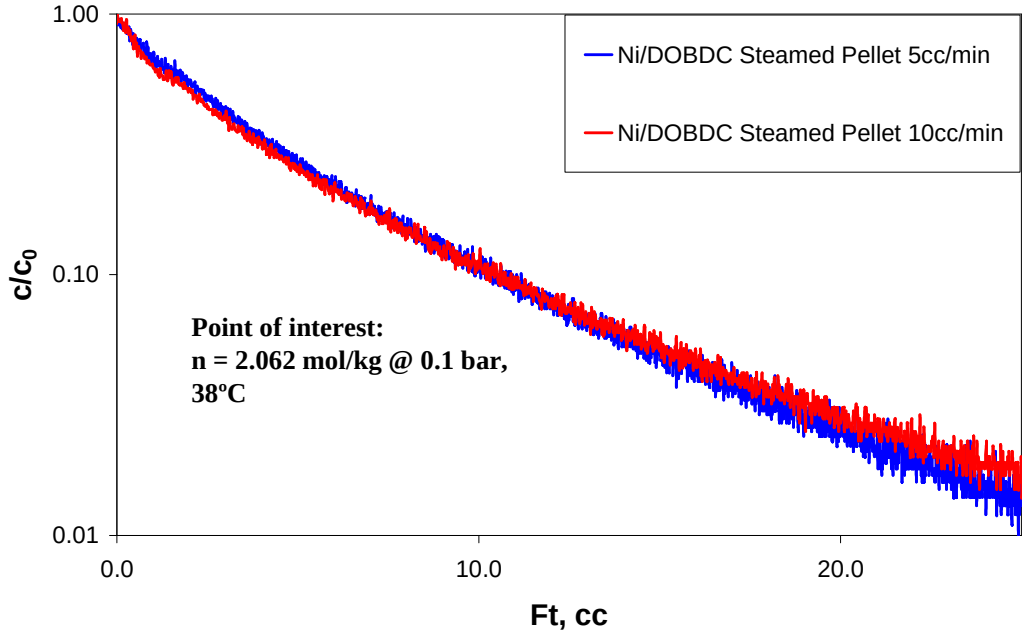

Figure 5.5 Experimental Ft plot of Ni/DOBDC pellet at 0.1bar of CO_2 in Helium, 38°C, 5 and 10 cc/min.

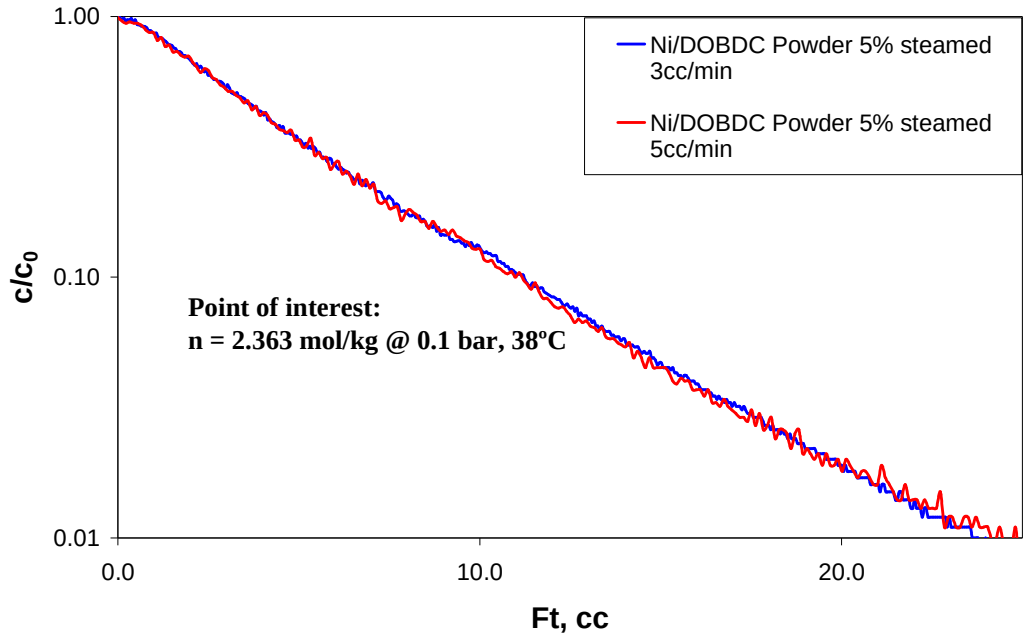

Figure 5.6 Experimental Ft plot of Ni/DOBDC powder 5% steamed at 0.1bar of CO_2 in Helium, 38 °C, 3 and 5 cc/min.

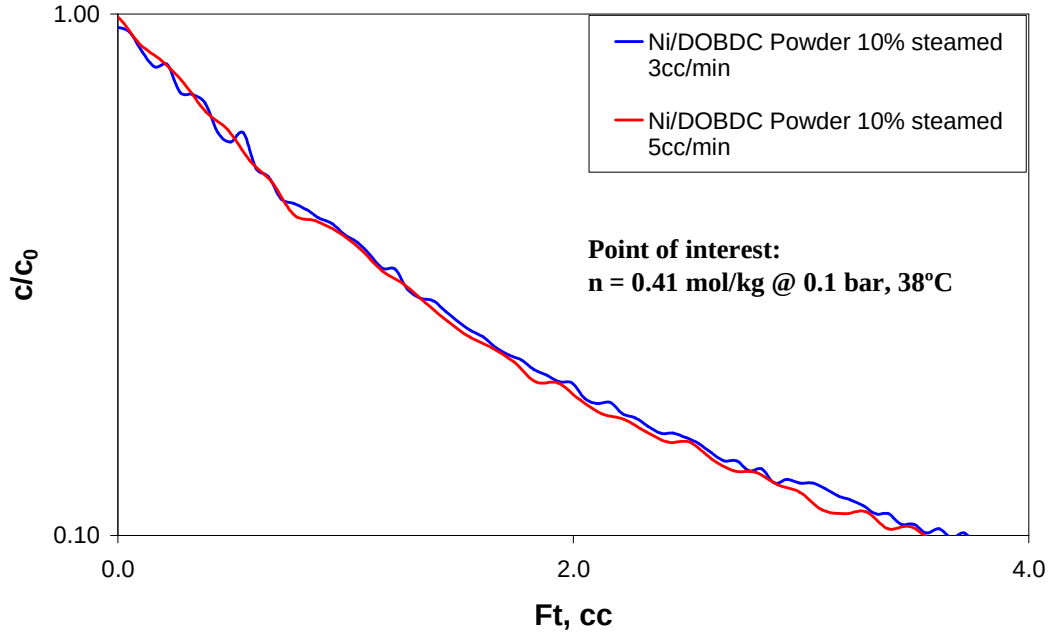

Figure 5.7 Experimental Ft plot of Ni/DOBDC powder 10% steamed at 0.1bar of CO_2 in Helium, 38 °C, 3 and 5 cc/min.

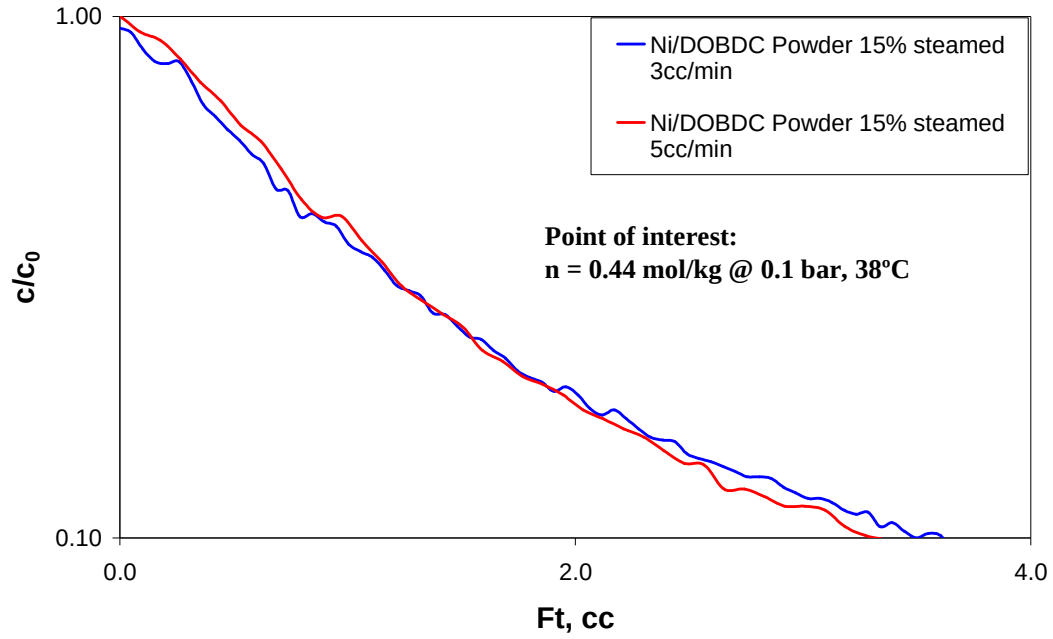

Figure 5.8 Experimental Ft plot of Ni/DOBDC powder 15% steamed at 0.1bar of CO_2 in Helium, 38 °C, 3 and 5 cc/min.

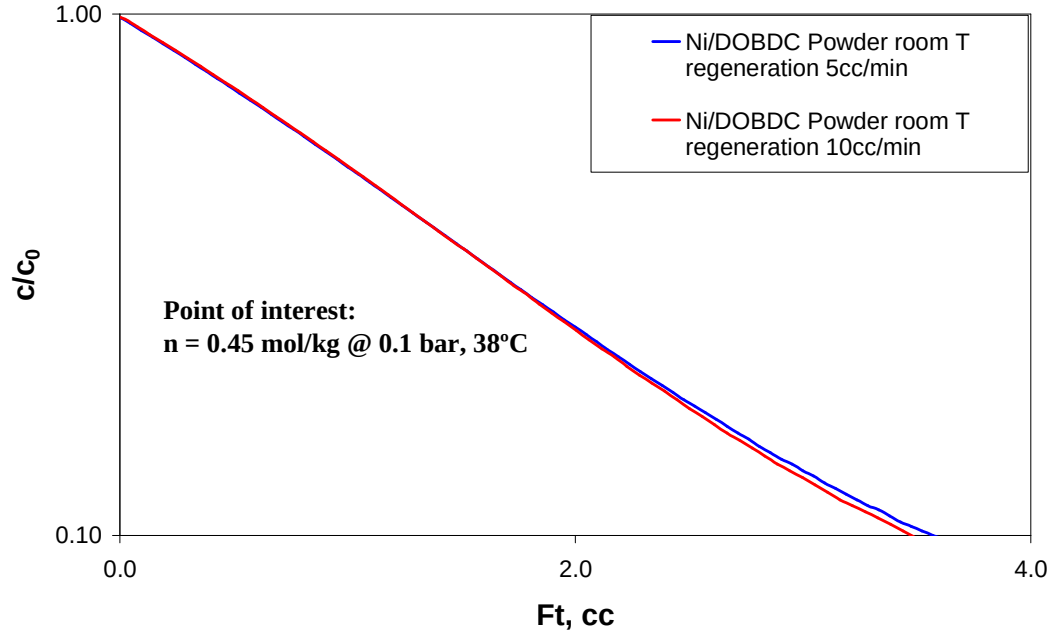

Figure 5.9 Experimental Ft plot of Ni/DOBDC powder regeneration at ambient temperature at 0.1bar of CO_2 in Helium, 38 °C, 5 and 10 cc/min.

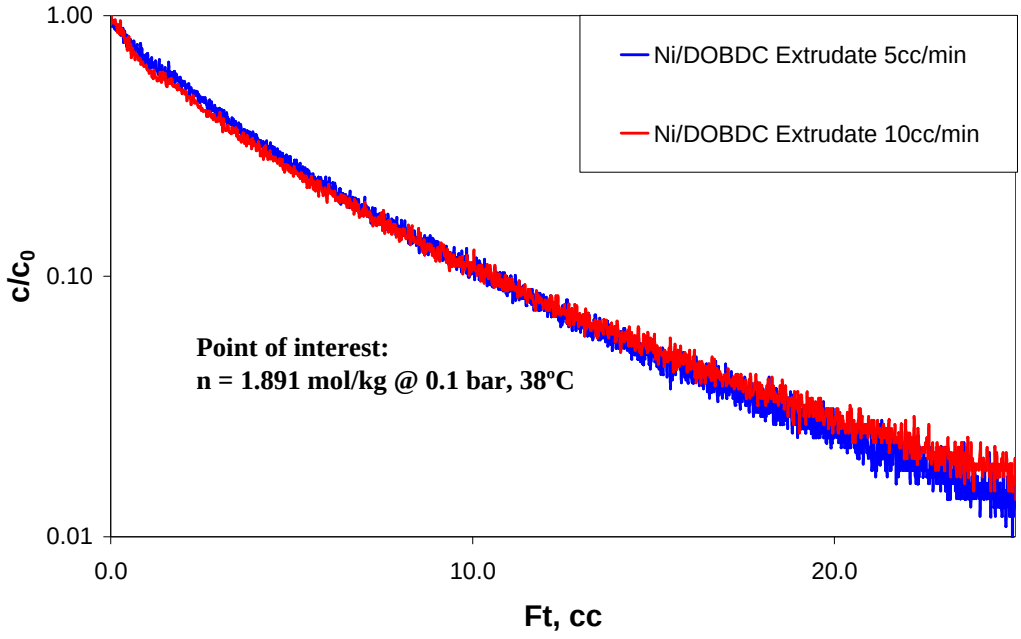

Figure 5.10 Experimental Ft plot of Ni/DOBDC extrudate at 0.1bar of CO_2 in Helium, 38 °C, 5 and 10 cc/min.

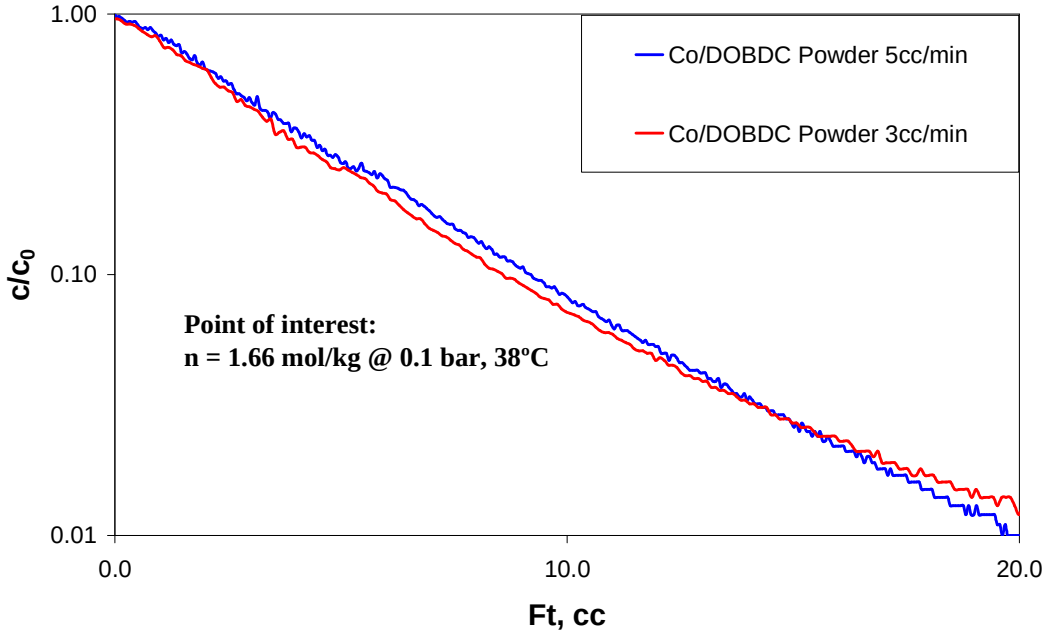

Figure 5.11 Experimental Ft plot of Co/DOBDC powder at 0.1bar of CO_2 in Helium, 38 °C, 3 and 5 cc/min.

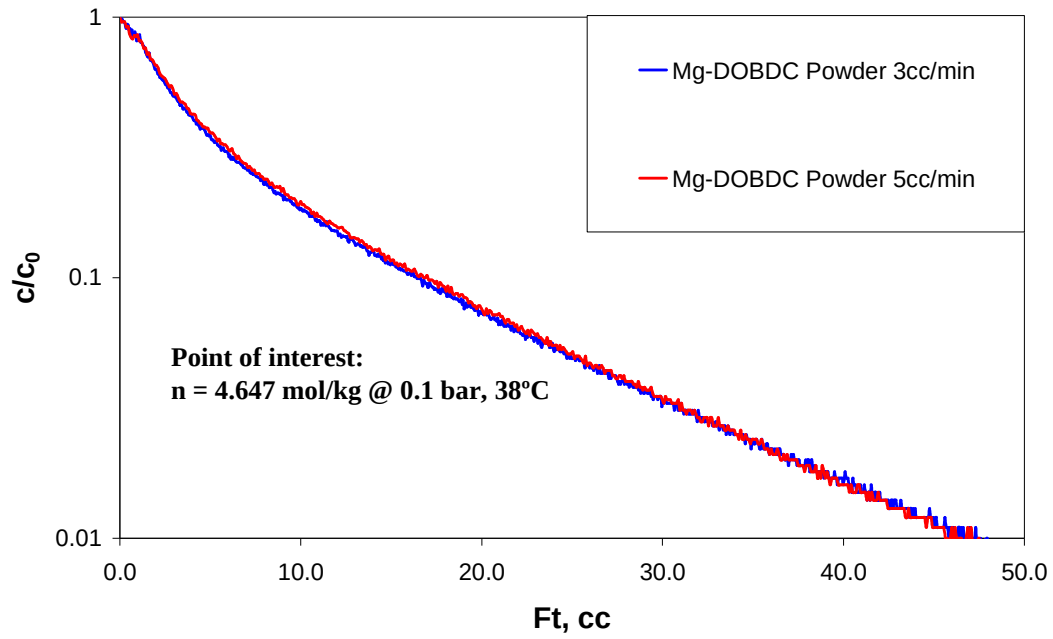

Figure 5.12 Experimental Ft plot of Mg/DOBDC powder at 0.1bar of CO_2 in Helium, 38 °C, 3 and 5 cc/min.

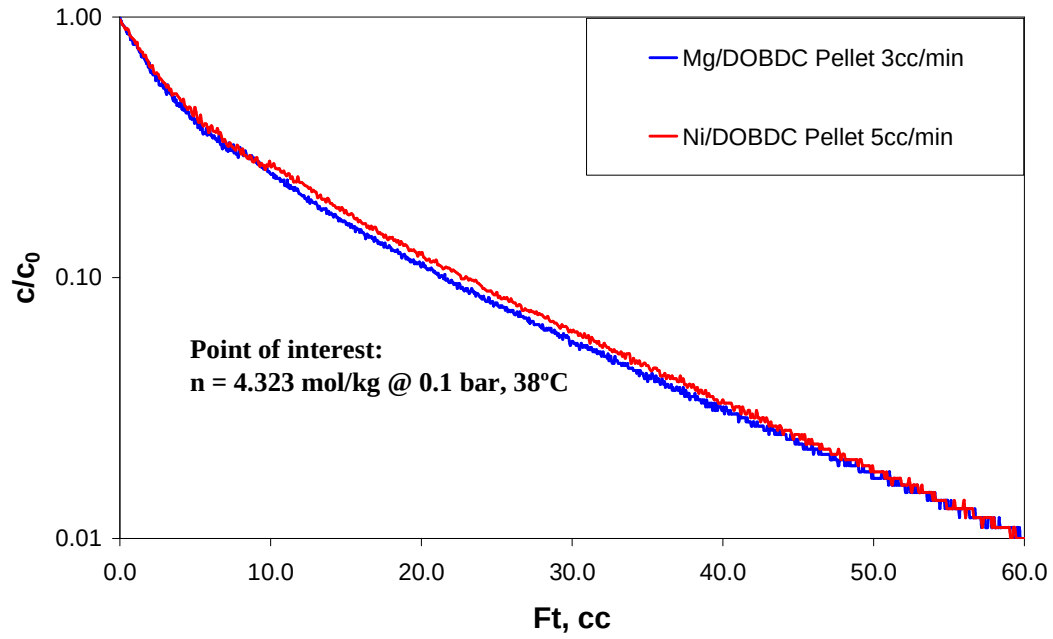

Figure 5.13 Experimental Ft plot of Mg/DOBDC pellet at 0.1bar of CO_2 in Helium, 38 °C, 3 and 5 cc/min.

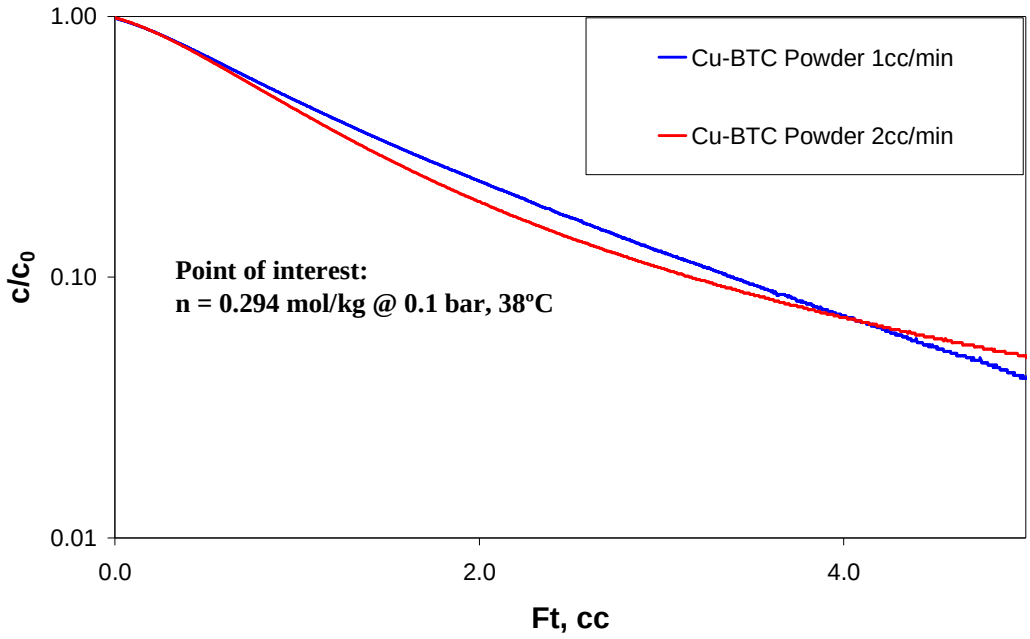

Figure 5.14 Experimental Ft plot of Cu-BTC powder at 0.1bar of CO_2 in Helium, 38°C, 1 and 2 cc/min.

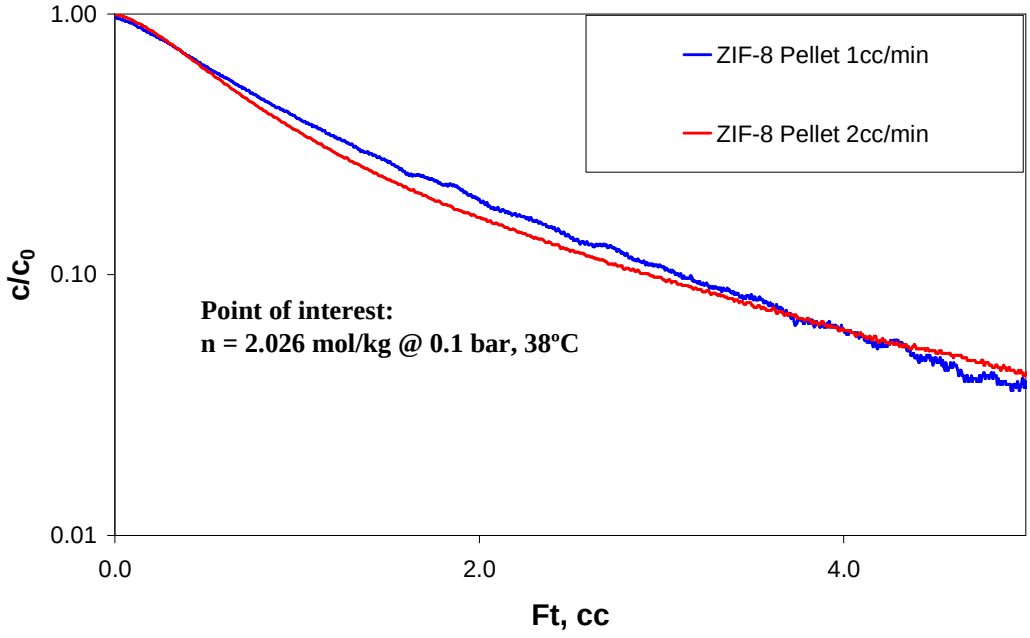

Figure 5.15 Experimental Ft plot of ZIF-8 pellet at 0.1bar of CO_2 in Helium, 38 °C, 1 and 2 cc/min.

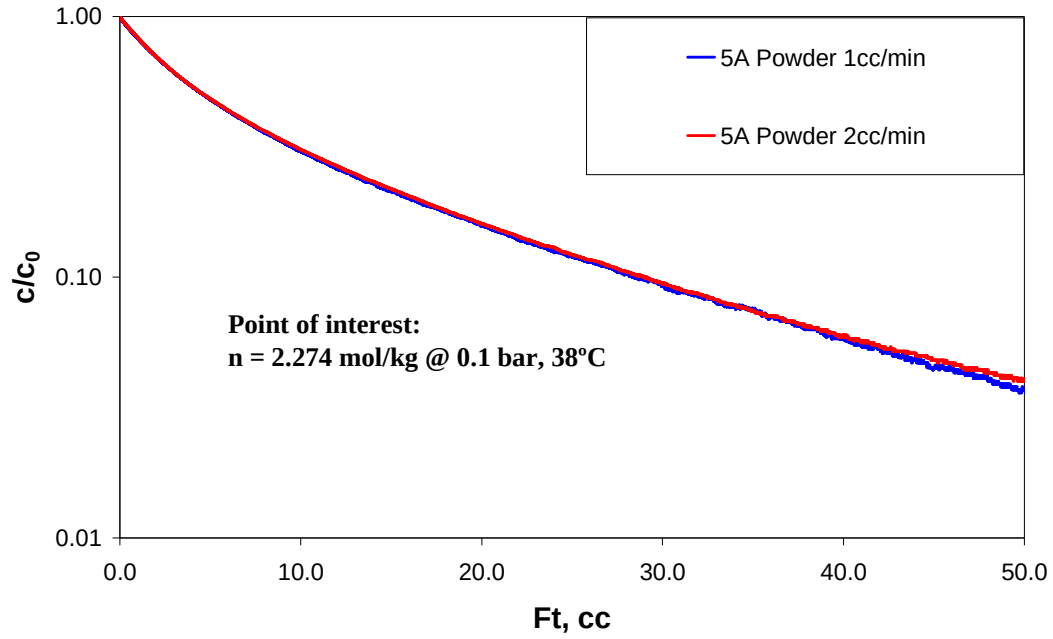

Figure 5.16 Experimental Ft plot of 5A powder at 0.1bar of CO_2 in Helium, 38 °C, 1 and 2 cc/min.

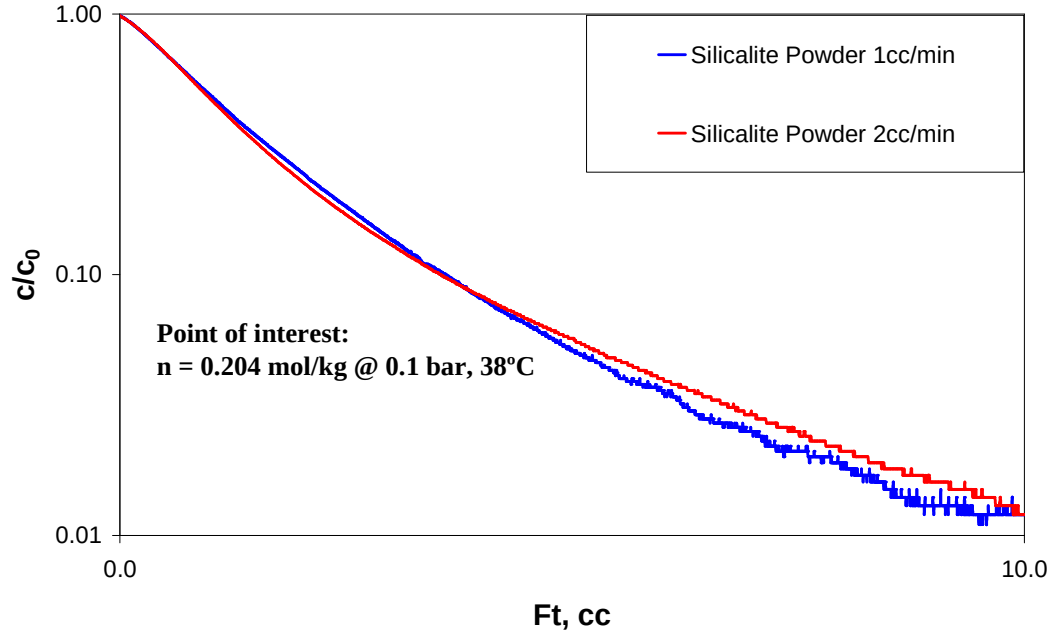

Figure 5.17 Experimental Ft plot of silicalite powder at 0.1bar of CO_2 in Helium, 38 °C, 1 and 2 cc/min.

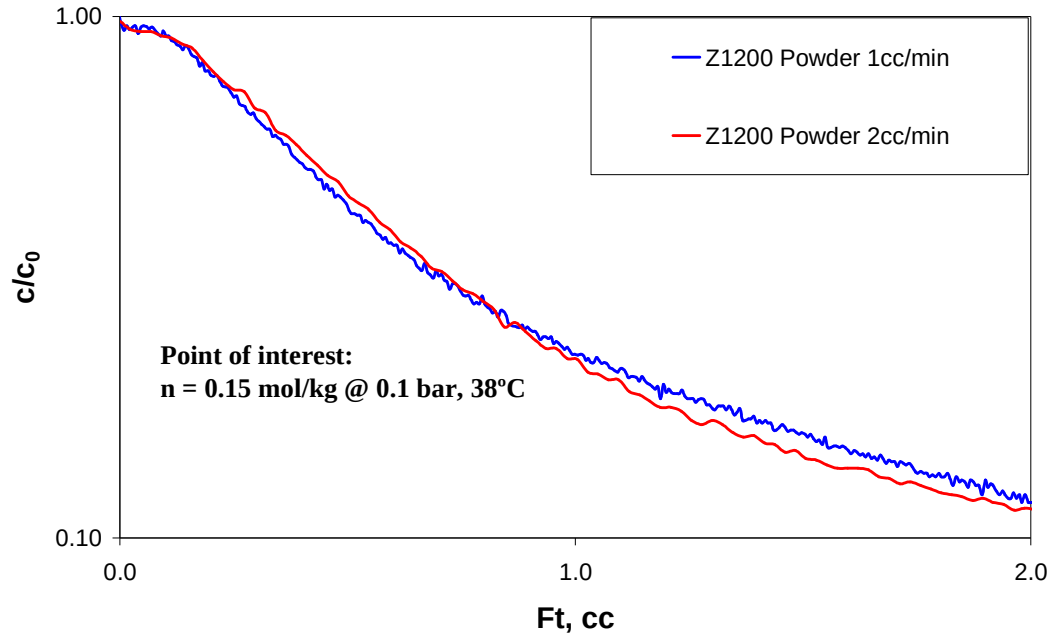

Figure 5.18 Experimental Ft plot of Z1200 powder at 0.1bar of CO_2 in Helium, 38 °C, 1 and 2 cc/min.

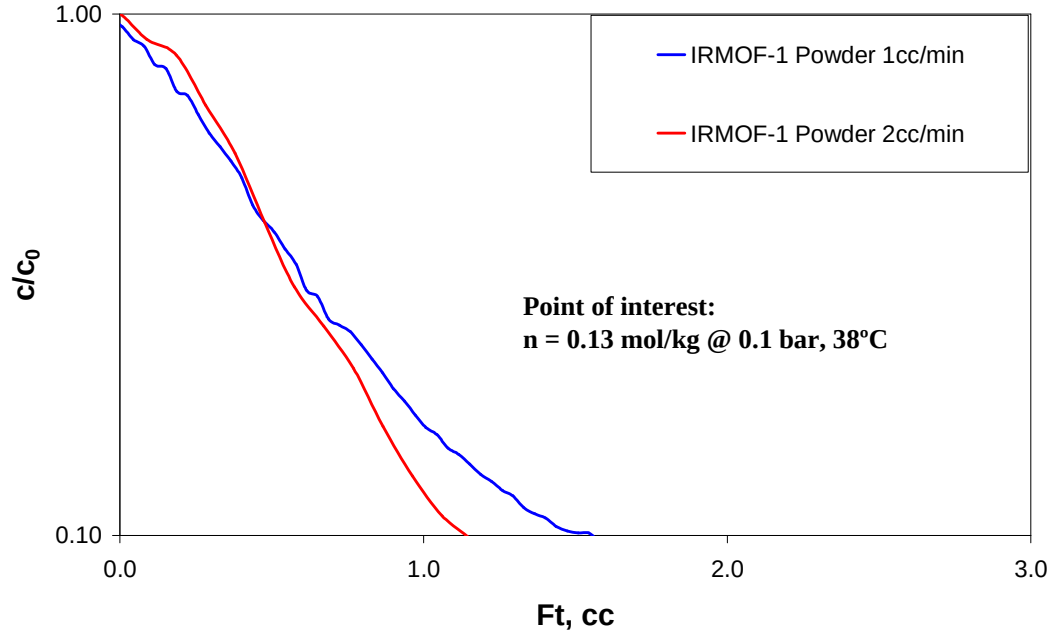

Figure 5.19 Experimental Ft plot of IRMOF-1 powder at 0.1bar of CO_2 in Helium, 38 °C, 1 and 2 cc/min.

Figure 5.20 presents the ZLC ranking of CO_2 desorption curves at 0.1 bar and 38°C for the all MOFs and three typical commercial zeolites. For the reason of qualitatively comparing capacity of different samples, the plot was normalized by the mass of the sample tested. Therefore, the areas under the desorption curves is directly proportional to the CO_2 adsorbent capacity. It is clear to ranking the adsorbents in this way as the right side the curve represents the higher capacity. The ZIF-8 pellets show a very low adsorption capacity of CO_2 at low CO_2 partial pressure range, even if it has pretty good thermal resistance as reported it is not a good candidate for carbon capture. By simply looking at the graph it is possible to rank the materials as follows: Mg/DOBDC > Ni/DOBDC > 13X > 5A> Co/DOBDC> Cu/BTC > Silicalite > Z1200 > IRMOF-1 > ZIF-8. Zeolites 13 X and 5A show a strong nonlinearity of the isotherm.

A good candidate adsorbent for carbon capture should not only have a high CO_2 capacity, but also have a linear desorption response. For instance, zeolite 13X has comparable adsorption capacity with Ni/DOBDC, but it has a lot of capacity at the low pressure range, which means that in PSA cycle, 13X requires more energy in the vacuum cycle than Ni/DOBDC. The M/DOBDC and Cu/BTC MOFs contain unsaturated metal sites, which can interact with adsorbate molecules to increase CO_2 adsorption capacity, but the M/DOBDC (where M = Mg, Ni, or Co and DOBDC = dioxybenzenedicarboxylate) MOFs have higher CO_2 adsorption capacity than Cu/BTC. This can be explained by higher density of open metal sites (either per unit of surface area or per unit of free volume of material) [75].

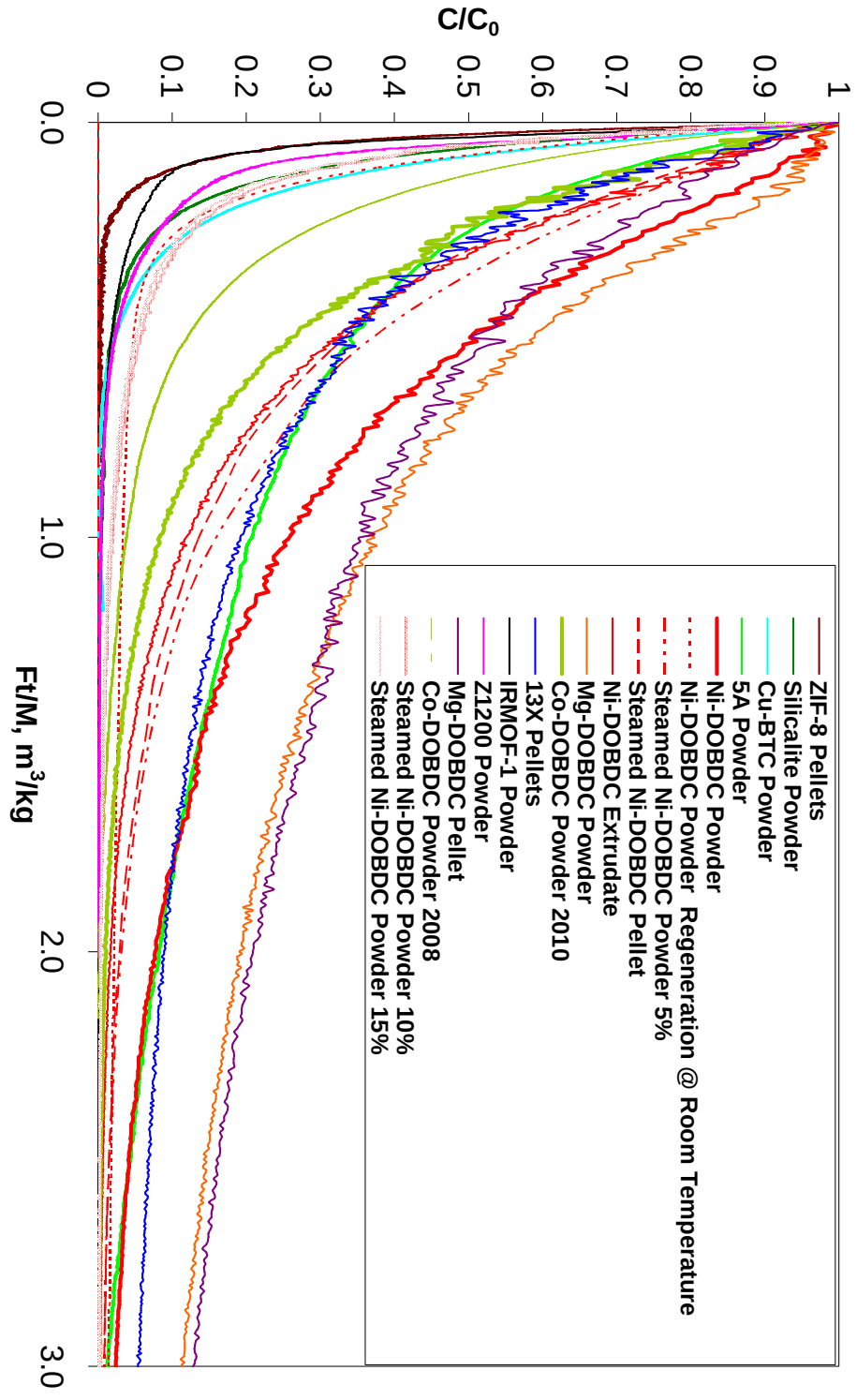

Figure 5.20 Ranking of all adsorbents at the point of interest for flue gas application (38 °C, 0.1 bar CO_2 partial pressure)

Compared to other two M/DOBDC adsorbent, the higher CO_2 adsorption capacity of Mg\DOBDC performs particularly well. It is known that MgO exothermically chemisorbs CO_2 to form $MgCO_3$ but CO_2 is not chemisorbed by the Mg−O bonds in Mg/DOBDC because of the rigid nature of the framework that prevents insertion into the Mg−O bonds. However, the ionic character of this bond promotes higher CO_2 uptake [49]. In M\DOBDC MOFs, CO_2 adsorption capacity increases with decreasing M−O bond length in the framework. The order of these bond lengths, which may be considered as an indication of the affinity of metals in this coordination state toward oxygen, is Mg−O (1.969 Å) < Ni−O (2.003 Å) < Co−O (2.031 Å) [75].

To obtain a quantitative comparison we need to apply Eq. (3.19) and get integrated and the desorption curves can be normalised by plotting the concentration vs Ft/V_S or using the mass, i.e. Ft/M, For weakly adsorbed species the required correction for dead volume from blank response but for strong adsorbed species, the dead volume is negligible. Figure 5.21 shows the ranking value of adsorbents by ZLC measurement of CO_2 at 0.1 bar. There is a very good agreement between the ZLC and gravimetric system [51]. So trends are predicted correctly, the CO_2 uptake is quite close especially for M/DOBDC MOFs. Identifying the best candidates is the most important task in screening, and the results are quite successful by the ZLC developed in this study. Once top candidates are identified, they can be studied in more detail experimentally. Given this validation, the ZLC technique could be used

for ranking the entire novel materials, providing insights and suggesting the most promising materials for industrial applications.

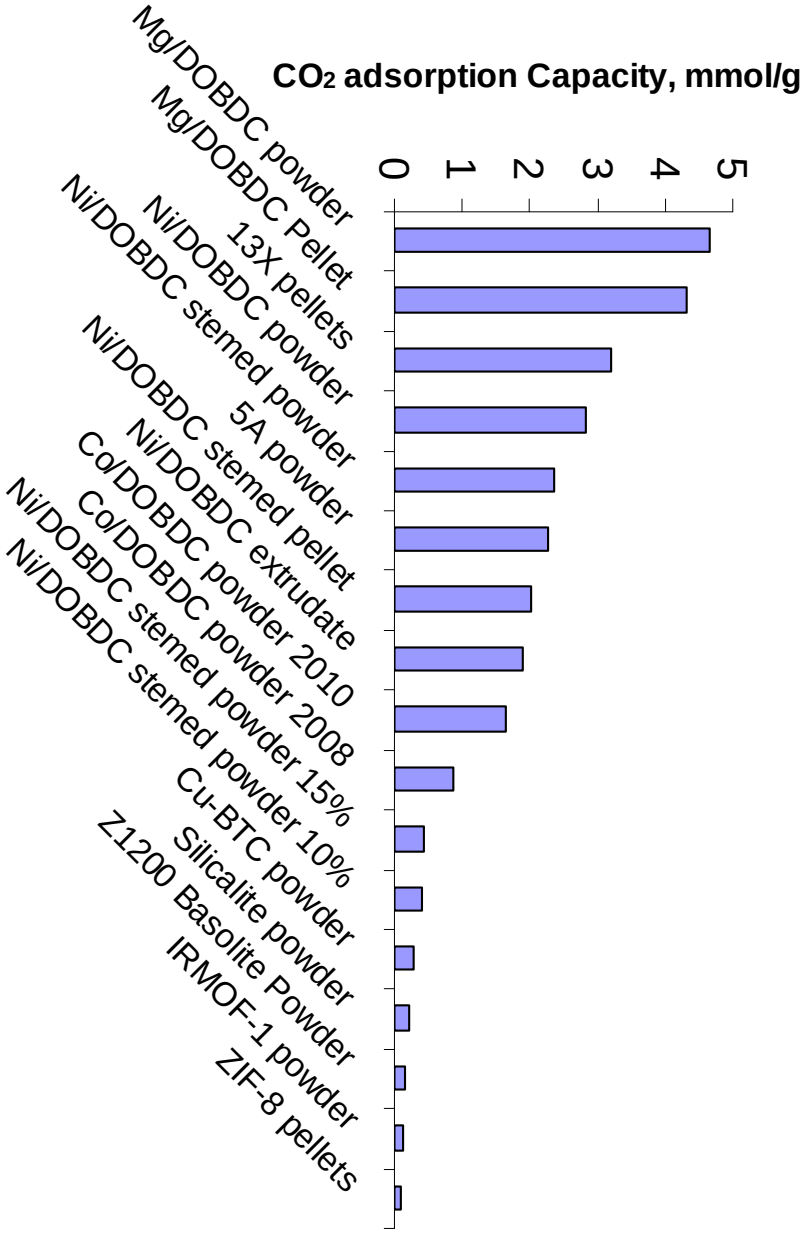

Figure 5.21 Experimental CO_2 capacity calculated from ZLC at 0.1 bar. Data obtained at 38 °C.

5.4.2 Heat of adsorption at zero loading on typical adsorbents

The ZLC desorption curve starting at the initial equilibration point and ending at the zero loading point, therefore it is a simple and effective way to study and calculate the temperature dependence of Henry law constant by looking at the zero loading region. Since Mg/DOBDC and Ni/DOBDC MOFs significantly outperform all other MOFs and benchmark zeolites at the point of interest in low pressure, the ZLC measurements were applied at different temperatures. This was also done for zeolite 13X. Experiments at 65 °C, 50 °C and 38 °C are shown in Figures 5.22, 5.23 and 5.24. The Ft plots include all the temperature response and blanks for Mg/DOBDC, Ni/DOBDC and 13X respectively, the temperature dependence of CO_2 adsorption capacity can be determined.

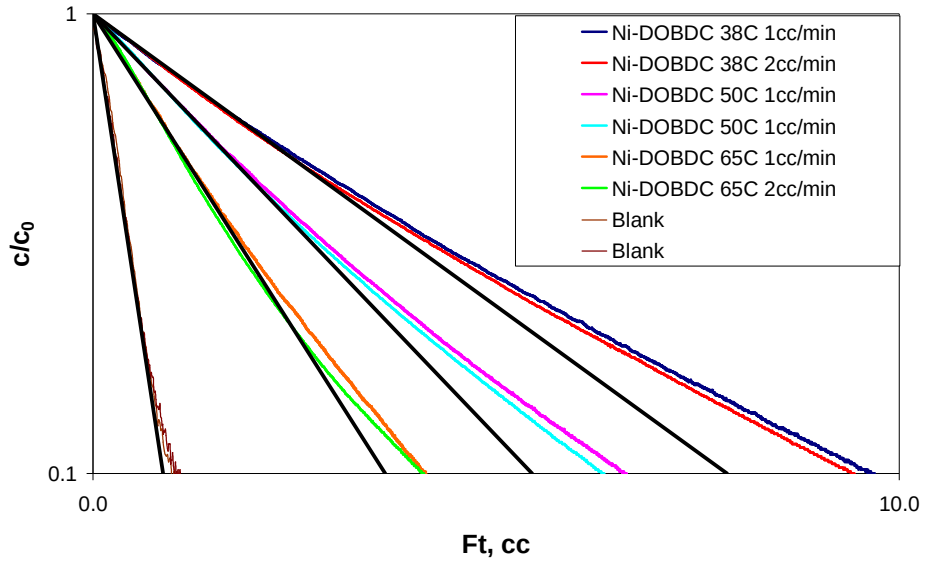

Figure 5.22 Experimental Ft plot with linear asymptotes (Henry's Law region) of Ni/DOBDC powder at 0.1bar of CO_2 in Helium, 38 °C, 50 °C and 65 °C, 1 and 2 cc/min and blanks

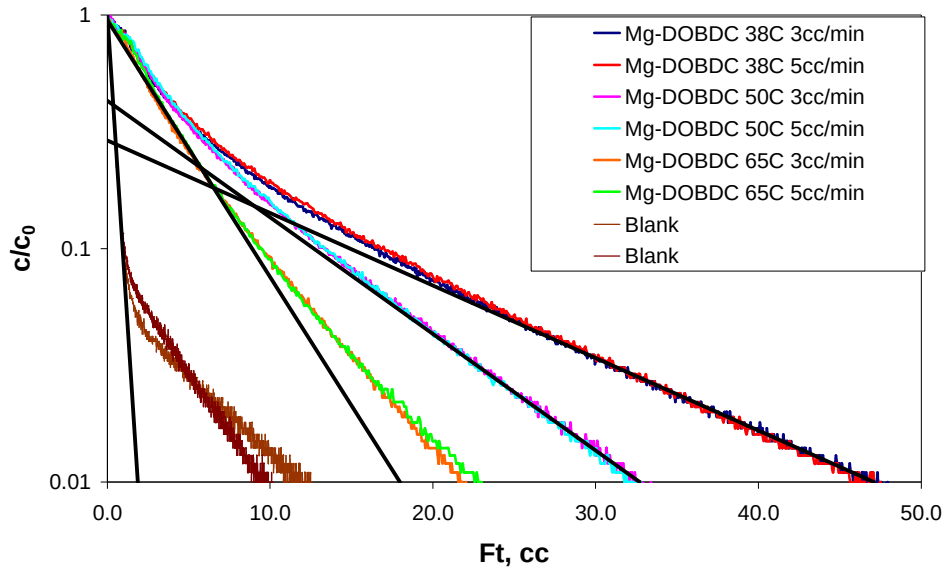

Figure 5.23 Experimental Ft plot with linear asymptotes (Henry's Law region) of Mg/DOBDC powder at 0.1bar of CO_2 in Helium, 38 °C, 50 °C and 65 °C, 1 and 2 cc/min and blanks

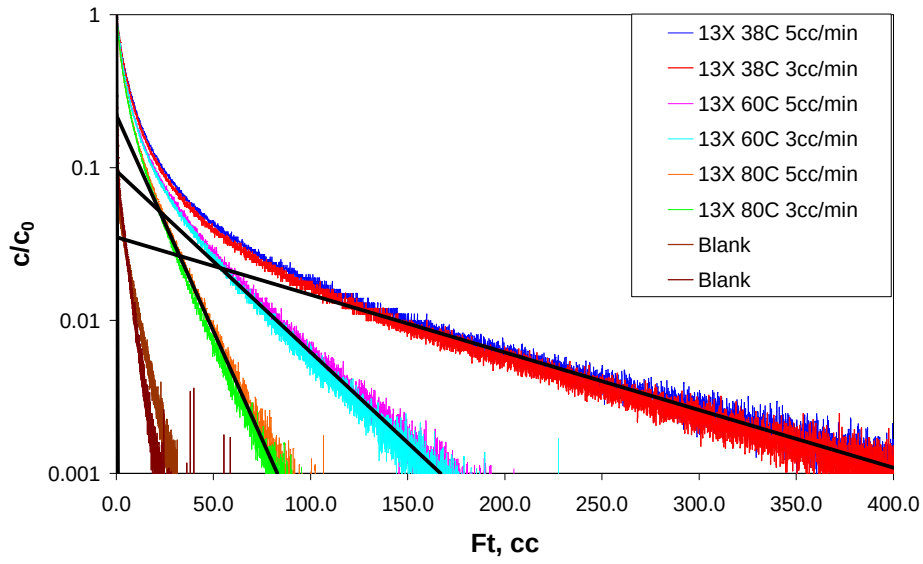

Figure 5.24 Experimental Ft plot with linear asymptotes (Henry's Law region) of 13X pellets at 0.1bar of CO_2 in Helium, 38 °C, 60 °C and 80 °C, 3 and 5 cc/min and blanks

The heat of adsorption was found to be 44kJ/mol, 38kJ/mol and 37kJ/mol for Mg/DOBDC, Ni/DOBDC and 13X respectively. The CO_2 capacity at the POI for Mg/DOBDC powder was larger than Ni/DOBDC, the stronger interactions between the CO_2 molecules and the unsaturated metal centres (UMCs) is consistent with the larger isosteric heat of adsorption. The estimation of isosteric heat of adsorption on 13X by ZLC was similar with 37.2 kJ/mol by Cavenati and Rodrigues [67] and slightly higher than 34.3 kJ/mol by Rege and Yang [12].

5.4.3 Ni/DOBDC MOFs ranking after modification

Figure 5.25 shows the qualitative comparison of the CO_2 adsorption capacity for the different Ni-DOBDC samples.

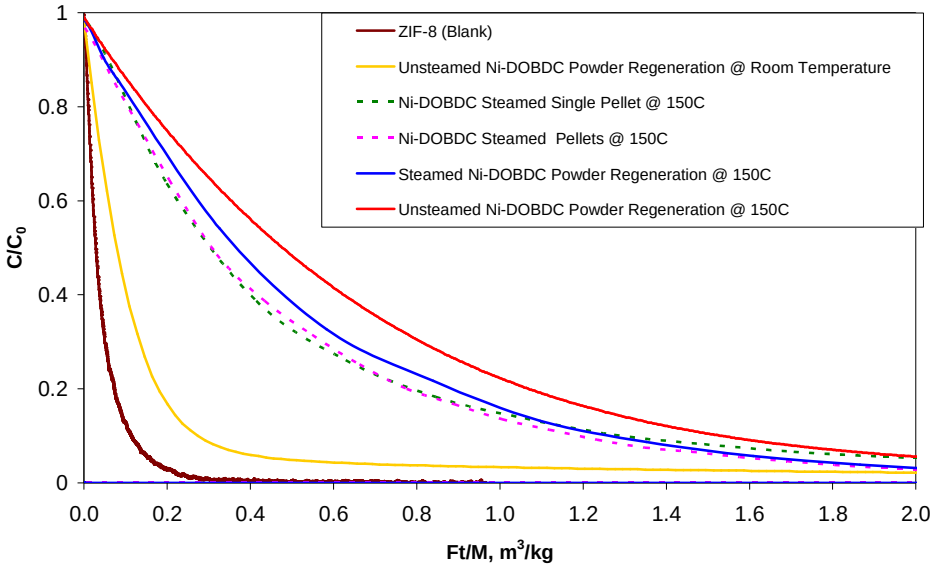

Figure 5.25 Comparison of different Ni-DOBDC samples (38 °C, 0.1 bar CO_2 partial pressure).

Figure 5.26 shows the corrected plot that we used to compare quantitatively the unsteamed, steamed and steamed pellet samples and evaluate the loss in capacity. Figure 5.27 shows the simple Ft analysis.

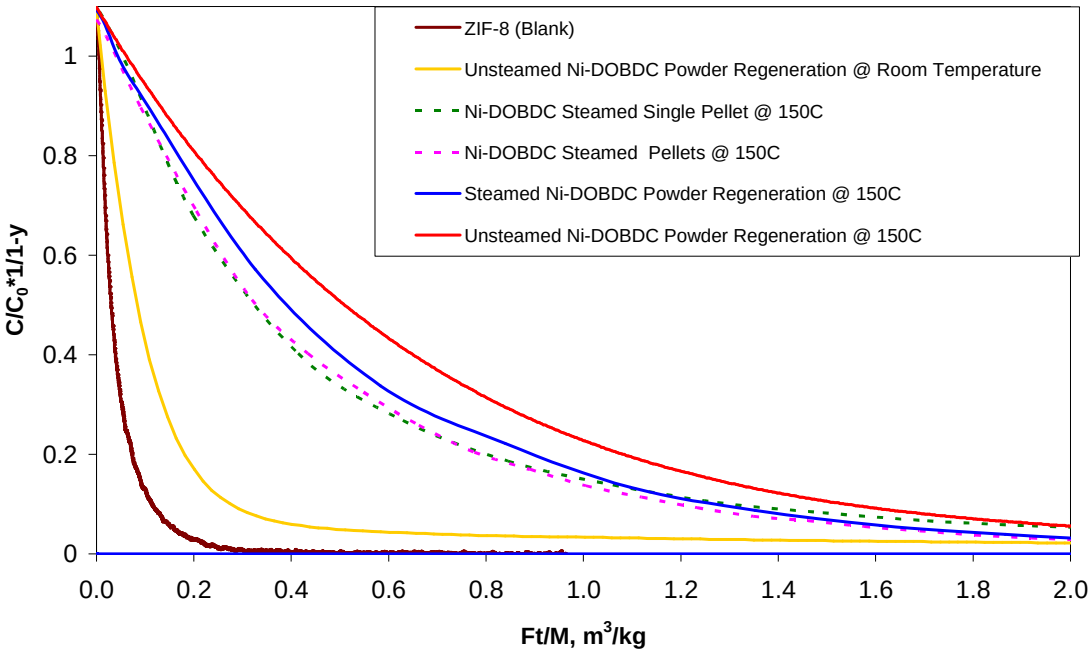

Figure 5.26 Comparison of different Ni-DOBDC samples, with flowrate correction (38 °C, 0.1 bar CO_2 partial pressure).

Table 5.3 includes the comparison of the different samples (relative to the unsteamed powder) used in the three methods of analysis. While the integral from Figure. 5.26 is the most accurate, the direct plot shown in Figure 5.27 yield very similar results (within 1%) which are acceptable for relative comparisons. Steaming has a mild negative effect on the CO_2 adsorption capacity for Ni-DOBDC. Based on the net analysis, it can be concluded that steaming reduces capacity by approximately 16.0%,

and pelletizing introduces an additional 10.7% loss. The simple Ft analysis yields similar results, except for the lowest capacity (room temperature regeneration). From Ft slope plot slope analysis, the steaming effect is approximately 16.2%, and the additional pelletizing effect is 11.8%. But the results show that regeneration at room temperature and atmospheric pressure did not desorb all the water, therefore, in the capture plant, thermal regeneration is required for Ni/DOBDC. This method yields reasonable values when the desorption curve is very different from the blank and can be used as a way of estimating the dimensionless Henry's law constant to be used in the pellet.

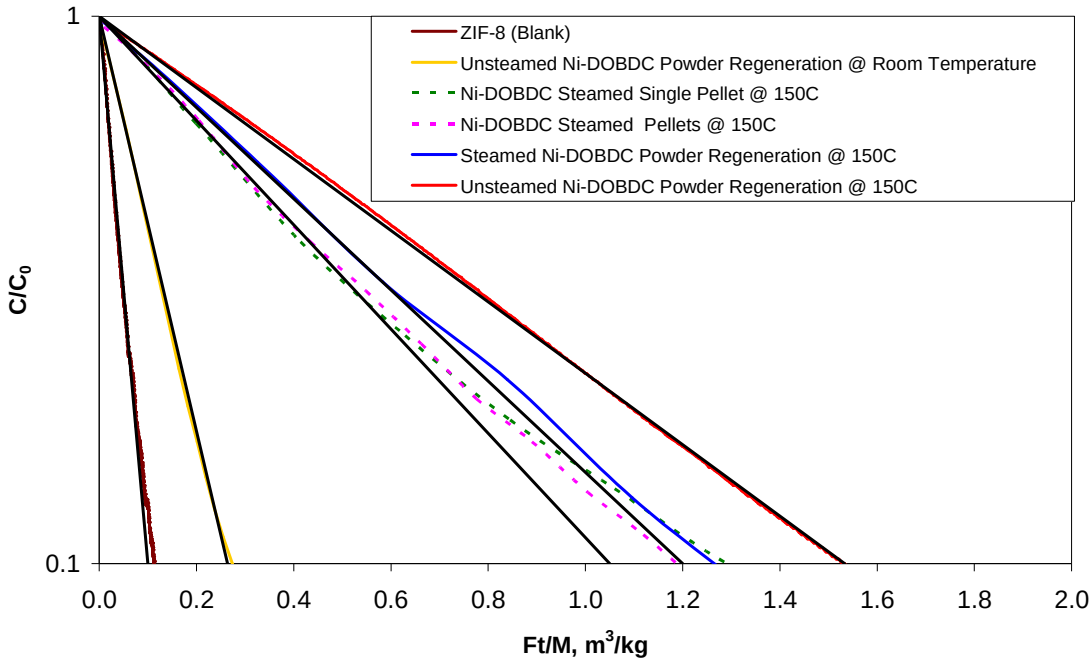

Figure 5.27 Ft plots with linear asymptotes (38 °C, 0.1 bar CO_2 partial pressure)

Table 5.3 Relative CO_2 capacities comparison with Ni/DOBDC sample (38 °C, 0.1 bar CO_2 partial pressure).

.

Analysis Method	**Unsteamed Powder (150ºC)**	**Unsteamed Powder (ambient T)**	**Steamed Powder (150ºC)**	**Steamed Pellets (150ºC)**
Integral from Fig. 4.9	100%	20.1%	84%	73.3%
Integral from Fig. 4.10	100%	19.5%	83.3%	72.4%
Ft Slope from Fig. 4.11	100%	12.6%	83.8%	72.0%

A new batch of Ni/DOBDC powder was supplied by UOP. Figure 5.28 presents the comparison of different Ni-DOBDC samples, with flowrate correction (38 °C, 0.1 bar CO_2 partial pressure), and Table 5.4 compares the value for each sample. The ZLC experiment shows a lower CO_2 capacity than that of the previous batch and the steaming caused about 60 % decrease in CO_2 capacity for this powder. The stability obtained by exposing the Ni/DOBDC sample to up to 15 mol% steam at 150 ºC for four hours, left about 40% capacity. Note that in the actual application, the MOF adsorbent will never be exposed to such harsh steaming. Nevertheless, the material was not completely destroyed by the extreme steaming conditions. This suggests that MOFs still hold great promise in this application provided they are protected from moisture.

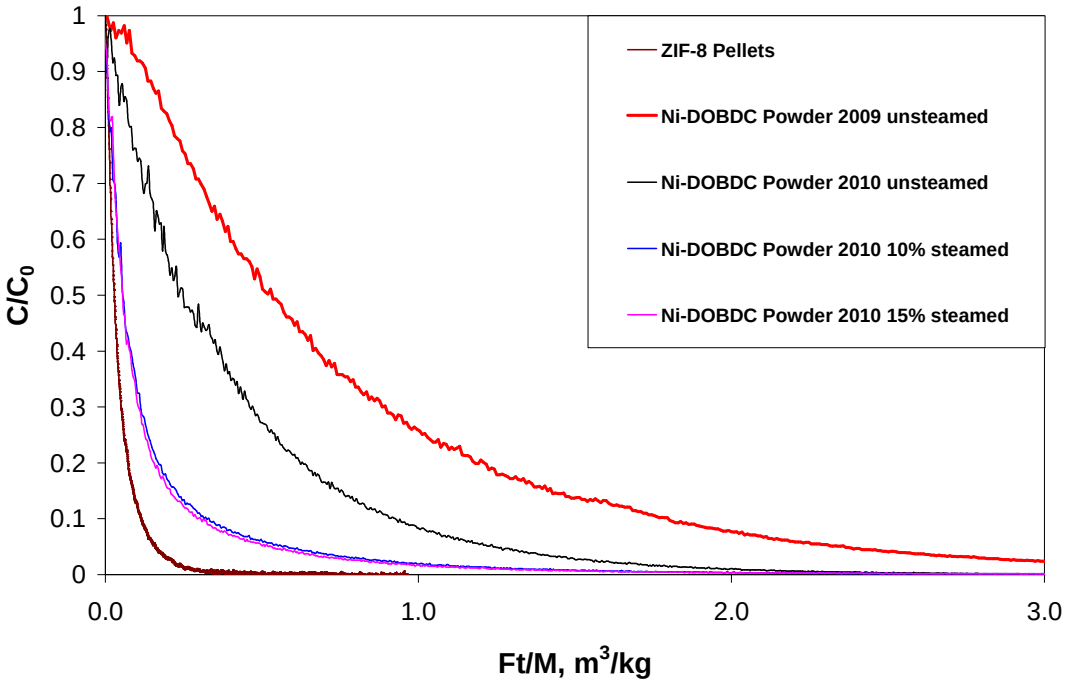

Figure 5.28 Comparison of different Ni-DOBDC samples, with flowrate correction (38 °C, 0.1 bar CO_2 partial pressure).

Table 5.4 Relative capacities

Adsorbents	**Ni/DOBDC 09 unsteamed**	**Ni/DOBDC 10 unsteamed**	**Ni/DOBDC 10 10% steamed**	**Ni/DOBDC 10 15% steamed**
Batch code	33279-28-1x	33735-5	33735-5	33735-5
CO_2 Capacity @ 0.1bar (mol/kg)	2.84	1.72	0.41	0.44

5.5 Conclusions

The semi-automated ZLC technique developed in this study was applied to provide rapid ranking of novel adsorbent materials for carbon capture. At the point of interest

for flue gas application (38 °C, 0.1 bar CO_2 partial pressure), Mg/DOBDC was found to outperform significantly all other MOFs and benchmark zeolites in low pressure physisorption of CO_2. Due to its comparable capacity with amine solusions, it may have a promising future for capturing CO_2 from flue gases. The CO_2 capacity at the POI for Mg/DOBDC powder was larger than that of Ni/DOBDC, the stronger interactions between the CO_2 molecules and the UMCs is consistent with the larger isosteric heat of adsorption.

CHAPTER 6

6. STUDY OF DIFFUSION BEHAVIOURS OF CO_2 IN NOVEL ADSORBENTS

6.1 Introduction

In the capacity-ranking experiments, DOBDC MOFs offers high capacity even at low CO_2 partial pressure. This gives them the potential to capture CO_2 from flue gas. Besides equilibrium studies, it is also important to measure mass transfer kinetics of CO_2 adsorption in MOF materials to be able to design adsorption separation processes. However, experimental research work on the diffusion of gases, including CO_2 in MOFs, is quite limited in the literature. Zhao [76] measured the diffusion coefficient of CO_2 in MOF-5 (cage with cavity of 12 Å and aperture opening of 8 Å)

to be in the range of 8.1−11.5 × 10^{-5} m^2/s in 295−331K with an activation energy of 7.61 kJ/mol. Further research was focused on theoretical and simulation work [77, 78], therefore, it is quite important to develop a system for measuring the kinetics of novel adsorbents for carbon capture.

In this chapter, the new semi-automated ZLC technique has been applied to investigate the diffusion behaviour of CO_2 in various samples of adsorbents, which have potential use in carbon capture due to the very high CO_2 adsorption capacity at the point of interest. For equilibrium measurements the L value in eq. 2.7 need to be small, ideally less than 1, the experiment conditions has to be small particles, large amounts of solid and low flowrates. However, for kinetic experiments, the L value should greater than 5 in order to have an accurate measurement of the diffusivity. In this case we want to increase the flowrate, use large crystals and decrease the amount of solid in the ZLC column.

6.2 Co/DOBDC Powder

The Co/DOBDC adsorbent has the largest crystals that were synthesised and supplied by UOP. The SEM image is shown in Figure 6.1.

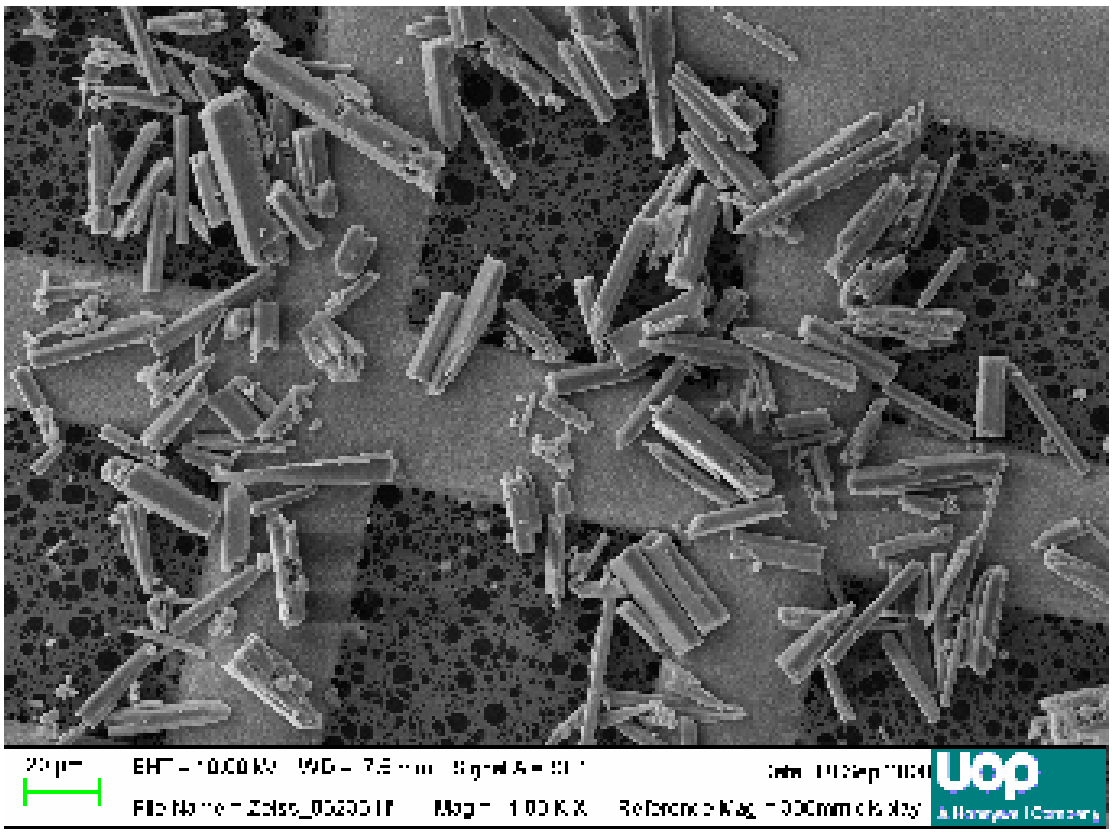

Figure 6.1 SEM image of Co/DOBDC crystals.

The dimensions of the crystals were measured using the image analysis tool GIMP 176 crystals, While the crystals considered are more similar to 3D bodies with square or rectangular faces, for mass transfer purposes the kinetics can be approximated by the behaviour of spheres that have the same surface to volume ratio = $3/R_c$ (Twigg 1989). The crystals dimensions are converted to an equivalent radius and using size interval of 1 µm, the log normal distribution (PSD) (lognormal distribution of the numbers of crystals in each size interval) is examined to determine the mean crystal diameter. In Figure 6.2 a log normal of distribution curve is plotted. From the log normal probability curve, the mean diameter was found to be approximately 6.5 µm.

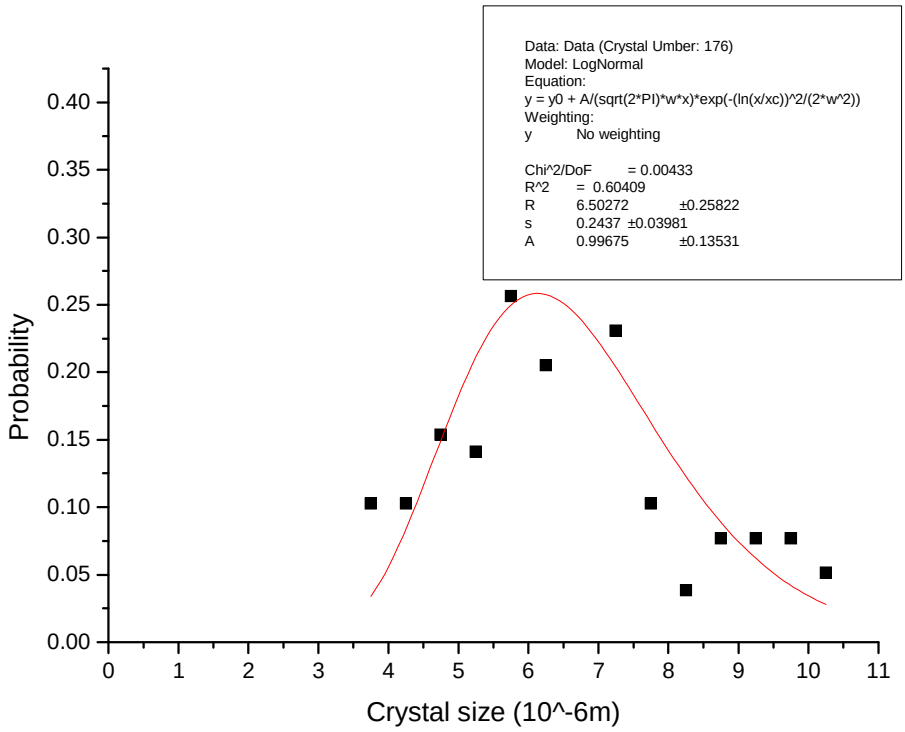

Figure 6.2 Size distribution of Co/DOBDC crystals.

3 mg of Co/DOBDC powder was packed between two porous stainless steel sinter discs held in one end of a Swagelok 1/8 in. union. Prior to the experiment, the sample was regenerated with a ramping rate of 1°C/min to 125°C and then held at this temperature for 12h at 1 cc/min of helium purge, After regeneration, the oven temperature was reduced to 38°C and the flow system switched to the high flowrate mass flow controllers. During an experiment, the sample was first equilibrated with helium stream containing 10% of CO_2 which prepared in the dosing volume. At time zero, the flow was switched to a pure helium purge stream at the same flow rate. The sorbate concentration at the outlet of the ZLC can be conveniently followed using a mass spectrometer (MS). ZLC experiments were carried out at two different flow rates (at 30 and 45 cc/min) in order to establish kinetic or equilibrium control.

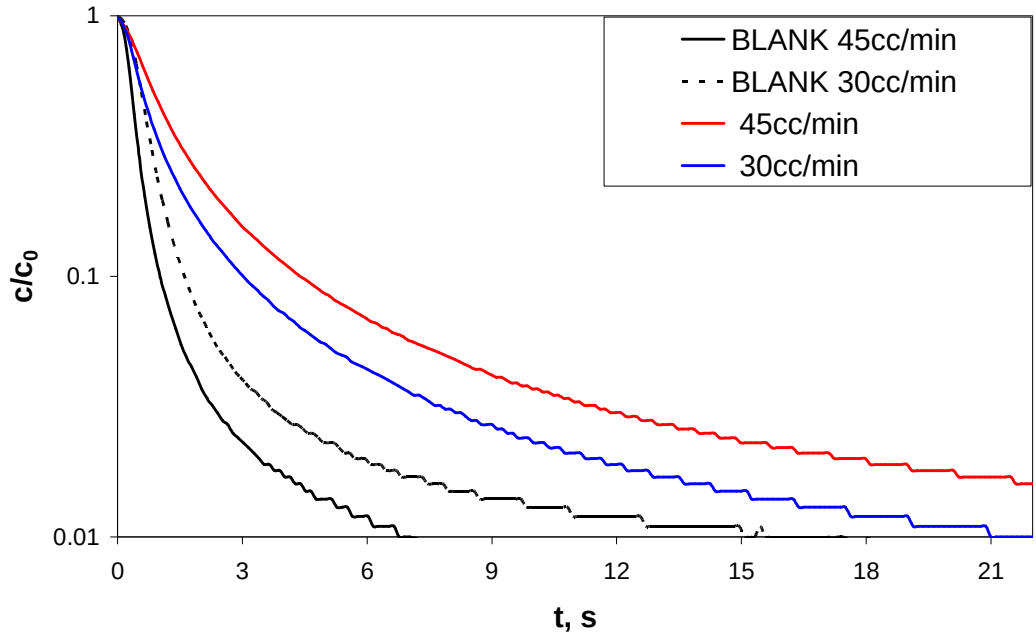

\Figure 6.3 ZLC curves for Co/DOBDC at 30 and 45 cc/min at 38 °C.

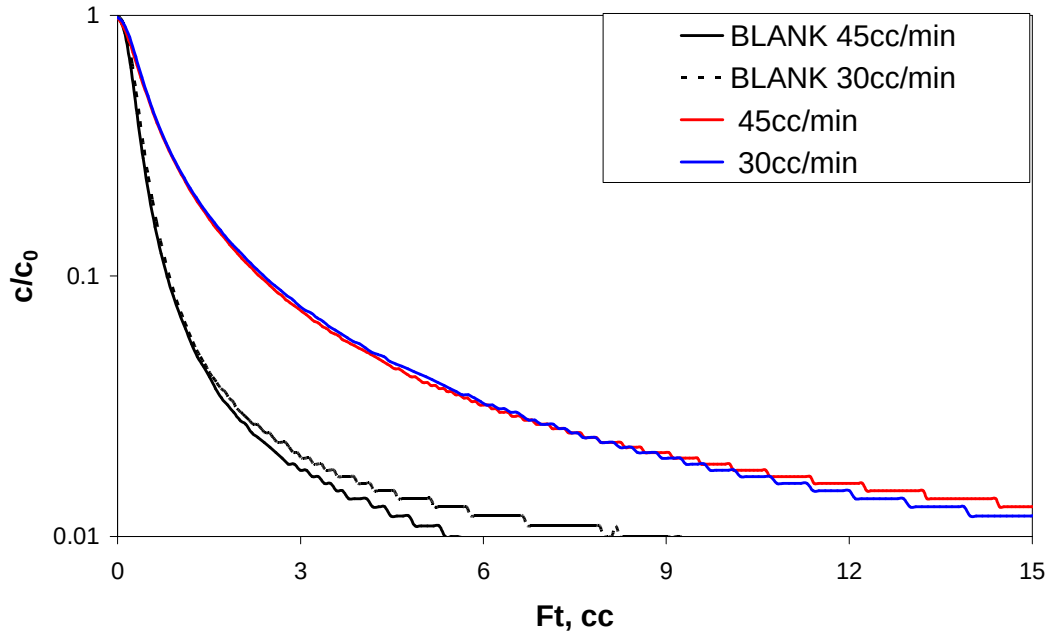

Figure 6.4 ZLC curves for Co/DOBDC at 30 and 45 cc/min at 38 °C.

For an accurate interpretation of ZLC data, it is essential to check whether the overall kinetics of desorption, as measured by the ZLC, is controlled by kinetics or by the equilibrium. One way of checking this condition is by plotting ln (c/c_o) vs. Ft. For

equilibrium-controlled processes, the response curves should be independent of desorption volume, implying an overlap of curves for varying Ft, whereas it diverges for a kinetically controlled process. The ZLC desorption curve and the experimental Ft plots for Co/DODBDC crystal are shown in Figures 6.3 and 6.4 (10% CO_2 in Helium, 38ºC, Flowrate = 30 and 45 cc/min)

The results of the Ft plot indicate that the curves overlap, so the system is still close to equilibrium control even at the highest flow rate. For a CO_2 capture process, this is actually a positive result, since in an equilibrium-driven process mass transfer limitations reduce the separation efficiency of the material. Duncan and Moller [79] did a research with effect of size distribution in ZLC and stated that analyzing such a curve with the standard ZLC model causes the diffusional time constant to be underpredicted, whereas the adsorption related parameter (L) is overpredicted, and that the error increases with increasing distribution width. Since the system is still under equilibrium control, we can only estimate a lower bound on the diffusivity so that the L parameter in the experiment was less than 1, and base on the equation (3.9) $L = \frac{1}{3}\frac{F}{KV_s}\frac{R^2}{D}$, the diffusivity was greater than $2\text{x}10^{-12}$ m^2/s. To obtain more specific kinetics information, larger crystal size needed.

6.3 Ni/DOBDC compressed pellets

Figure 6.5 (a) shows the pressed Ni/DBODC pellet as received from UOP. Since the ZLC is packed in a 1/8” Swagelok union fitting, the original pellet could not be

tested directly. Fragments of different sizes were broken off the material as shown in Figure 6.5 (b), (c) and (d).

(a)

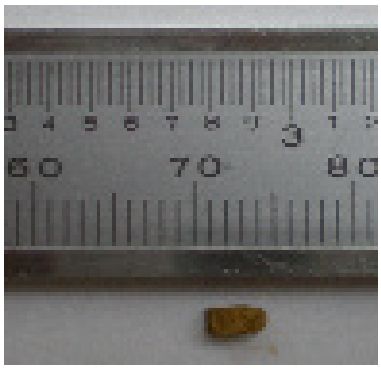

(b)

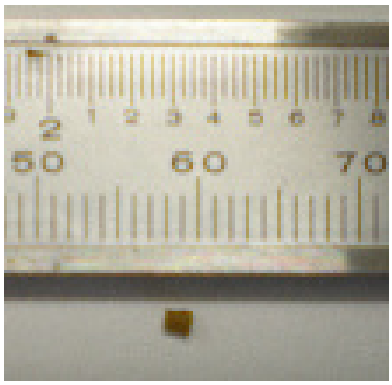

(c)

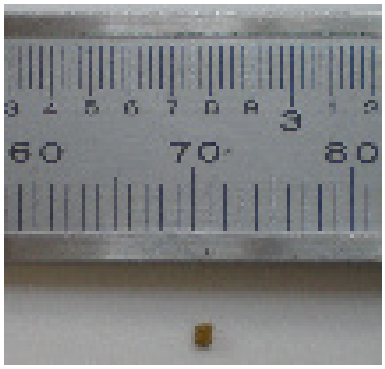

(d)

Figure 6.5 Formed pellet and fragments used in the kinetic experiments.

For mass transfer purpose the images were used to obtain the effect radius that gives the same surface to volume ratio. Table 5.1 includes the dimensions measured by image analysis tool (GIMP) of the individual pellets and the equivalent radius calculated on this basis.

Table 6.1 Dimensions measured by image analysis tool (GIMP) of the fragments and the calculated equivalent radius.

Fragments	**Mass of sample (mg)**	**Width (mm)**	**Length (mm)**	**Height (mm)**	**Surface Area (mm^2)**	**Volume (mm^3)**	**Equivalent Radius (mm)**
b	8.8	2.0	4.2	1.9	40.4	16.0	1.19
c	2.7	1.8	2.0	1.2	16.3	4.3	0.79
d	1.5	1.0	1.4	1.0	7.6	1.4	0.57

Three ZLCs were packed with 1 - 9 mg of Ni/DOBDC pellets. Prior to the experiment, the sample was thermally regenerated with a ramping rate of 1°C/min to 150°C and then held at this temperature for 12h and 1 cc/min of helium purge gas. After regeneration, the oven temperature is reduced to 38°C and the flow system switch to high flowrate mass flow controller. For each sample, ZLC runs at 5 different flow rates were performed in the range of 5 - 45 cc/min. If the system is under macropore diffusion control, the ratio of pore diffusivity with two different purge gases should be more or less the same as the ratio of the two molecular diffusivities. Therefore, to verify the validity of the assumption that the Ni/DOBDC pellet is under macropore diffusion control, the column was regenerated again and the same ZLC measurement procedures were used with N_2 as the purge gas.

Figure 6.6 shows the qualitative comparison of the CO_2 adsorption capacity for the different Ni-DOBDC fragment (R = 0.57 mm, R = 0.79 mm, R = 1.19 mm) at 0.1bar

of CO_2 in Helium, 38 °C, 5 cc/min and the blank response. This initial test was carried out to check if these fragments showed consistent adsorption capacities. It is quite clear that there is very little variation between the three compressed fragments.

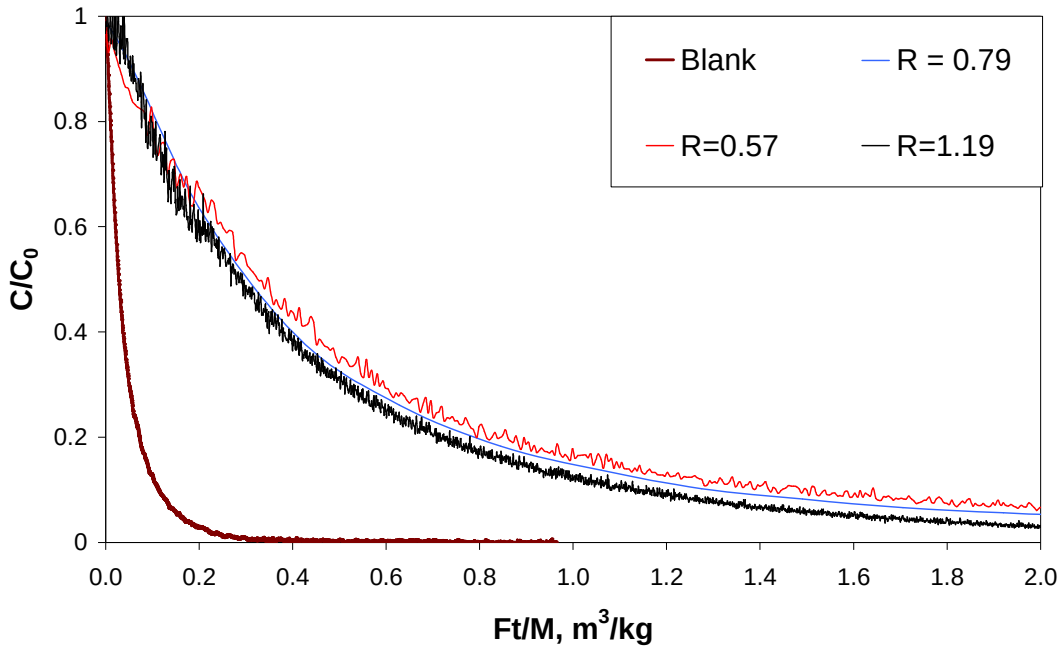

Figure 6.6 Comparison of adsorbent capacity of different Ni/DOBDC fragments. (R = 0.57 mm, R = 0.79 mm, R = 1.19 mm) at 0.1bar of CO_2 in Helium, 38 °C, 5 cc/min and the blank response.

The experimental Ft plots for each Ni/DOBDC pellets of particle size 0.57mm, 0.79 mm and 1.19 mm are shown in Figures 6.7, 6.8 and 6.9 (10% CO_2 in Helium, 38ºC, Flowrate = 5,10, 20, 30 and 45 cc/min) respectively. For equilibrium-controlled processes, the response curves should be independent of desorption volume, implying an overlap of curves for varying *Ft*, whereas it diverges for kinetically controlled process. As shown in Figure 6.7, the representative response curves for the smallest pellets (R = 0.57 mm) at five different purge rates are clearly overlapping,

confirming that the process is close to equilibrium control because of low R value. The Ft plots from the other two pellets (R = 0.79 mm, R = 1.19 mm) clearly indicate that the desorption is kinetically controlled.

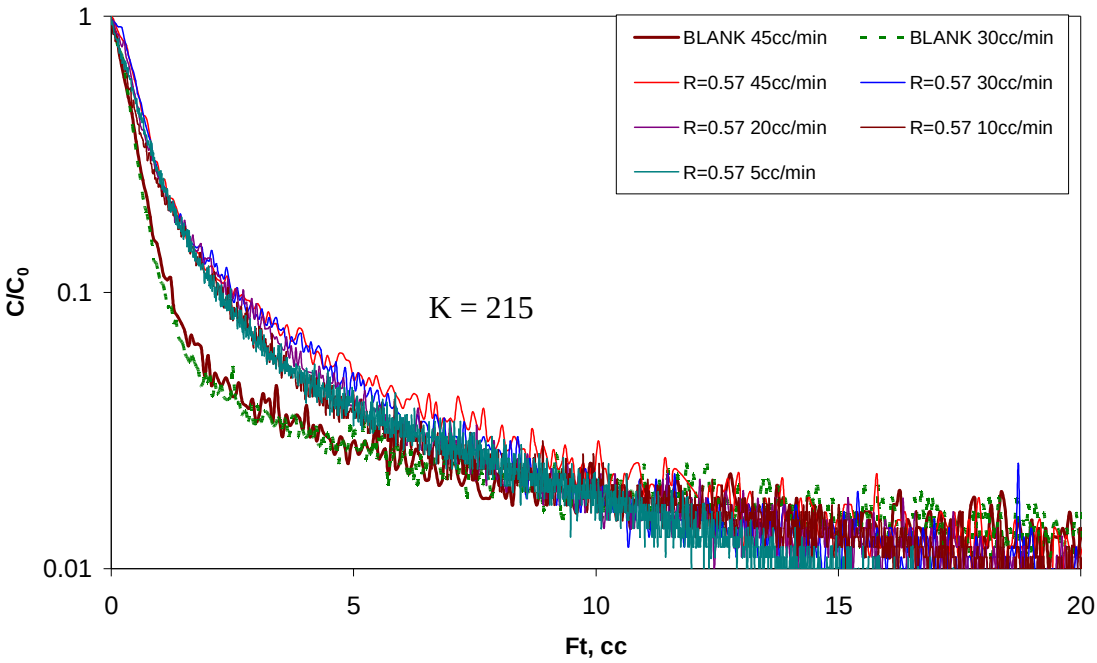

Figure 6.7 Experimental Ft plot of Ni/DOBDC pellet (R = 0.57 mm) at 0.1bar of CO_2 in Helium, 38 °C, 5, 10, 20, 30, 45 cc/min and the blank response at 30, 45 cc/min

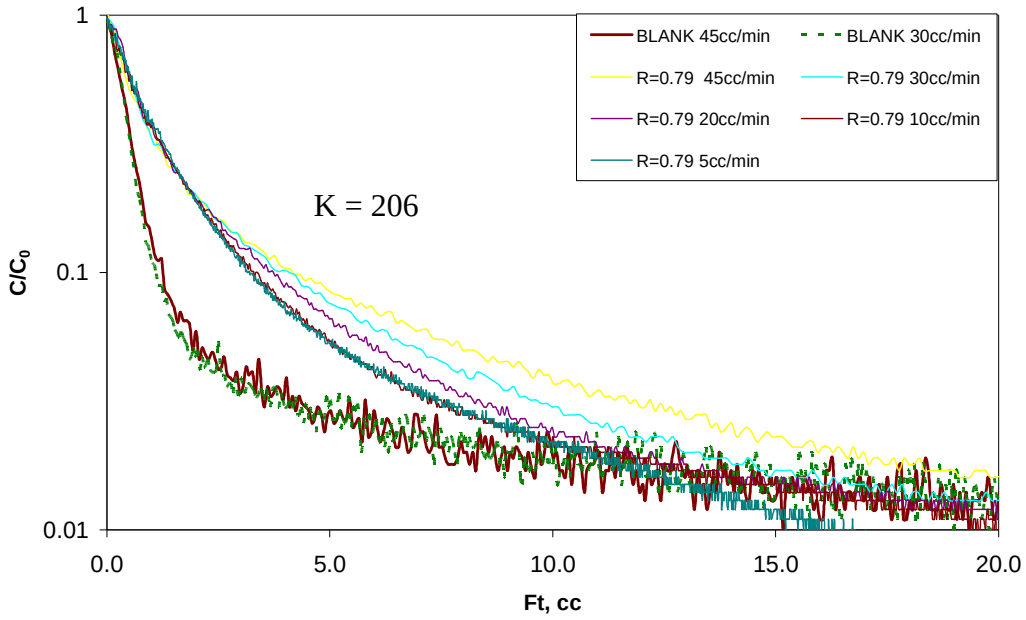

Figure 6.8 Experimental Ft plot of Ni/DOBDC pellet (R = 0.79 mm) at 0.1bar of CO_2 in Helium, 38 °C, 5, 10, 20, 30, 45 cc/min and the blank response at 30, 45 cc/min

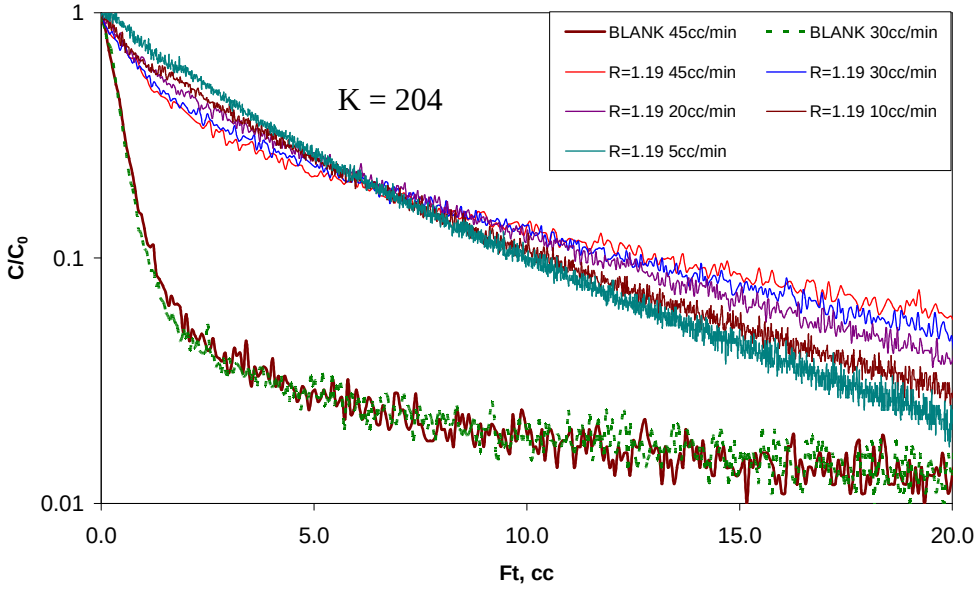

Figure 6.9 Experimental Ft plot of Ni/DOBDC pellet (R = 1.19 mm) at 0.1bar of CO_2 in Helium, 38 °C, 5, 10, 20, 30, 45 cc/min and the blank response at 30, 45 cc/min.

The ZLC desorption curve of the pellets (R=0.79mm and 1.19 mm at 38 °C) are shown in Figure 6.10 and 6.11. Based blank response it is clear that the system base line reached after 3 seconds but there is a drift when concentration is lower than 0.05, therefore to obtain reliable diffusivity value without the systematic error, the slope of long time asymptote was selecting in between the concentration from 0.1 to 0.05. The diffusional time constants can be estimated clearly from the plots, since the desorption curves of three highest flowrates (20, 30 and 45 cc/min) are nearly parallel to each other, in conformity with the kinetic control limit.

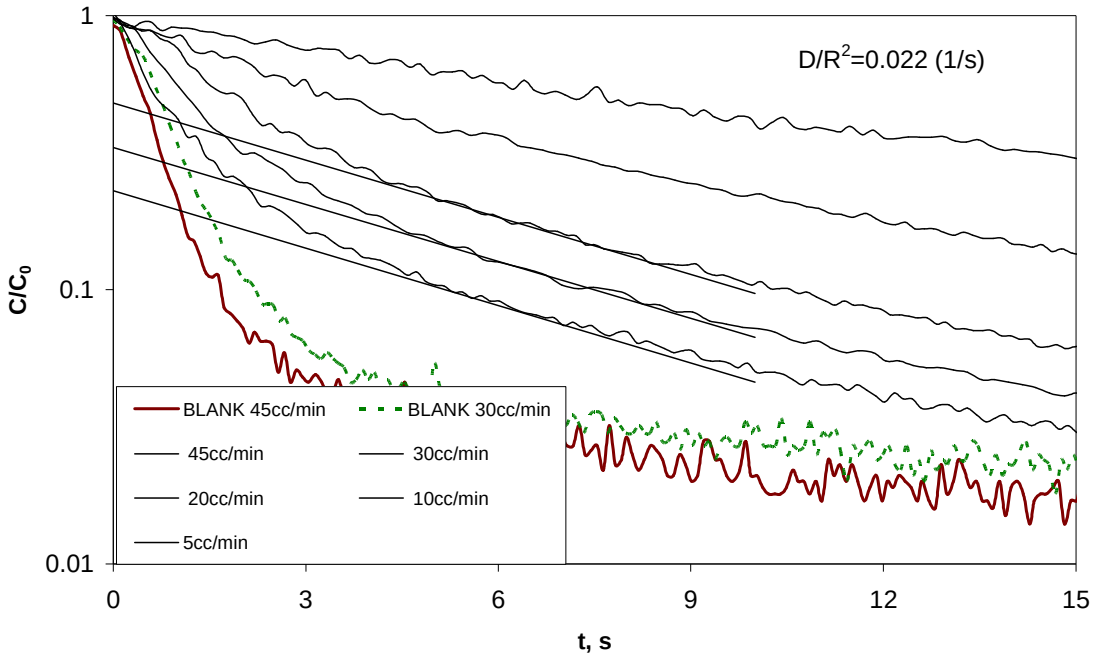

Figure 6.10 Experimental ZLC response curves of Ni/DOBDC pellet (R = 0.79 mm) at 0.1bar of CO_2 in Helium, 38 °C, 5, 10, 20, 30, 45 cc/min and the blank response at 30, 45 cc/min.

From the results on Co/DOBDC crystals we assumed that the micropore diffusivity in similar materials is at least 10^{-12} m^2/s, this means that for a 1 µm crystal the corresponding micropore diffusional time constant (R^2/D) should be less than 1s. The kinetic response observed on Ni/DOBDC pellet is clearly much slower than this. The diffusional time constant obtained from the ZLC desorption curves allows a direct comparison between the two pellet sizes, i.e. 0.022/0.009 = 2.4 can be compared directly with $(1.19/0.79)^2 = 2.3$. This shows that within the experimental uncertainty the data are consistent with macropore diffusion control. For a macropore controlled system, the time constant derived from the ZLC response curve represents D/R_p^2 (R_p represents the radius of particle) rather than D/r_c^2 (r_c represents the radius of crystal).

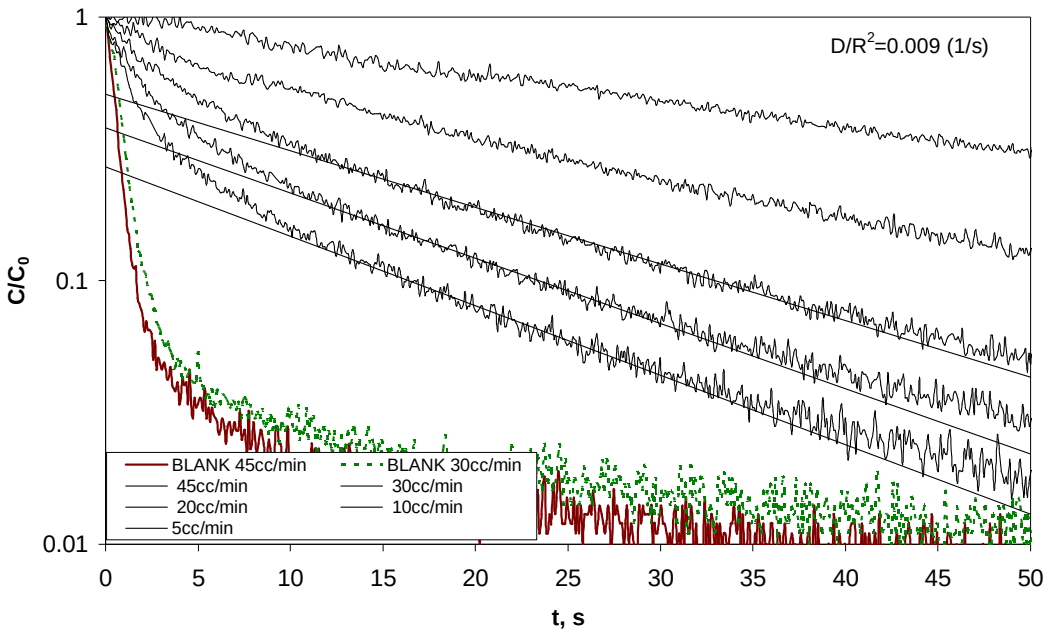

Figure 6.11 Experimental ZLC response curves of Ni/DOBDC pellet (R = 0.79 mm) at 0.1bar of CO_2 in Helium, 38 °C, 5, 10, 20, 30, 45 cc/min and the blank response at 30, 45 cc/min

The validity of the assumption that the Ni/DOBDC pellet is under macropore diffusion control may be conveniently verified by using different purge gases (He and N_2) which have different molecular diffusivities. If the mass transfer rate is controlled by intracrystalline diffusion, desorption curves measured under similar conditions with different purge gas, should be identical [59]. The experiments were repeated on the largest pellet (R = 1.19 mm) by using N_2 as the purge gas under the same condition. Figure 6.12 shows that the Ft plot confirmed kinetic control on the pellet. Figure 6.13 shows the comparison of the replicate desorption curves obtained with helium and nitrogen purge gas. It can be seen that desorption curves are dependent of the gas providing further experimental confirmation of macropore diffusion control.

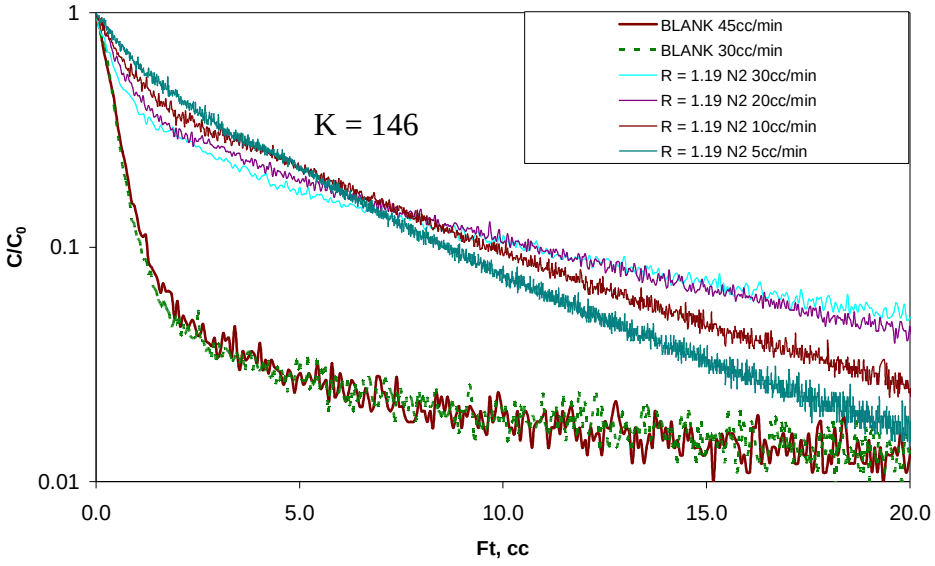

Figure 6.12 Experimental Ft plot of Ni/DOBDC pellet (R = 1.19 mm) at 0.1bar of CO_2 in Nitrogen, 38 °C, 10, 20, 30, 45 cc/min and the blank response at 30, 45 cc/min

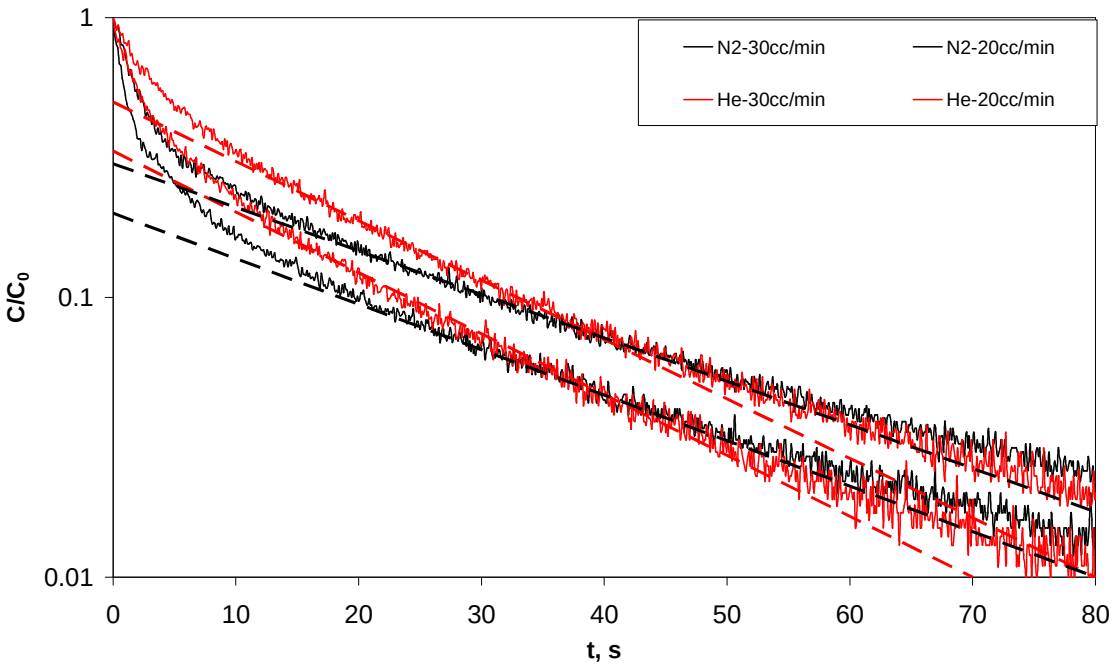

Figure 6.13 Comparison of experimental ZLC response curves of Ni/DOBDC pellet (R = 1.19 mm) at 0.1bar of CO_2 in two different purge gas (N_2 and He), 38 °C, 20 and 30 cc/min

From a ZLC experiment we can obtain D_P/R_P^2 from the slope of the long time asymptote at higher flowrate as shown in Figures 6.10, 6.11 and 6.13 and the $\varepsilon_P + (1-\varepsilon_P)H$ data of the low flowrate in the Ft plot (Figure 6.7, 6.8 and 6.9). In the tests we used all the equilibrium and kinetic information (Eq.2.34 and Eq.2.11) of pellets (R = 0.79, R = 1.19) by applying equation 2.23 to obtain an estimate of the macropore void fraction which is shown on table 5.3, the estimated value are consistent and reasonable value considering that the pellets are made from a powder with a relatively wide particle size distribution, this is needed to get close packing (i.e. $\varepsilon_P < 1$).

Table 6.2 Summary of Parameters from the ZLC Analysis of Ni/DOBDC pellets.

Equivalent Radius (mm)	**Carrier Gas**	$\varepsilon_P + (1-\varepsilon_P)H$	**D_p/R^2 (1/s)**	**D_m of CO_2 (mm^2/s)**	**ε_P**	**τ**
0.79	Helium	205	0.022	$0.625*10^2$	0.21	4.7
1.19	Helium	204	0.009	$0.625*10^2$	0.20	4.9
1.19	Nitrogen	146	0.045	$0.164*10^2$	0.24	4.2

6.4 Ni/DOBDC extrudate

Pressing self-supporting pellets of Ni/DOBDC is labour and time-intensive, and is not conducive to direct scale up. As such, extrusion methods utilizing simple binders like alumina were explored in order to prepare samples for scale up and characterization. Alumina was identified as the optimal additive in terms of extrusion ease and physical properties of the dried material. Figure 6.14 shows the Ni/DOBDC extrudate, this kind of extrudate was made from powder which was first mixed with solvent and then extruded by syringe, after proper drying, the extrudate was formed. Similar to the compressed pellet, for the ZLC measurements the long piece of extrudate could not be loaded in a 1/8" Swagelok union fitting (ZLC column) and tested directly, Fragments of different length were cut off the material as shown in Figures 6.14 a and 6.14 b. the image was captured by cross section face and side face.

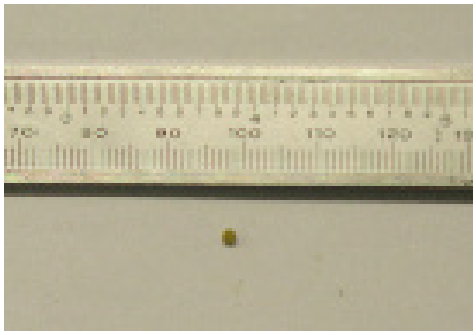

Cross-section face of Ni-MoF extrudate a

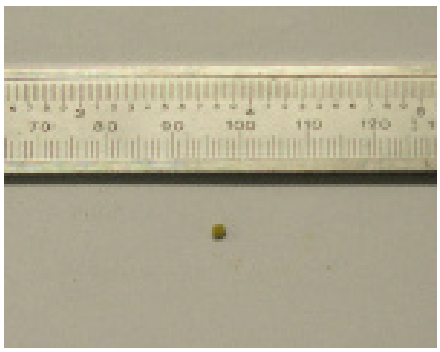

Side face of Ni-MoF extrudate a

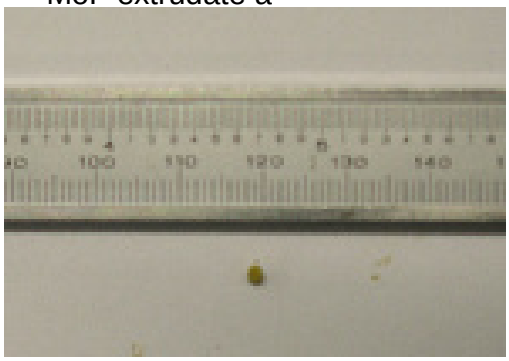

Cross-section face of Ni-MoF extrudate b

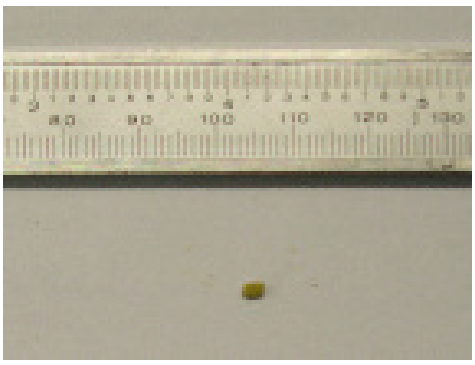

Side face of Ni-MoF extrudate b

Figure 6.14 Ni/DOBDC extrudate used in the kinetic experiments.

For dimension analysis and calculation, for mass transfer purposes the kinetics can be approximated by the behaviour of spheres that have the same surface to volume ratio = $3/R_{P.}$ Table 6.2 includes the dimensions measured by image analysis tool (GIMP) of the individual pellets and the equivalent radius calculated on this basis.

The thermal regeneration and ZLC measurements procedure on Ni/DOBDC extrudates were the same as that on Ni/DOBDC compressed pellet. For each sample, ZLC experiment runs at 5 different flow rates were performed in the range of 5 - 45 cc/min.

Table 6.3 Dimensions measured by image analysis tool (GIMP) of the extrudate and the calculated equivalent radius.

Material	**Mass of Sample (mg)**	**Diameter of cross-section of pellet (mm)**	**Length of pellet (mm)**	**Surface Area (mm2)**	**Volume (m m3)**	**Equivalent Radius (mm)**
Extrudate a	**5.1**	**1.933**	**2.133**	**18.829**	**6.263**	**0.998**
Extrudate b	**7.0**	**2.00**	**2.571**	**22.438**	**8.077**	**1.08**

Figure 6.15 shows the qualitative comparison of the CO_2 adsorption capacity for the different Ni-DOBDC fragment extrudate (R = 0.99 mm, R = 1.08 mm) at 0.1bar of CO_2 in Helium, 38 °C, 5 cc/min and the blank response. As the compressed Ni/DOBDC pellet fragments, this initial test confirmed the consistent adsorption capacities on these two extrudates. There is very little variation between the two extrudate fragments.

The experimental Ft plots for each Ni/DOBDC pellets tested of particle size 0.99mm, 1.08 mm are shown in Figures 6.16, 6.17 (10% CO_2 in Helium, 38ºC, Flowrate = 5,10, 20, 30 and 45 cc/min) respectively. The Ft plots clearly show divergence for these two fragments, indicating that desorption is kinetically controlled. At a lower flowrate (5cc/min), the desorption response shows a linear decay, which means at such low a flowrate, the system is closer to equilibrium control, therefore the Henry law constant K of the fragment can be estimated from the slope.

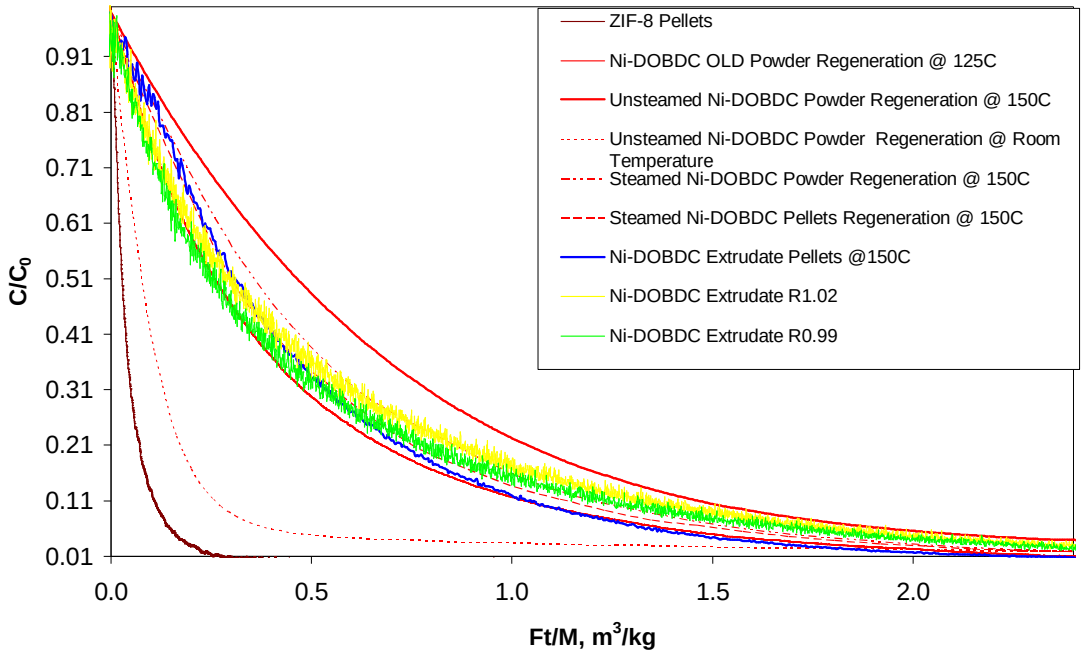

Figure 6.15 Comparison of adsorbent capacity of different fragments.

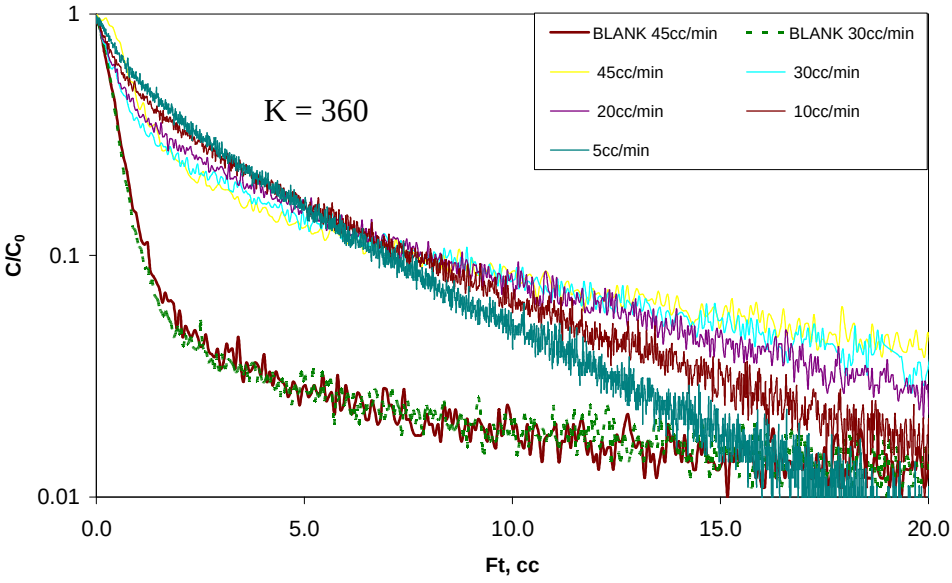

Figure 6.16 Experimental Ft plot of Ni/DOBDC extrudate (R = 0.99 mm) at 0.1bar of CO_2 in Nitrogen, 38 °C, 10, 20, 30, 45 cc/min and the blank response at 30, 45 cc/min

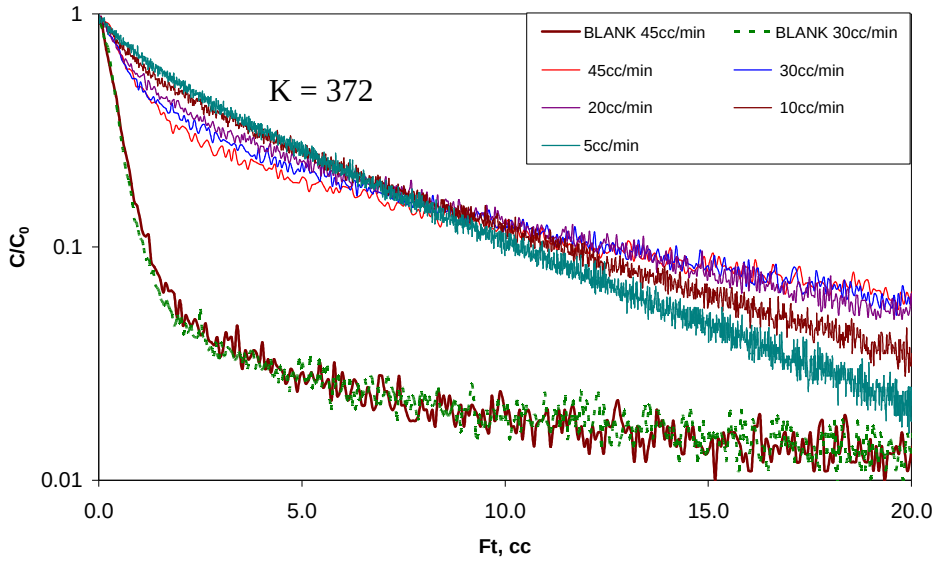

Figure 6.17 Experimental Ft plot of Ni/DOBDC extrudate (R = 1.08 mm) at 0.1bar of CO_2 in Nitrogen, 38 °C, 10, 20, 30, 45 cc/min and the blank response at 30, 45 cc/min

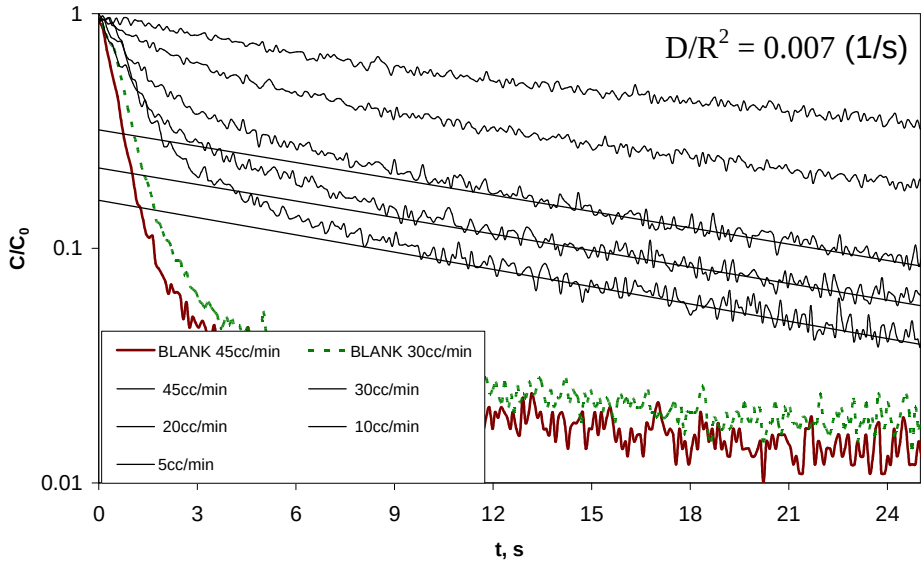

Figure 6.18 Experimental ZLC response curves of Ni/DOBDC extrudate (R = 0.99 mm) at 0.1bar of CO_2 in Helium, 38 °C, 5, 10, 20, 30, 45 cc/min and the blank response at 30, 45 cc/min

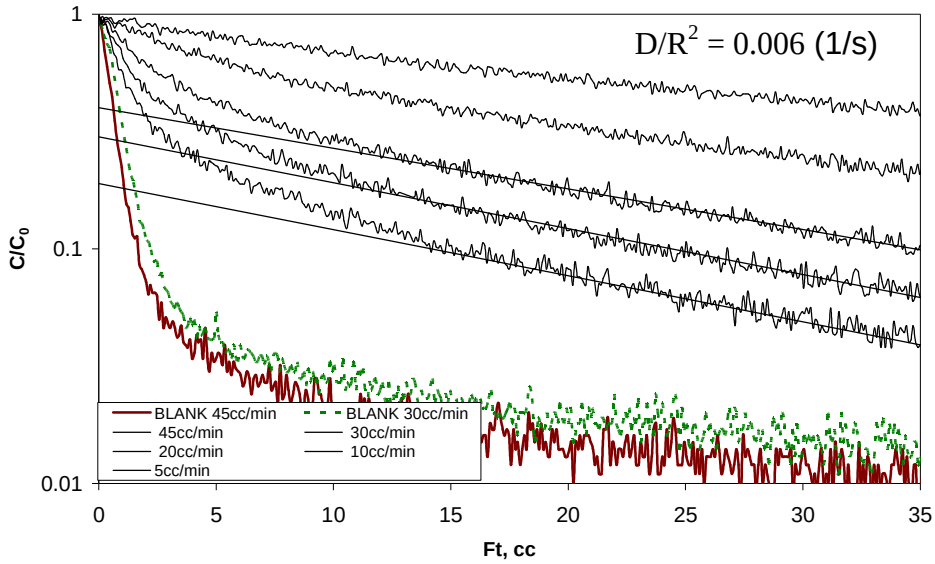

Figure 6.19 Experimental ZLC response curves of Ni/DOBDC extrudate (R = 1.08 mm) at 0.1bar of CO_2 in Helium, 38 °C, 5, 10, 20, 30, 45 cc/min and the blank response at 30, 45 cc/min

The ZLC desorption curve of the pellets (R=0.99mm and 1.08 mm at 38 °C) are shown in Figure 6.18 and 6.19. The diffusional time constants can be estimated clearly from the plots, since the desorption curves of three high flowrate (20, 30 and 45 cc/min) are nearly parallel to each other, in conformity with the kinetic control limit. With these slow desorption decay similar as Ni/DOBDC compressed fragment, it can be assumed that the desorption mechanism is also controlled by macropore diffusion. Table 5.4 shows the estimated tortuosity; fragment voidage and the average density of Ni/DOBDC extrudate based all the equilibrium and kinetic information (Eq.2.34 and Eq.2.11) as well as the comparison with largest compressed fragment. The estimated tortuosity values are consistent and slightly larger than the compressed fragments. The ratio of the density between Ni-DOBDC extrudate and

steamed Ni-DOBDC pellet is 1.426, the higher density is the explanation of the higher K value for the Ni/DOBDC extrudate.

Table 6.4 Summary of parameters from the ZLC analysis

Equivalent Radius (mm)	**Materials**	**ε_P**	**τ**	**Average Density (kg/m^3)**
0.99	Ni-DOBDC Extrudate a	0.190	5.2	840
1.08	Ni-DOBDC Extrudate b	0.199	5.0	
1.19	Ni-DOBDC Compressed Pellet	0.203	4.9	589

6.5 13X zeolite commercial pellet

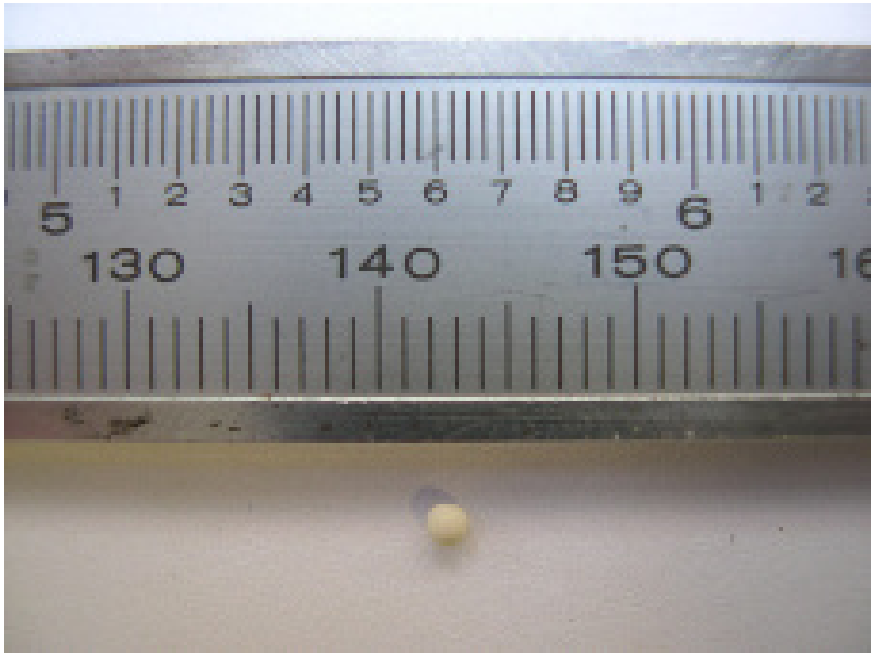

Figure 6.20 13X commercial pellet used in the kinetic experiments.

The ZLC system also used to study the diffusion behaviour of a 13X commercial pellet, Figure 6.20 shows the 13X pellet supplied by UOP, the radius of the pellet was measured by image analysis tool (GIMP) to obtain the volume of the pellet. The pellet shows an average diameter of approximately 1.6mm.

The ZLC column packed with one 13X pellet, to reduce the pressure drop in the column; the non-adsorbable rockwool was also filled in side the column. The ZLC column was thermally regenerated with a ramping rate of 1°C/min to 300°C and then held this temperature for 12h at 1 cc/min of the helium purge gas. And then, the oven temperature is reduced to 38°C and the flow system switch to high flowrate mass flow controllers. For each sample, ZLC experiment runs at 5 different flow rates were performed in the range of 5 - 45 cc/min. After that, the same ZLC column was thermally regenerated again in nitrogen and the same measurement were carried out with 10% CO_2 in N_2.

The adsorption of CO_2 in 13X zeolite is nonlinear as determined in chapter 4. If the pellet system is micropore controlled, the nonlinear asymptotic solution to the ZLC model may be used to calculate at zero loading diffusivity. The Ft plot using two different purge gases (He and N_2) are presented in Figures 6.21 and 6.22, respectively. Compare to the desorption curve of Ni/DOBDC MOF, the zeolite shows high non-linearity. Brandani [61] developed the model for ZLC experiments to analyze the effect of nonlinear equilibrium on the resulting apparent diffusivities. From the practical point of view we come to the conclusion that nonlinearity affects

the intercept of the ln (c/c_0) vs. t plot but has negligible effect on the slope at long time. Therefore the ratio of the long time asymptote slope is still reflecting the ratio of diffusivity.

Figure 6.23 shows the comparison of the replicate desorption curves obtained with helium and nitrogen purge gas. It can be seen that the desorption curves are dependent of the gas. The ratio of the two diffusivities and the ratio of the slope are approximately 2, which confirms macropore diffusion control.

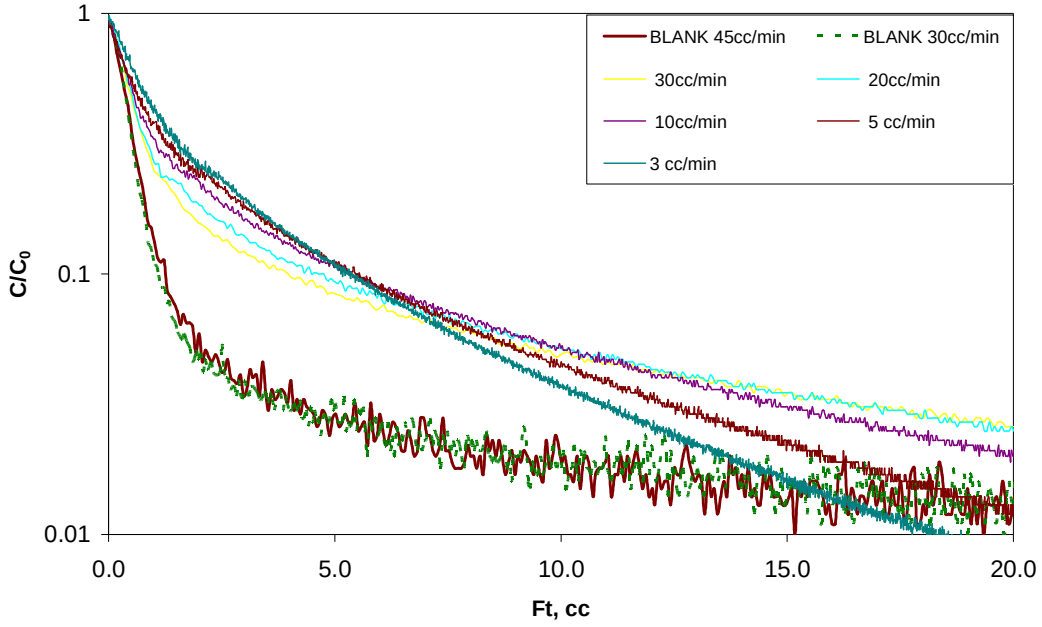

Figure 6.21 Experimental Ft plot of 13X (R = 1.6 mm) at 0.1bar of CO_2 in Nitrogen, 38 °C, 10, 20, 30, 45 cc/min and the blank response at 30, 45 cc/min

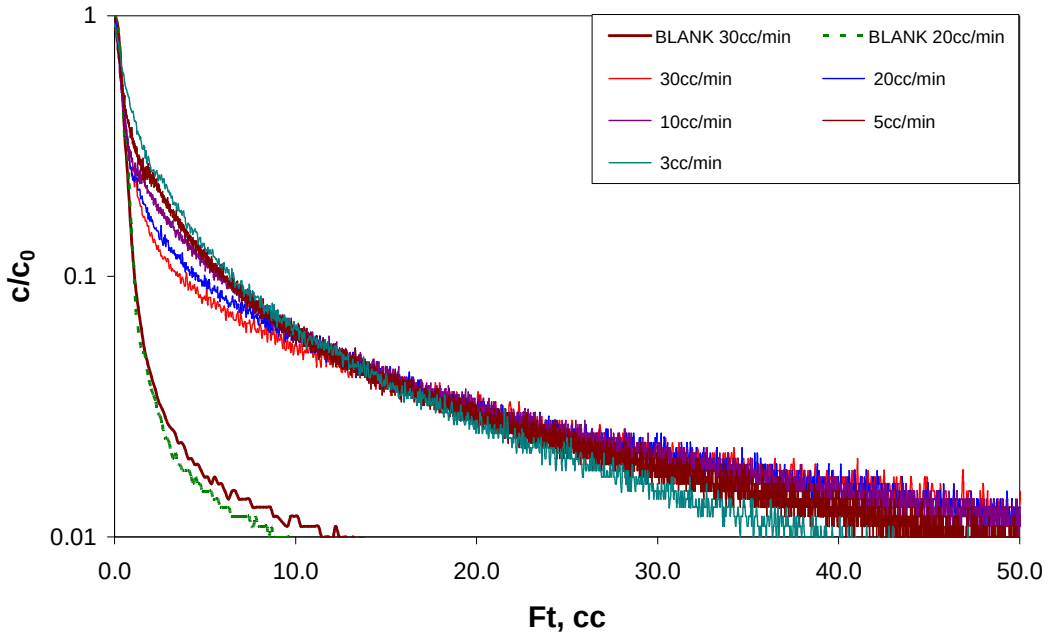

Figure 6.22 Experimental Ft plot of 13X (R = 1.6 mm) at 0.1bar of CO_2 in Nitrogen, 38 °C, 10, 20, 30, 45 cc/min and the blank response at 30, 45 cc/min

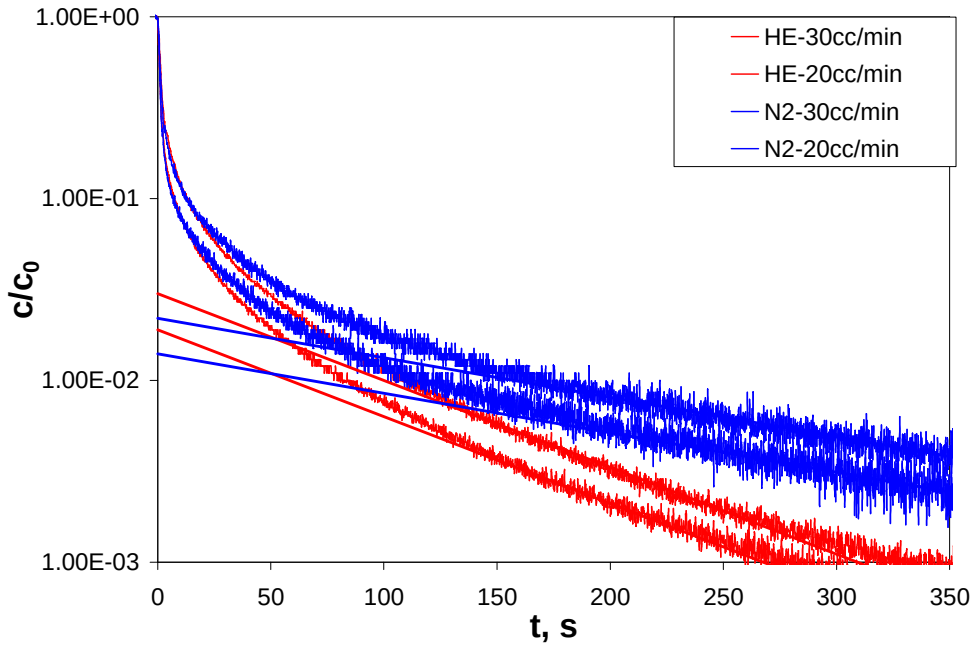

Figure 6.23 Comparison of experimental ZLC response curves of 13X pellet (R = 1.19 mm) at 0.1bar of CO_2 in two different purge gas (N_2 and He), 38 °C, 20 and 30 cc/min

6.6 Conclusion

ZLC kinetic experiments were carried out on both powders and pellets. The main difference is that in the case of powders the mass transfer resistance is typically due to internal diffusion in the crystals, while for pellets one can also have diffusion in the macropores. What is important is that in order to be able to measure diffusivities one has to run the ZLC under conditions that are far from equilibrium control.

The semi-automated ZLC technique can provide a simple method to study the diffusion behaviour of novel adsorbents, i.e. Co/DOBDC crystals, Ni/DOBDC compressed pellets, Ni/DOBDC extrudate and 13X commercial pellet. For Co/DOBDC crystals, since the system it close to equilibrium control even at the highest flow rate, only an estimate of a lower bound can be made, the diffusivity is greater than $2x10^{-12}$ m^2/s. For Ni/DOBDC pellets Ni/DOBDC extrudate and 13X pellet, the results showed macropore diffusion control. This was confirmed by carrying out experiment with different pellet sizes and changing the carrier gas.

CHAPTER 7

7. SCREENING STABILITY MEASUREMENTS OF NOVEL ADSORBENTS

7.1 Introduction

Metal organic frameworks (MOFs) are characterised by their large surface areas, controllable pore structures, and versatile chemical compositions [38]. In the capacity ranking chapter, some of the MOFs with open metal sites (M/DOBDC， M = Zn, Ni, Co, Mg) show extremely high CO_2 capacity and very desirable isotherm shapes. Therefore, these MOFs are considered to be potential candidates for carbon capture. For MOFs to be suitable for industrial application, it is important to

understand how stable they are in a typical flue gas. Currently, however, the experimental information on MOF stability is still quite scarce in the literature.

The previous chapters discussed developing the semi-automated ZLC system to screen and rank the CO_2 adsorption capacity of novel adsorbents and to study the kinetic behaviour of CO_2 in M/DOBDC MOFs, since they demonstrated the most promise for CO_2 adsorption capacity at these low pressure conditions. The goal of this chapter is to show how to use the new ZLC system to help clarify the performance of M/DOBDC MOFs under realistic operating conditions by using humid gas, humid gas with CO_2, and synthetic wet flue gas. Since a very small amount of sample is required for loading into the ZLC column (10-15 mg), compared to a typical breakthrough experiment set up or even real plant, in which columns contain up to gram or kilogram amount, a large time scale can be avoided for monitoring the same volume of flue gas per weight of adsorbent elutriate that flows through in the real plant, in addition to reducing gas consumption, it is also possible to arrive at a result in a few days compared to several months of operation in a pilot plant.

7.2 Experiment

7.2.1 Adsorbent

The stability study focused on the potential CCS candidate MOFs (Co/DOBDC, Ni/DOBDC, and Mg/DOBDC powder) and commercial zeolites as a benchmark

7.2.2 Experimental setup

The semi-automated ZLC apparatus is applied to measure the stability of adsorbents. The individual dosing system is especially useful to prepare mixtures with accurate concentrations of water vapour, and wet flue gas in the determination of the effect of humidity and acids on adsorbents. The formulation of flue gas supplied by the gas supplier (BOC) is shown in Table 7.1. Water could not be included, since at high pressure (200 bars) it would have condensed in the cylinder leading to corrosion problems. Since the ZLC system contains an independent dosing volume, a certain concentration of water can be added to the flue gas without problems. Oxygen was not included since it is incompatible with SO_2 at high pressure, but this will not have a major effect, since in adsorption on MOFs O_2 and N_2 are likely to have similar properties.

• Preliminary tests

In the preliminary test, 10% CO_2 in helium and a few thousands ppm of water was prepared in the 10% CO_2 and helium. Prior to the experiment, the ZLC column was packed and then thermally regenerated with a ramping rate of 1°C/min to the required activation temperature (Table 5.1), and then held at this temperature for 12h at a very low flow rate of the helium purge gas, i.e. 1 cc/min. After regeneration, the oven temperature was reduced to the standard temperature (i.e. 38°C) automatically. In a preliminary test, a typical ZLC experiment was first carried out on a fresh sample to obtain the original CO_2 capacity. Then, the sample was regenerated again

and cooled down to 38°C, a mixture with 10% CO_2 and several thousands ppm of water in helium was introduced into the column, after a certain time, the valve was switched and the desorption of CO_2 response was followed by MS. By comparing the response with the original sample, the effect of water in the mixture was obtained.

Table 7.1 Key synthetic wet flue gas characteristics for ZLC tests

CO_2 concentration (%)	16
NO_x (ppm)	10
SO_x (ppm)	100
N_2	Balance
Moisture (%)	1 (prepared by dosing volume)

• Stability tests

For stability measurements, the sample was regenerated as usual, and then a typical ZLC experiment was carried out on a fresh sample with 16% of CO_2 in nitrogen. Thereafter, the sample was exposed to the mixture gas* for a certain time, followed by intermediate regeneration (same procedure as fresh sample). The ZLC runs were carried out on the adsorbent to evaluate the residual CO_2 capacity. If the sample was still active, a further additional time (i.e. 24h) of exposure would be applied until the sample was fully deactivated or until it maintained a constant capacity. After this a

new ZLC column was packed and the same procedure as shown above was applied to the other three mixtures. The four different mixtures of gases are:

*1% v/v water in nitrogen (humid gas)

*1% v/v water and 16% v/v CO_2 in nitrogen (weak acid gas).

* Synthetic 'Dry' (original gas from gas supplier) flue gas

* Synthetic wet (1% v/v water) flue gas

7.3 Preliminary water experiment

In this preliminary test, the Ni/DOBDC MOF sample was first tested with 10% CO_2, 5000ppm (and 2000ppm) of water in helium. Initial tests had been run exposing the column to water and CO_2 for only two hours, but the results shows close capacity result of the experiments with the original activated sample, shown in Figure 7.1, but the mass loss from the Rubotherm gravimetric system (Vanderbilt University) shows that the Ni/DOBDC sample could adsorb up to 33% by weight of water. this indicates that at the concentration and flow rates used, one hour of exposure could achieve only partial saturation and the time required for full saturation could be up to several hours.

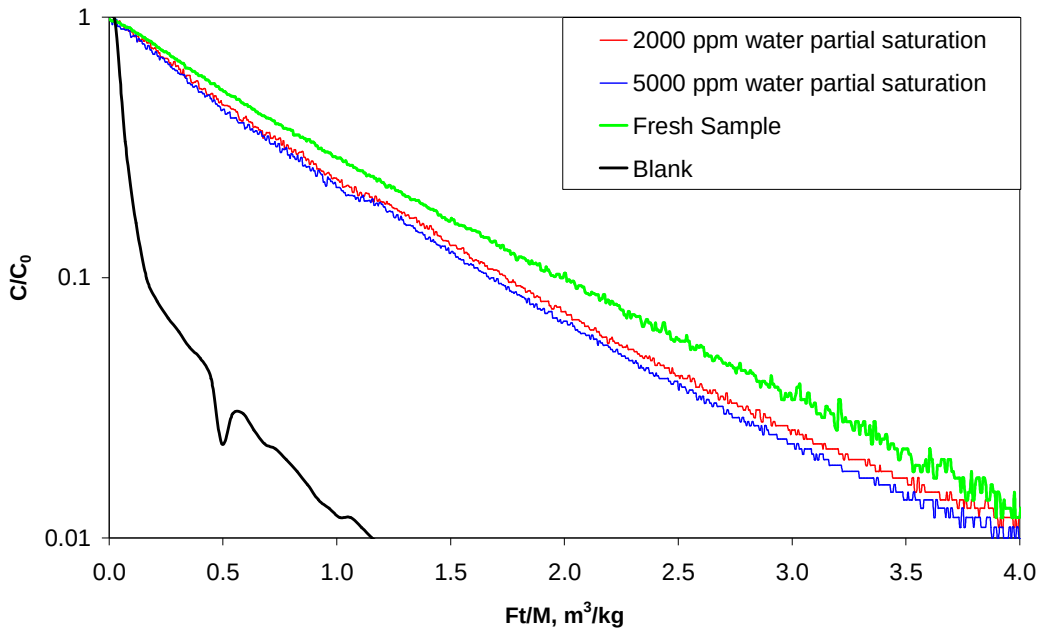

Figure 7.1 Ni/DOBDC results after exposure to humidity (2000ppm and 5000ppm water in helium) gas.

To understand this better, blank runs (ZLC column containing non adsorbing rock wool) (Figure 7.2) were carried out with 10% CO_2, 5000ppm of water in helium to check and calibrate the system. Figure 7.2 shows the monitored signal during the exposure. It is clear that the transient for CO_2 is very fast, while water takes approximately 2 to 3 hours to reach saturation. The slower response of water signal indicates that the water could be adsorbed on the metal surfaces or in the vacuum pump of the mass spectrometer since the lines before the MS were heated and cleaned to avoid presence of residual adsorbent. Figure 7.3 shows the MS signal on the fully regenerated Ni/DOBDC sample, in this case water saturation is achieved after more than 6 hours, confirming the gravimetric results.

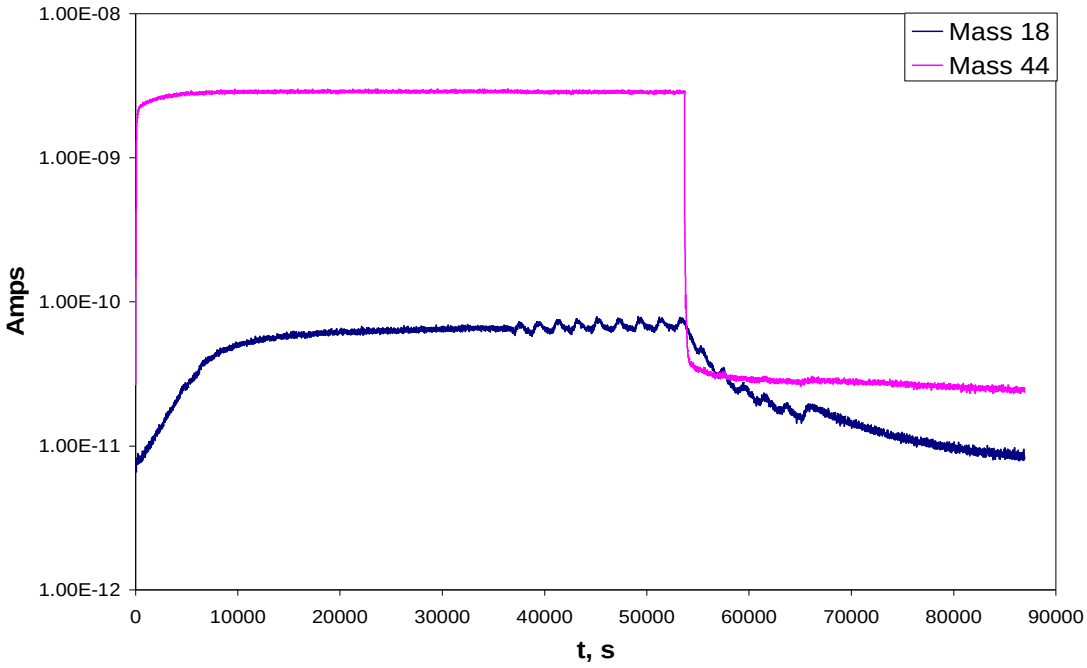

Figure 7.2 Blank runs (ZLC column contains non adsorbable rock wool) shows applied with 10% CO_2, 5000ppm of water in helium

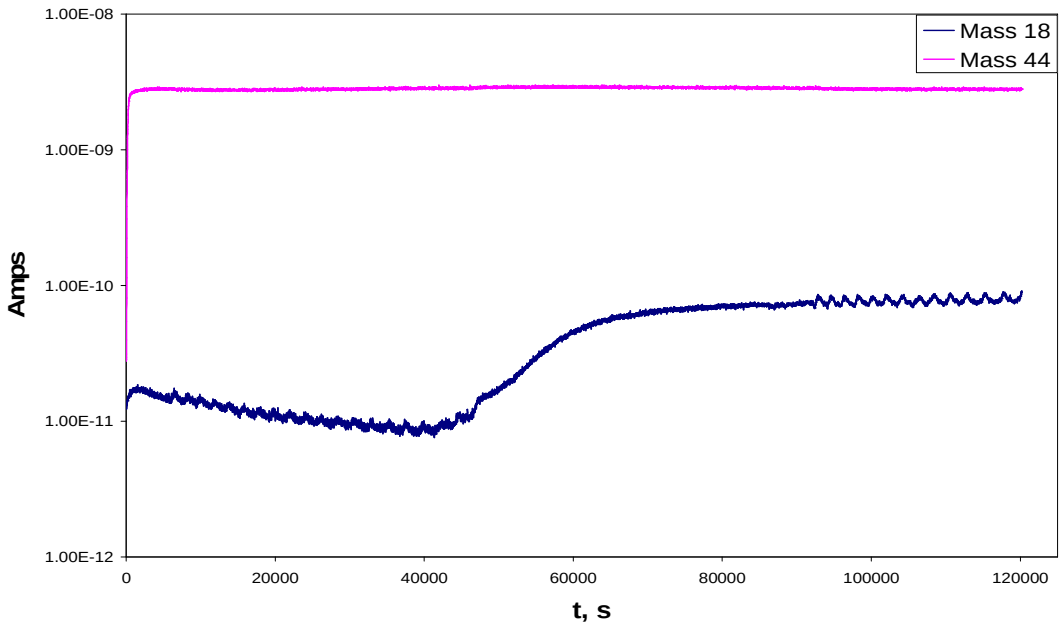

Figure 7.3 ZLC runs of Ni/DOBDC with 10% CO_2, 5000ppm of water in helium

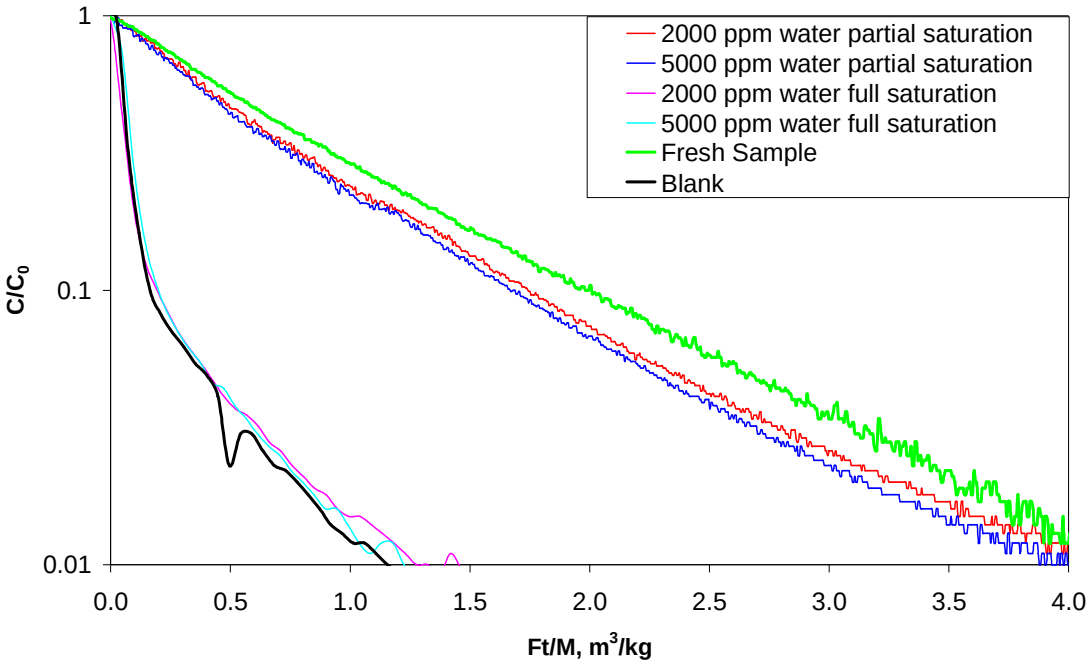

Figure 7.4 Ni/DOBDC results after exposure to humidity (2000ppm and 5000ppm water in helium) gas by partial saturation and full saturation.

Figure 7.4 shows the comparison of the curves with the fully regenerated sample runs and the results from the experiments with partial water equilibration (2 hours) and full saturation. Compared to the blank curves, once saturated with water the Ni/DOBDC MOF does not have an appreciable capacity for CO_2. For this experiment, one of the issues that need to be considered carefully was that the amount of time needed to saturate fully the sample.

Gas mixtures were prepared with 2000 ppm and 5000 ppm of water and applied to the other two M/DOBDC (Co, Mg) samples and 5A zeolite. The desorption after full saturation shows in Figure 7.5 proved the strong hydrophilic nature of these MOFs

and zeolite, so in the presence of even low quantities of water, once the sample has reached equilibrium, the adsorbed phase is effectively saturated and the sample does not show any CO_2 capacity.

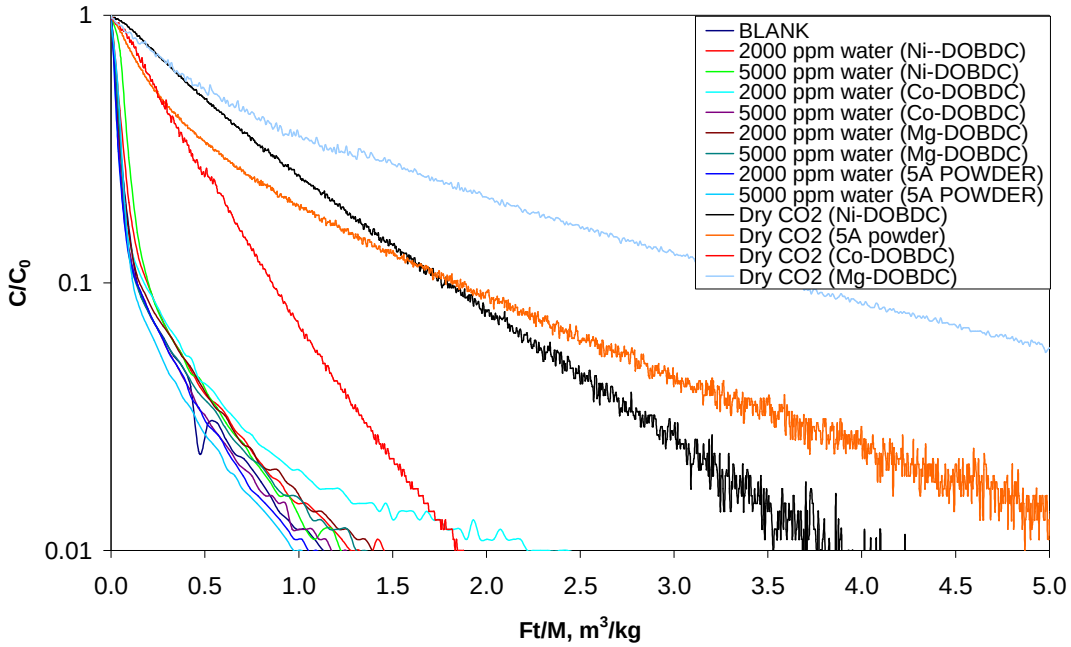

Figure 7.5 Adsorbents (Co, Ni, Mg/DOBDC and 5A) capacity after exposure to humidity (2000ppm and 5000ppm water in helium) gas by full saturation.

Since the M/DOBDC sample showed high CO_2 adsorption capacity compared to the traditional zeolite, they are considered to have hydrophilic surfaces as well, which generally have strong interactions with H_2O molecules. Therefore in a process design using a MOF or another adsorbent, it may be advantageous to utilize a guard bed to adsorb water and thereby minimize H_2O effects on the adsorbent targeted for CO_2 capture.

7.4 Stability test

It is important to understand the effects of impurities (humidity and acid gases) on CO_2 adsorption in adsorbent samples before making any conclusions about their applications in process designs to separate CO_2 in a carbon capture plant. In order to accelerate sorbent development, the effect of actual flue gas constituents on sorbent performance must be known.

7.4.1 Water stability

In the first part of our study, ZLC runs were first applied on the regenerated fresh sample to check the CO_2 capacity. After exposing the sample to a gas mixture for a set period of time, the sample was prepared for capacity testing using an intermediate regeneration. ZLC runs were carried out at periodic intervals for the MOF samples to check the residual CO_2 capacity. Figures 7.6, 7.7 and 7.8 show the ZLC response curves at 38 °C for Co/DOBDC, Ni/DOBDC and Mg/DOBDC powder, respectively. Based on Eq.6, the area between the ZLC curve and the blank curves is proportional to the CO_2 capacity, with different times of humidity gas (1% v/v water in nitrogen) exposure. It can be seen in Figure 7.6 that Co/DOBDC had almost lost all capacity after the first 24 hours of exposure. However, Figure 7.7 indicates that Ni/DOBDC is very stable in the presence of water and thermal regeneration. Mg/DOBDC also lost about half of its CO_2 capacity after the first 24 hours of exposure, but thereafter, the rate of loss in capacity decreased as can be seen in Figure 7.8.

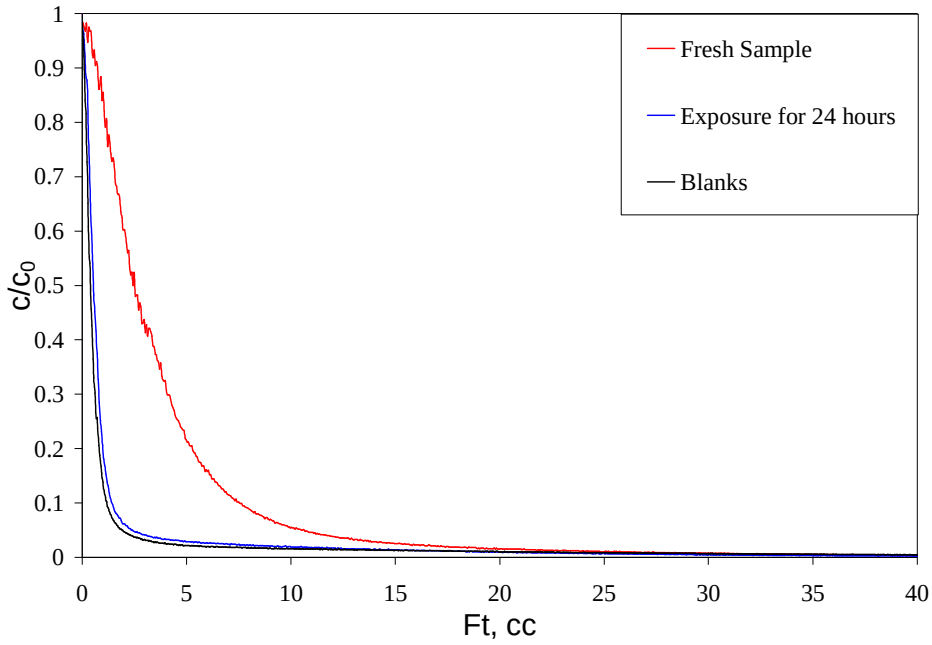

Figure 7.6 Co/DOBDC stability results after exposure to humidity (1% v/v water in nitrogen) gas.

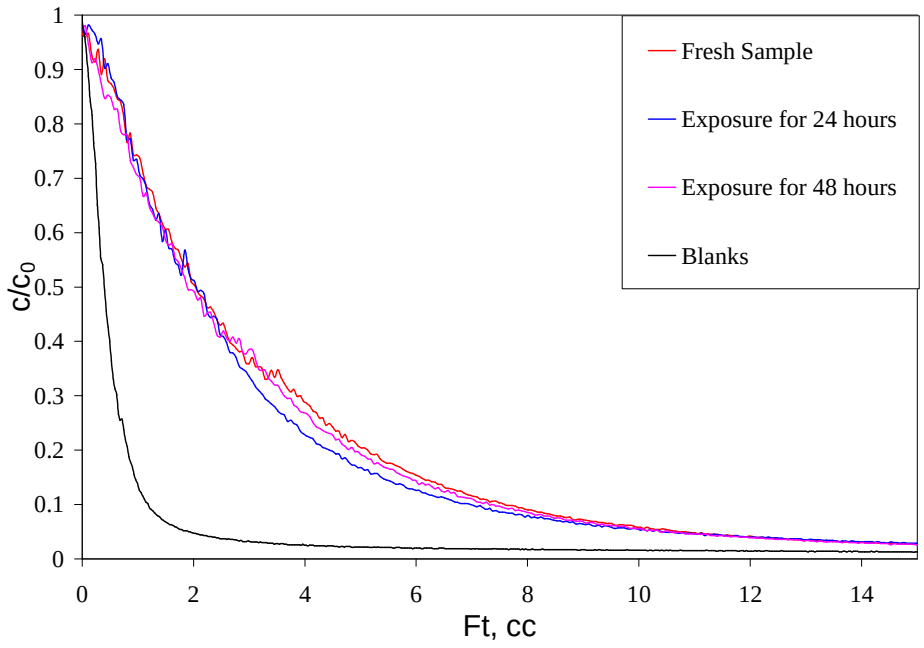

Figure 7.7 Ni/DOBDC stability results after exposure to humidity (1% v/v water in nitrogen) gas.

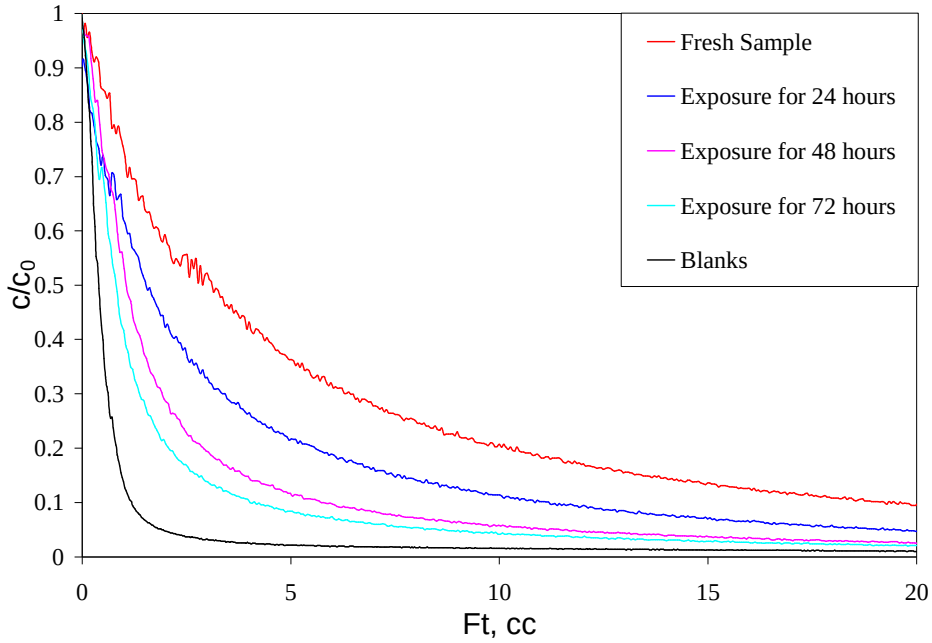

Figure 7.8 Mg/DOBDC stability results after exposure to humidity (1% v/v water in nitrogen) gas.

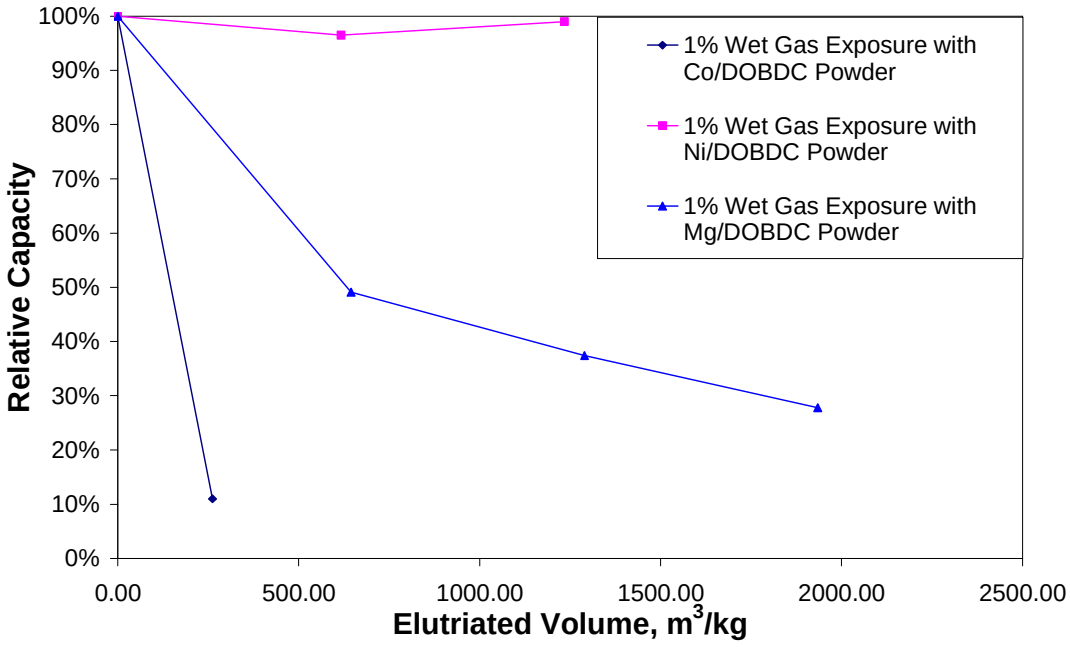

Figure 7.9 Comparison of the stability tests with humidity gas (1% v/v water in nitrogen).

Figure 7.9 is a plot of the relative CO_2 capacity versus elutriated gas volume per adsorbent weight. It shows the comparison between the three MOFs; Ni/DOBDC shows the best stability. Although these three MOFs are synthesized through solvothermal reactions, Co/DOBDC and Mg/DOBDC still show their lack of hydrostability.

7.4.2 Water and CO_2 stability

In the second part of the experiment, the exposure work was applied to three MOFs with 1% water, and 16% CO_2 in nitrogen. The results are shown in Figures 7.10, 7.11, and 7.12. From Figure 7.10, it can be seen that the CO_2 capacity of Co/DOBDC decreases rapidly after the first 24 hours of exposure runs in the water stability test; the residual capacity is very close to the blank. However, even the Ni/DOBDC sample showed excellent stability to water, but when the sample was exposed to weak acid gas there was a progressive loss of capacity, which can be seen in Figure 7.11. In Figure 7.12, Mg/DOBDC just retains about one third of CO_2 capacity after the first 24 hours of exposure; thereafter, the capacity decay became slower.

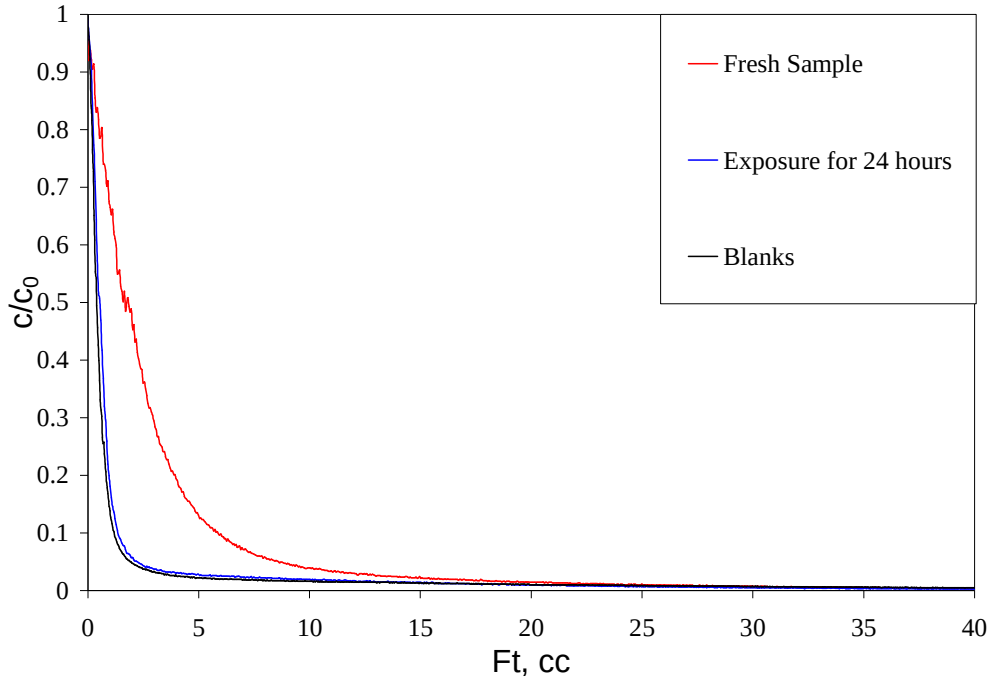

Figure 7.10 Co/DOBDC stability results after exposure to humidity (1% v/v water, 16% v/v CO_2 in nitrogen) gas.

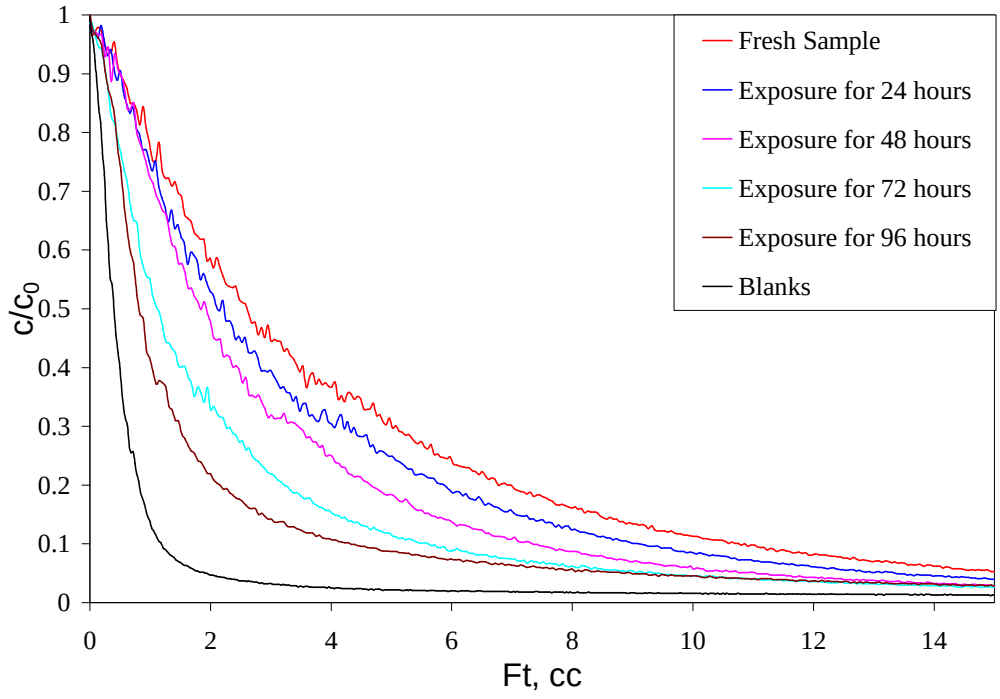

Figure 7.11 Ni/DOBDC stability results after exposure to humidity (1% v/v water, 16% v/v CO_2 in nitrogen) gas.

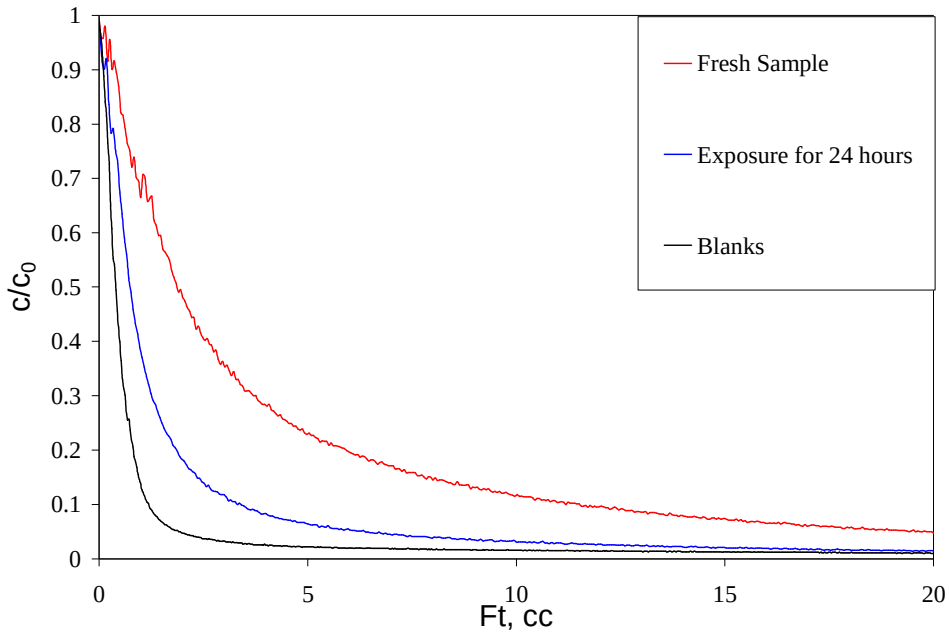

Figure 7.12 Mg/DOBDC stability results after exposure to humidity (1% v/v water, 16% v/v CO_2 in nitrogen) gas.

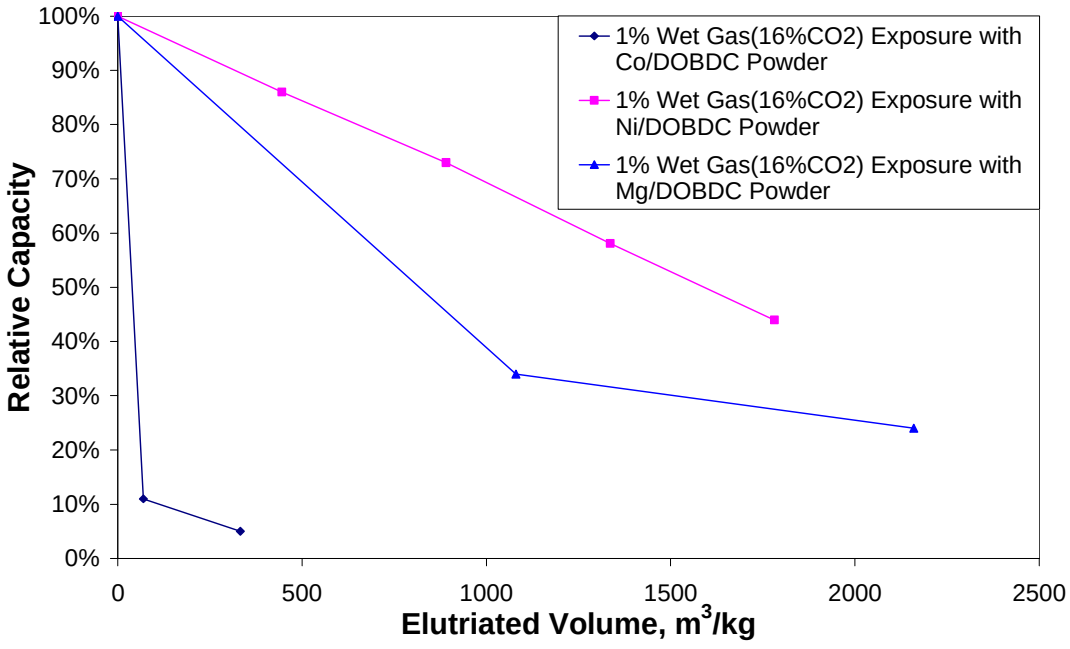

Figure 7.13 Comparison of the stability tests with humidity gas (1% v/v water, 16% v/v CO_2 in nitrogen).

A comparison of the three MOFs is shown in Figure 7.13. Compared with the other two DOBDC MOFs, Ni/DOBDC is better at maintaining its CO_2 capacity after multiple exposures to water vapour and CO_2 and multiple thermal regeneration processes, which means that it is somewhat prone to degradation in weak acid exposure and heat treatments. Most of the deactivation on Co/DOBDC and Mg/DOBDC is due to the effect of water.

7.4.3 'Dry' flue gas stability

Exposure measurement using synthetic flue gas was first attempted on the original synthetic flue gas with out water supplied by BOC, however, from the mass spectrometer signal in Figure 7.14 we can see that the synthetic flue gas is not completely dry. Mass 18 shows water to breakthrough after 20 hours, however, we can not implement a drying column in the flue gas line since it will adsorb SO_2 and NO as well.

The result of 'dry' flue gas stability on Mg/DOBDC MOF is shown in Figure 7.15. There is a clear effect due to the flue gas. The capacity gas has permanently destroyed the MOF sample, but there is capacity left even after 96 hours exposure.

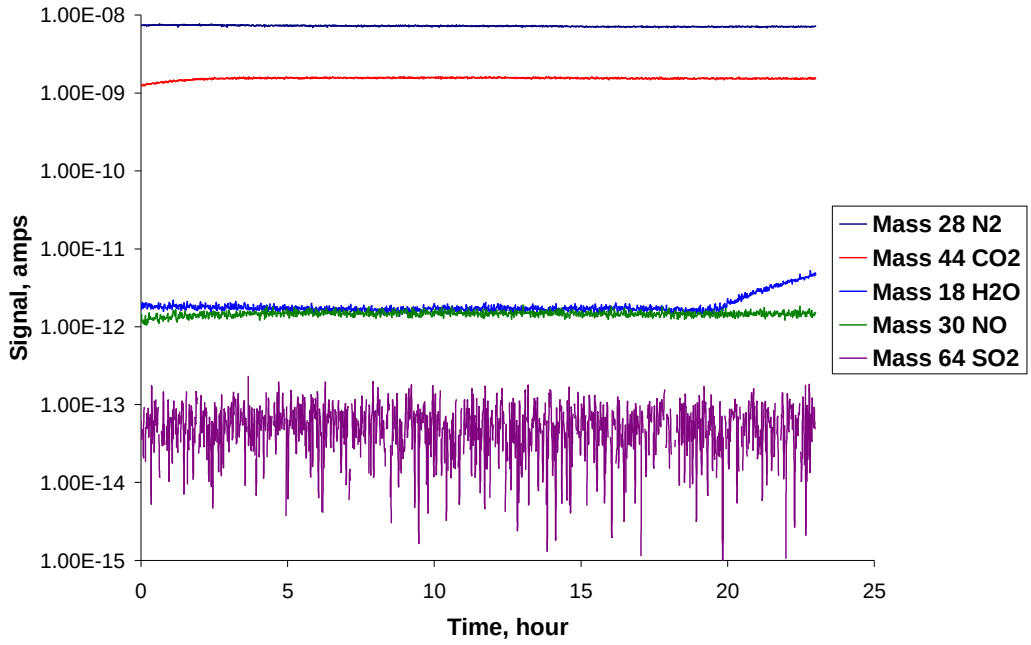

Figure 7.14 MS monitored signal during 'dry' flue gas exposure on Mg/DOBDC.

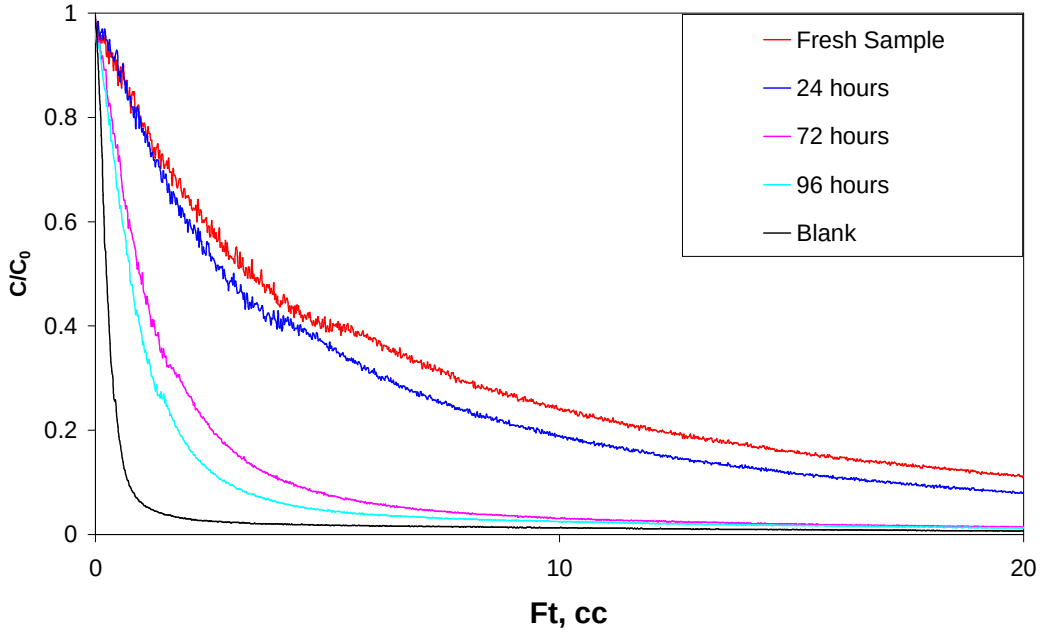

Figure 7.15 Mg/DOBDC stability results after exposure to flue gas supplied by BOC.

7.4.4 Wet flue gas stability

1 % v/v water was added to the synthetic flue gas, the results of wet flue gas stability on M/DOBDC MOFs and zeolite 13X are shown in Figures 7.16, 7.17, 7.18 and 7.19. From Figure 7.16, one can see that the behaviour of the Co/DOBDC sample is significantly different from the other two mixture stability tests. What is interesting in this case is the fact that the shape of the isotherm has changed. The effect of the wet flue gas seems to make the adsorption sites stronger, so the isotherm, after the first treatment, shifts to a non-linear one.

The Ni/DOBDC sample showed excellent stability in water, with full regeneration at 150 °C. When the samples were tested with wet flue gas there was a progressive loss in capacity (Figure 7.17). What is interesting to note from the stability results is that the capacity loss seems to be uniform, i.e. at each extended exposure more material is deactivated but the general shape of the isotherm and of the ZLC response remains the same.

Figure 7.18 shows the results for the Mg/DOBDC sample. There is an additional effect due to the flue gas, but it is clear that in this case most of the deactivation is due to the effect of water. For this sample, the shape of the ZLC curve does not change qualitatively.

Figure 7.19 shows the results for zeolite 13X plotted in semi-logarithmic form because the effect of purities in wet flue gas on this zeolite was very small. There is some loss in the first 24 hours of exposure, followed by a slower decay.

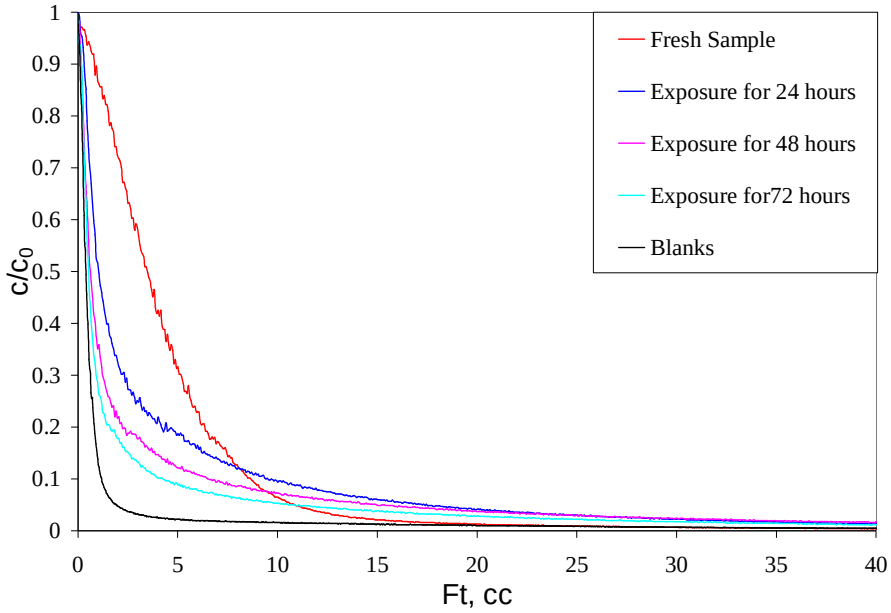

Figure 7.16 Co/DOBDC stability results after exposure to wet (1% v/v water) flue gas.

Since the MOF samples were powders and the 13X was a pellet, the slow capacity decay on 13X pellet could also be explained by a shrinking core model, i.e. the wet flue gas was deactivates the external layer of the pellet, resulting in slow decay of capacity loss. To confirm this hypothesis, a new pellet was selected and crushed into fine powder, the ZLC column was packed by using similar a mass of 13X powder and loaded on the system. The same procedure as for the 13X pellet was applied to the crushed powder to check the stability results. Figure 7.20 shows the stability test results for the 13X powder. It is clear that the trend of capacity loss on 13X powder is similar to that for the pellet. It confirmed the good stability of this type of zeolite and excluded a shrinking core type mechanism.

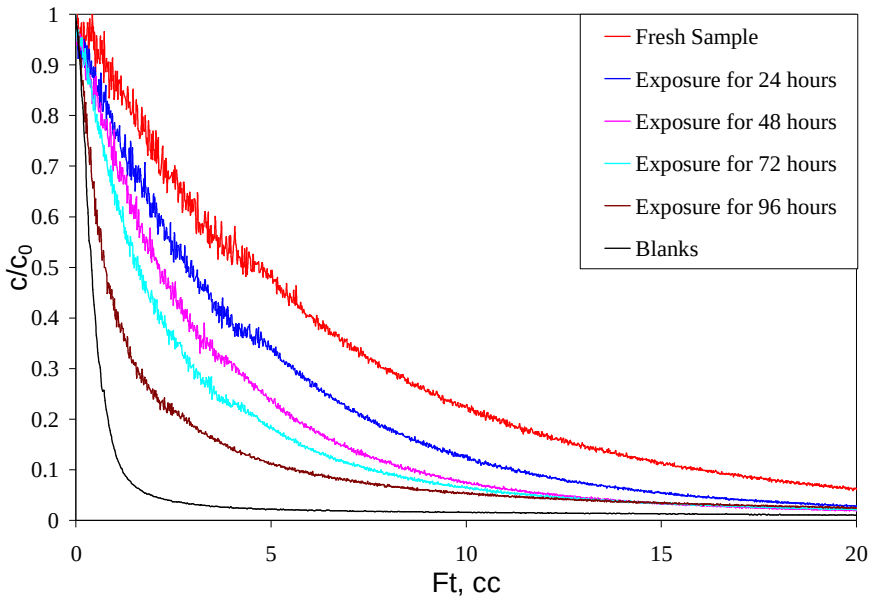

Figure 7.17 Ni/DOBDC stability results after exposure to wet (1% v/v water) flue gas.

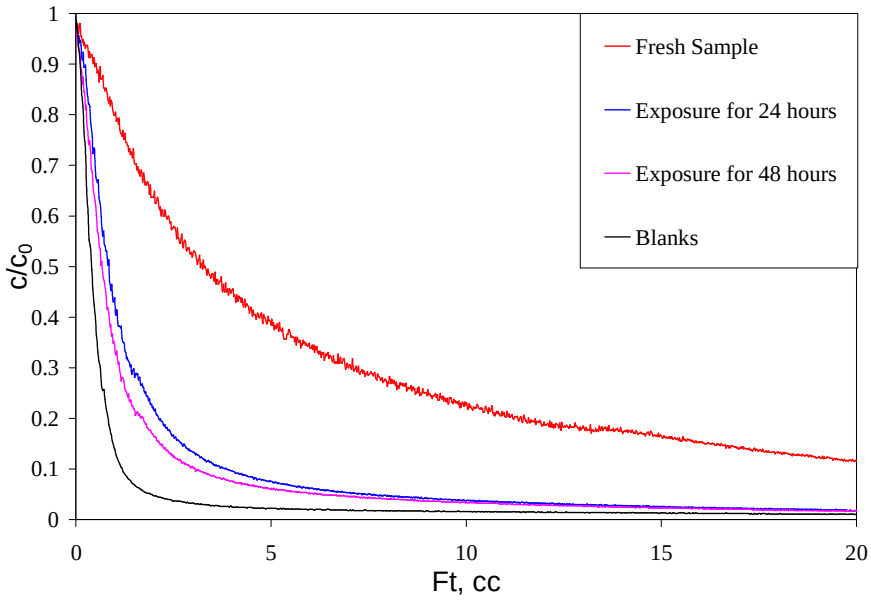

Figure 7.18 Mg/DOBDC stability results after exposure to wet (1% v/v water) flue gas.

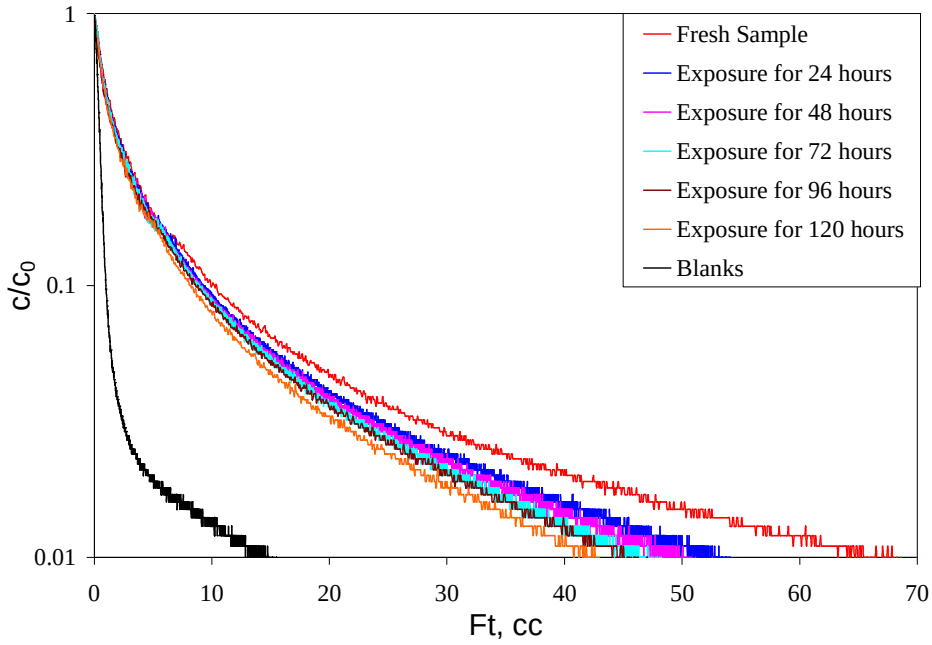

Figure 7.19 13X pellet stability results after exposure to wet (1% v/v water) flue gas.

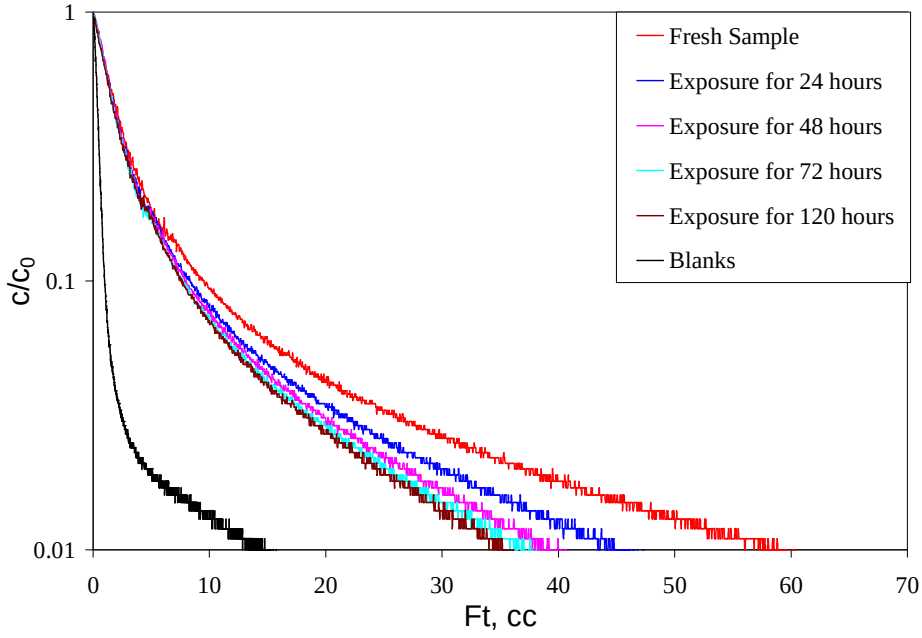

Figure 7.20 13X powder stability results after exposure to wet (1% v/v water) flue gas.

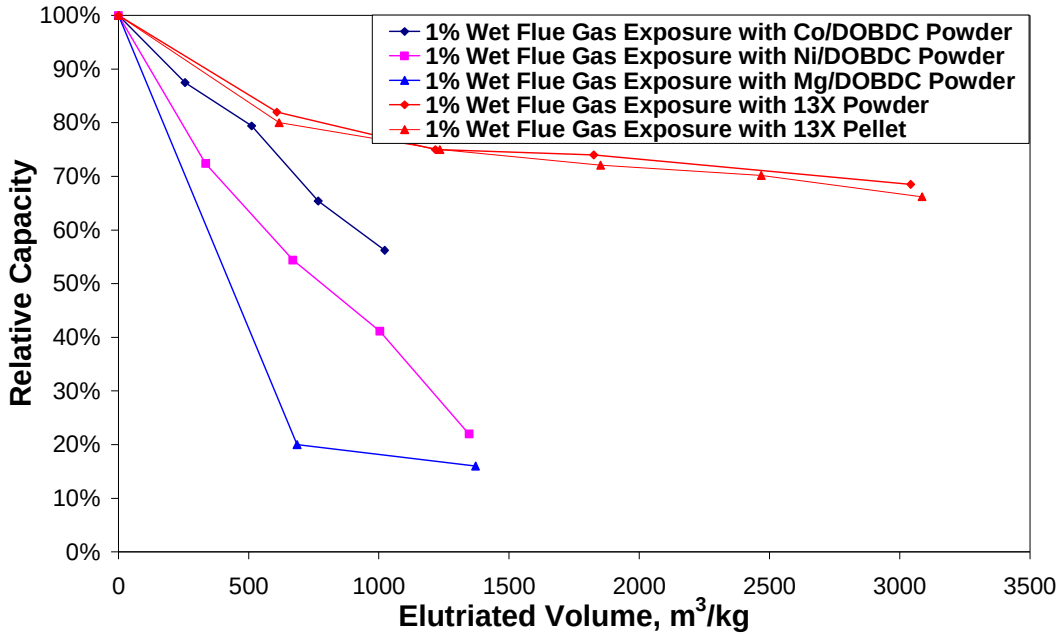

Figure 7.21 Comparison of the stability tests with wet (1% v/v water) flue gas.

Figure 7.21 shows the comparison of the wet flue gas effects on CO_2 adsorption for M/DOBDC powders and 13X zeolite. What is interesting from these results is the fact that the three M/DOBDC MOFs behave very differently in terms of stability, the ranking in terms of stability to the wet flue gas follows the inverse order of the capacity for CO_2, i.e. Co/DOBDC > Ni/DOBDC > Mg/DOBDC. Since in the ZLC CO_2 capacity ranking measurements Mg/DOBDC sample showed large capacity and the fresh sample also confirmed that this material is the best material for carbon capture, but additional ZLC experiments in simulated flue gas suggest that Mg/DOBDC is more moisture and acid sensitive than the other two M/DOBDC MOFs. Ni/DOBDC showed linear capacity decay in the wet flue gas stability test. Co/DOBDC shows better performance but it has a very peculiar change in isotherm shape after the first exposure. For the reference zeolite sample, it is obvious that flue gas does not affect CO_2 adsorption for 13X as much as it does for MOFs; it only

showed some loss of capacity after the first exposure, followed by a slow secondary decay. These results indicated that even if MOFs have good pure CO_2 adsorption capacity at the POI, in order to use them in a real flue gas it will be essential to remove water before the CO_2 capture step.

Besides the comparable CO_2 capacity between the Ni/DOBDC and the benchmark zeolite at the POI, the small water effect together with an easier regeneration process suggests that Ni/DOBDC may have a promising future in CO_2 capture from flue gas.

7.4.5 SO_2 analysis

In order to understand the flue gas effect better, the analysis was also focused on the phenomena during the exposure to the flue gas. Figure 7.22 shows a typical monitored MS signal for Co/DOBDC sample during exposure. Figure 7.23 shows the MS signal for the second exposure. For strong adsorbed species like H_2O and SO_2, the ZLC is behaving like a normal breakthrough apparatus. What is important is to compare the SO_2 signal for the first treatment and for the second and subsequent ones.

The slow breakthrough of SO_2 response in the first exposure indicates that SO_2 is clearly adsorbed on the Co/DOBDC sample, the same sample shows an immediate breakthrough in the second case. It seems that the sample changes the pore openings and does not allow SO_2 to diffuse into the solid after the first treatment, the blockage happened inside the adsorbent with slower mass transfer of SO_2. This could also

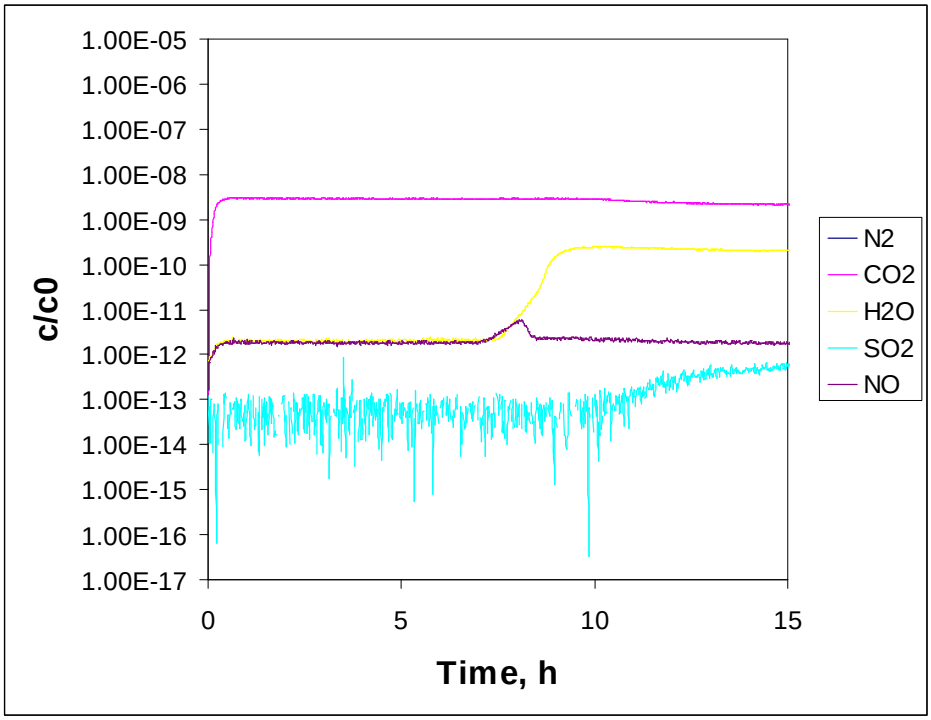

Figure 7.22 MS monitored signal during 1st 24h wet flue gas exposure on Co/DOBDC.

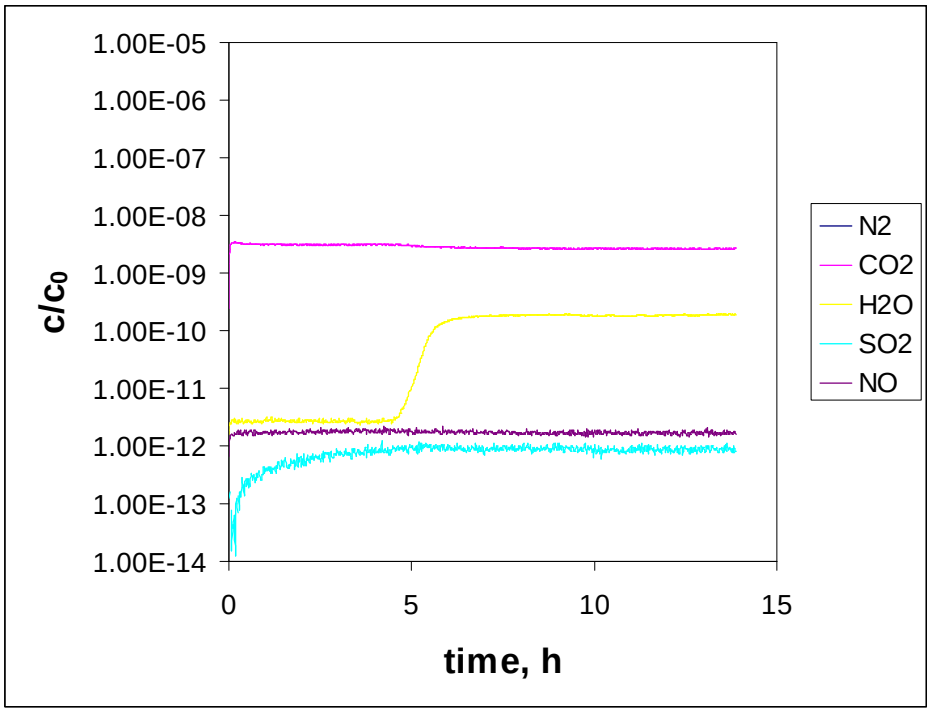

Figure 7.23 MS monitored signal during 2nd 24h wet flue gas exposure on Co/DOBDC.

explain the change in shape of the ZLC (Figure 7.16). Another possibility is that an irreversible metal salt formed between the metal site and SO_2. These effects would explain why subsequent treatments only induce minor reductions in the CO_2 capacity.

Since the ZLC is behaving like a normal breakthrough apparatus in this case, the first moments (mean residence time) analysis was applied to the SO_2 breakthrough curve (i.e. Figure 7.22 and 7.23) for the three M/DOBDC MOF samples using equation 3.27, which is related the adsorption capacity. For Co/DOBDC, it is clear in Figure 7.24 that there is a very sharp reduction after the first exposure. However, in the case of Ni/DOBDC (Figure 7.25), the SO_2 capacity follows a similar trend as the CO_2 capacity. In Mg/DOBDC (Figure 7.26), a clear reduction of SO_2 capacity is shown as well.

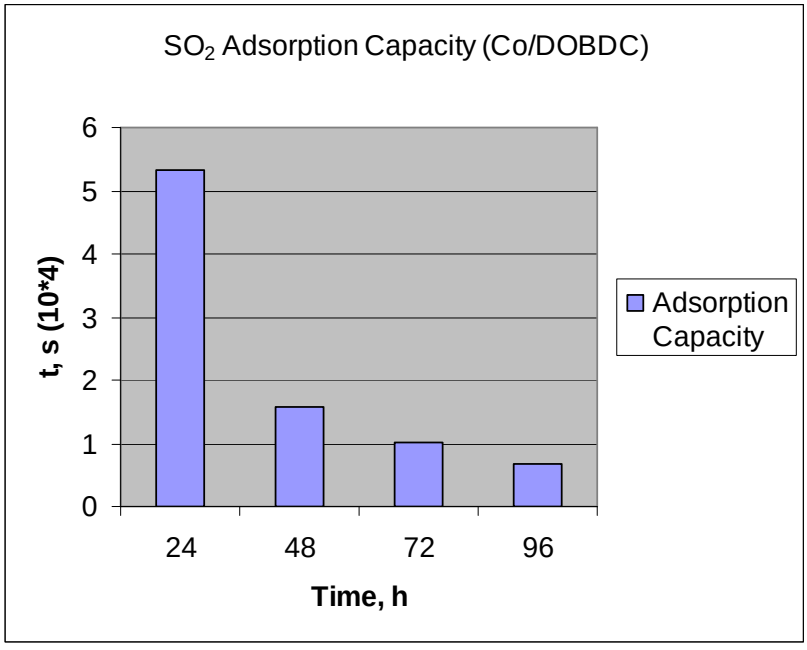

Figure 7.24 moment analysis on SO_2 breakthrough curves for Co/DOBDC during long time wet flue gas exposure.

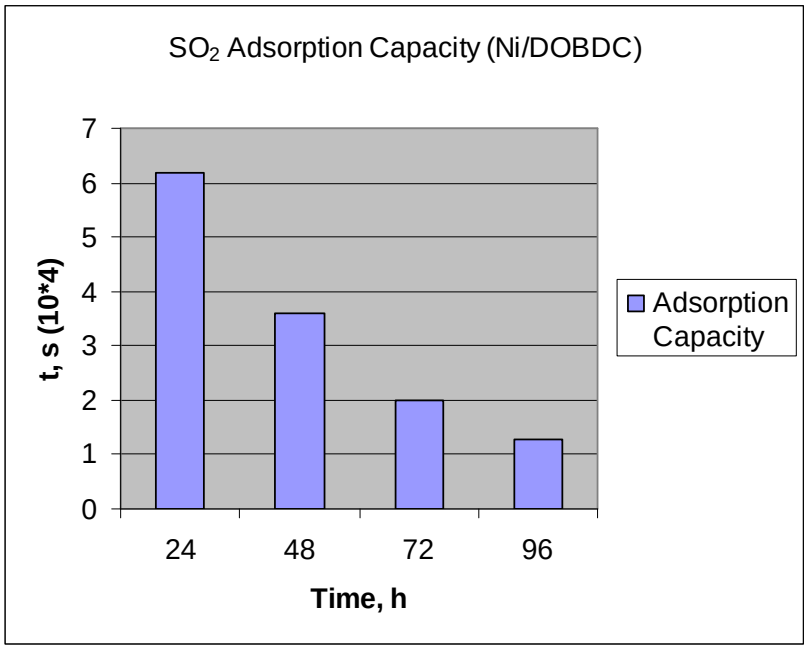

Figure 7.25 moment analysis on SO_2 breakthrough curves for Ni/DOBDC during long time wet flue gas exposure.

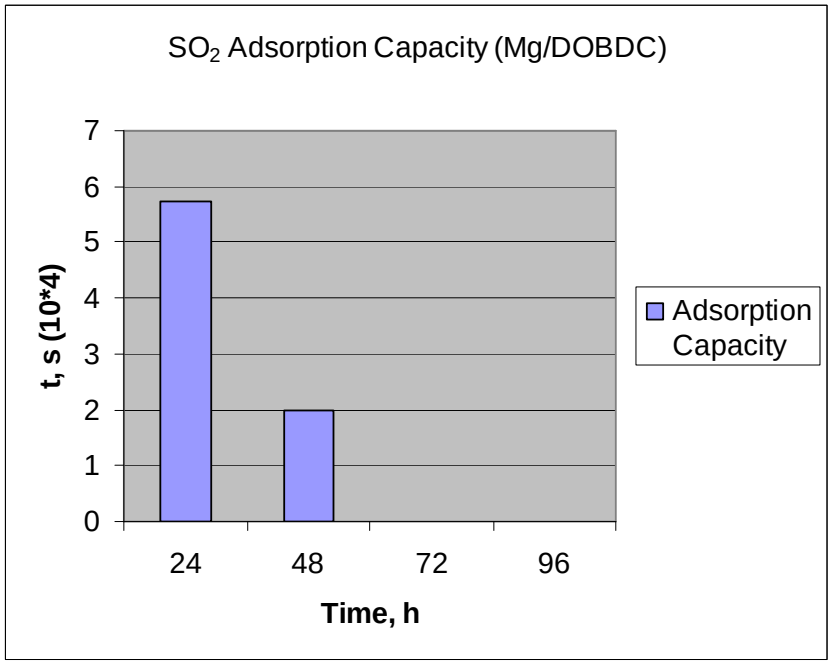

Figure 7.26 moment analysis on SO_2 breakthrough curves for Mg/DOBDC during long time wet flue gas exposure.

7.4.6 XRD characterisation

The ZLC columns treated with the wet flue gas were sealed and sent to our collaborate partner UOP for further characterisation. Powder samples were analyzed by X-ray diffraction (XRD) to determine the purity of the freshly activated sample as well as the effect of flue gas.

The typical XRD patterns shown in Figure 7.27 give the comparison of fresh activated Mg/DOBDC and the sample after being exposed to wet flue gas for a long time. The significant reduction in peak intensity for samples exposed to the flue gas compared to the fresh activated sample indicates changes in the crystal structure. This confirms the reason of the CO_2 capacity reduction after the exposure experiment compared to the original sample.

7.5 Conclusion

The ZLC system has been shown to be extremely useful when trying to accelerate the deactivation of samples due to SO_X and NO_X impurities. Compared to traditional breakthrough experiments or real plant data, the treatment by ZLC can be repeated in situ, use a relatively simple way to interpret results and use a very small sample, and screen the adsorbents stability. This has shown that the technique is a key tool in the screening of novel adsorbents for carbon capture applications. The experiment of stability test shows a lack of stability of M/DOBDC in the presence of impurities.

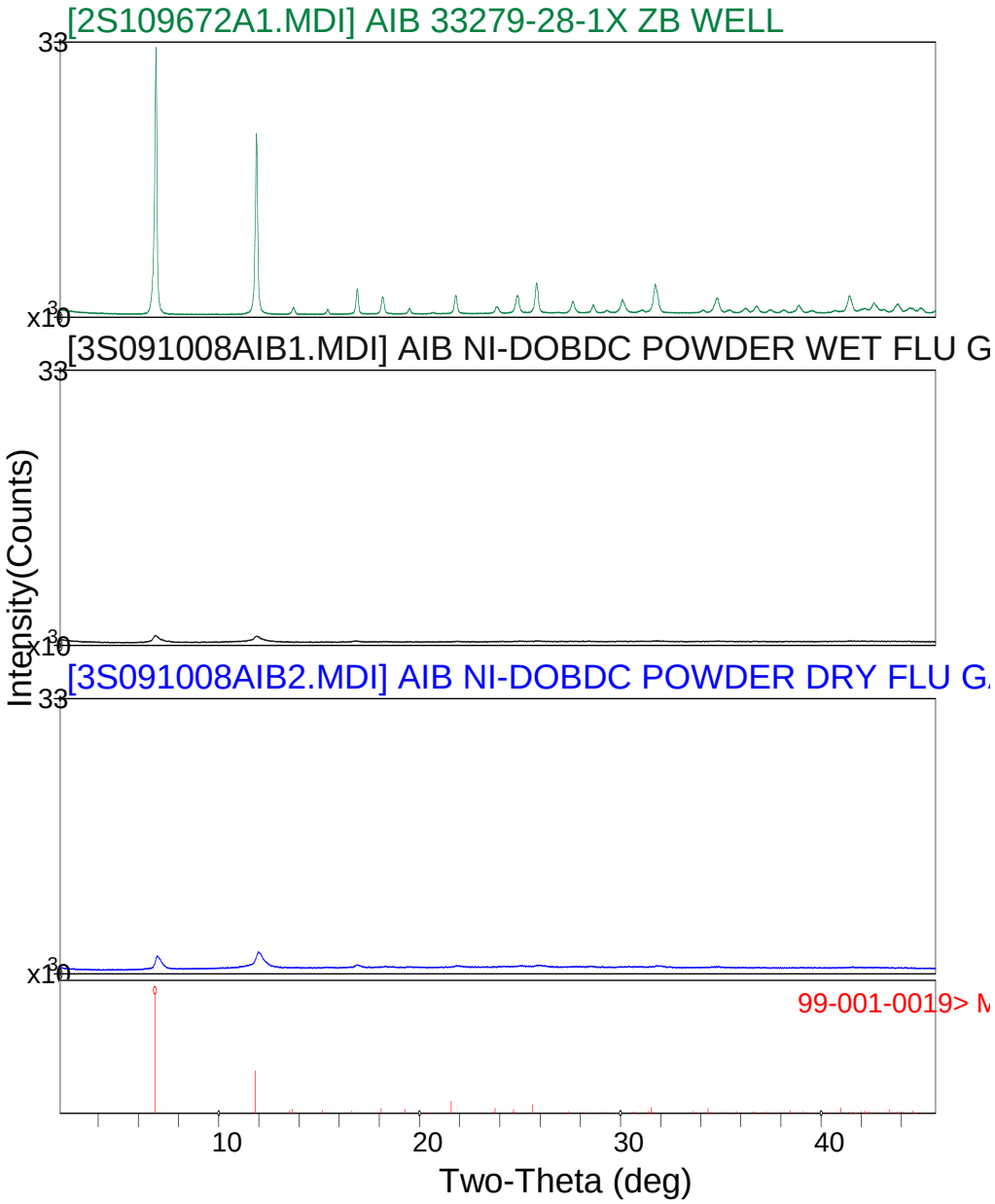

Figure 7.27 XRD spectra for Mg/DOBDC original sample (up), exposed to 1% wet flue gas at 38ºC, 3cc/min for 72h (mid), and exposed to <<1% water at 38 ºC, 3cc/min for 72h (down).

CHAPTER 8

8. CONCLUSIONS AND FURTHER WORK

The dissertation presents a new ZLC system that was designed and set up to deliver all the features used for rapid screening of adsorbents for CO_2 capture applications:

- Rank CO_2 capacity of materials rapidly
- Use only small samples
- Interpret the results easily
- Determine kinetics
- Test the materials with water
- Test the materials with SO_x and NO_x

The key features of the new apparatus that was developed are: the use of 5-15 mg of sample and a dual detector system – a thermal conductivity detector (TCD) for single component measurements and a mass spectrometer for studying the influence of water and other impurities. Improvements over previous ZLC apparatuses include:

5. Extension to lower flowrates, i.e. < 3 cc/min, thereby reducing consumption of gases and allowing to run the system under equilibrium control conditions;
6. A new gas dosing system that allows the use of vapours without a chilled bath and bubbler system;
7. A new switching valve system, which prevents leakages;
8. Automated series of experiments, which are implemented using Labview.

The key characteristics for a good adsorbent should be good sorption properties (capacity, kinetics, selectivity,), low energy requirement for regeneration, good thermal and oxidative stability, tolerance to contaminants, and low cost. The new ZLC technique was first applied to provide rapid screening capacity ranking of more than 15 MOF materials from the open literature and three typical zeolites for carbon capture. At the point of interest for flue gas application (38°C, 0.1 bar CO_2 partial pressure), Mg/DOBDC was found to outperform significantly all other MOFs and benchmark zeolites at the point of interest in low pressure physisorption of CO_2. This has confirmed the literature results carried out on a traditional gravimetric system. The CO_2 capacity at the POI for Mg/DOBDC powder is larger than that of Ni/DOBDC and also the larger isosteric heat of adsorption. The ZLC was also used to investigate steaming on Ni/DOBDC as well as see the effect of forming powders into pellets.

The new ZLC system also enables one to measure micropore and macropore diffusivity. Experiments were carried out on both powders and pellets of typical MOFs and zeolites. For Co/DOBDC crystals, since the system it close to equilibrium control even at the highest flow rate, a low limit of diffusivity can be estimated. For all the formed samples of Ni/DOBDC and 13X pellets, the results indicate that mass transfer is controlled by macropore diffusion. The ZLC technique can also estimate realistic void fraction and tortuosity values for the pellets.

The new ZLC technique was applied to study the stability on the MOF M/DOBDC series. The preliminary water tests showed that all M/DOBDC samples are highly hydrophilic. Therefore in a process design using these MOFs, we conclude that there is a needs to use a guard bed layer to adsorb water or use a gas drying unit before the CO_2 capture section of the plant.

The ZLC system appears to be extremely useful to accelerate the deactivation of samples due to SO_X and NO_X impurities. The key advantages are based on the fact that the treatment can be repeated in situ, in a relatively simple way using a very small sample. The results show that in the presence of impurities and water the candidate MOFs undergo significant deactivation. The Ni based material shows the best resistance to degradation. This result indicates further that there would be a need for a drying unit prior to the carbon capture adsorption process.

A major conclusion of this study is that the ZLC technique can be a key tool in the screening of novel adsorbents for carbon capture applications, since it can be used to

investigate equilibrium, kinetic and stability characteristics of new materials for post-combustion carbon capture conditions.

Based on the results presented in this study, further work will be focused on:

1. Developing further the automation of the system and include an analysis tool to interpret experimental results.
2. Extend the use of ZLC to other classes of adsorbents. At lower concentrations, i.e. carbon capture for gas fired power plants, chemisorption will be important and the use of the ZLC to determine also reaction kinetics information is a new area of research that should be pursued.
3. Extend the use of the automation of the system to allow also the use larger columns to study breakthrough curves.
4. Apply the new ZLC system to multi-component mixtures.

References

1. Yu, K.M.K., et al., *Recent Advances in CO2 Capture and Utilization.* ChemSusChem, 2008. **1**(11): p. 893-899.

2. Pachauri, R.K.a.R., A., *Contribution of Working Groups I, II and III to the Fourth Assessment Report of the Intergovernmental Panel on Climate Change.* Retrieved from http://www.ipcc.ch/publications_and_data/ar4/syr/en/contents.html, 2007. **Fourth Assessment Report**: p. 104.

3. IEA, *IEA CO2 Emissions Update 2010.* 2011.

4. International Energy Agency, *World Energy Outlook 2007—Executive Summary; Head of Communication and Information Office, France; .* 2007.

5. Ciferno, J.P., et al., *Capturing Carbon from Existing Coal-Fired Power Plants.* Chemical Engineering Progress, 2009. **105**(4): p. 33-41.

6. Granite, E.J. and H.W. Pennline, *Photochemical Removal of Mercury from Flue Gas.* Industrial & Engineering Chemistry Research, 2002. **41**(22): p. 5470-5476.

7. Jörg Kärger, D.M.R., *Diffusion in zeolites and other microporous solids.* 1992.

8. Aaron, D. and C. Tsouris, *Separation of CO₂ from Flue Gas: A Review.* Separation Science and Technology, 2005. **40**(1): p. 321 - 348.

9. Mitsubishi, *Mitsubishi's carbon capture technology* Carbon Capture Journal, 2007: p. 1-5.

10. Himeno, S., T. Komatsu, and S. Fujita, *High-Pressure Adsorption Equilibria of Methane and Carbon Dioxide on Several Activated Carbons.* Journal of Chemical & Engineering Data, 2005. **50**(2): p. 369-376.

11. Aris, R., *Mathematical Modeling.* 1999: p. 15.

12. Rege, S.U. and R.T. Yang, *A novel FTIR method for studying mixed gas adsorption at low concentrations: H2O and CO2 on NaX zeolite and [gamma]-alumina.* Chemical Engineering Science, 2001. **56**(12): p. 3781-3796.

13. R. Bredesen, T.A.P., *Membrane Technology, Vol. 2 (Eds.: K.-V. Peinemann, S. Pereira Nunes), Wiley-VCH, Weinheim, pp. 217.* 2008.

14. Steeneveldt, R., B. Berger, and T.A. Torp, *CO2 Capture and Storage: Closing the Knowing-Doing Gap.* Chemical Engineering Research and Design, 2006. **84**(9): p. 739-763.

15. Harrison, D.P., *Greenhouse Gas Control Technologies 7, 2, 1101*. 2005.

16. D.M. Ruthven, S.F.a.K.K., *Pressure Swing Adsorption, VCH Publishers, New York, NY.* 1994.

17. Ruthven, D.M. and R. Kumar, *An Experimental Study of Single-Component and Binary Adsorption Equilibria by a Chromatographic Method.* Industrial & Engineering Chemistry Fundamentals, 1980. **19**(1): p. 27-32.

18. Ruthven, D.M.F., S.; Knaebel, K. S., *Pressure Swing Adsorption, New York, NY.* 1994: p. 352.

19. Zhao, D., et al., *Characteristics of the synthetic heulandite-clinoptilolite family of zeolites.* Microporous and Mesoporous Materials, 1998. **21**(4-6): p. 371-379.

20. AtlasDatabase, *Retrieved from http://www.iza-structure.org/databases/*.

21. Montanari, T. and G. Busca, *On the mechanism of adsorption and separation of CO2 on LTA zeolites: An IR investigation.* Vibrational Spectroscopy, 2008. **46**(1): p. 45-51.

22. Hernández-Huesca, R., L. Díaz, and G. Aguilar-Armenta, *Adsorption equilibria and kinetics of CO2, CH4 and N2 in natural zeolites.* Separation and Purification Technology, 1999. **15**(2): p. 163-173.

23. Wang, H., et al., *Flowrate correction for the determination of isotherms and Darken thermodynamic factors from Zero Length Column (ZLC) experiments.* Adsorption, 2011. **17**(4): p. 687-694.

24. Harlick, P.J.E. and F.H. Tezel, *An experimental adsorbent screening study for CO2 removal from N2.* Microporous and Mesoporous Materials, 2004. **76**(1-3): p. 71-79.

25. Siriwardane, R.V., et al., *Adsorption of CO2 on Molecular Sieves and Activated Carbon.* Energy & Fuels, 2001. **15**(2): p. 279-284.

26. Siriwardane, R.V., et al., *Adsorption of CO2 on Zeolites at Moderate Temperatures.* Energy & Fuels, 2005. **19**(3): p. 1153-1159.

27. Inui, T., Y. Okugawa, and M. Yasuda, *Relationship between properties of various zeolites and their carbon dioxide adsorption behaviors in pressure swing adsorption operation.* Industrial & Engineering Chemistry Research, 1988. **27**(7): p. 1103-1109.

28. Merel, J., M. Clausse, and F. Meunier, *Experimental Investigation on CO2 Post Combustion Capture by Indirect Thermal Swing Adsorption Using 13X and 5A Zeolites.* Industrial & Engineering Chemistry Research, 2007. **47**(1): p. 209-215.

29. Calleja, G., J. Pau, and J.A. Calles, *Pure and Multicomponent Adsorption Equilibrium of Carbon Dioxide, Ethylene, and Propane on ZSM-5 Zeolites with Different Si/Al Ratios.* Journal of Chemical & Engineering Data, 1998. **43**(6): p. 994-1003.

30. Gallei, E. and G. Stumpf, *Infrared spectroscopic studies of the adsorption of carbon dioxide and the coadsorption of carbon dioxide and water on CaY- and NiY-zeolites.* Journal of Colloid and Interface Science, 1976. **55**(2): p. 415-420.

31. Brandani, F. and D.M. Ruthven, *The Effect of Water on the Adsorption of CO2 and C3H8 on Type X Zeolites.* Industrial & Engineering Chemistry Research, 2004. **43**(26): p. 8339-8344.

32. Ertan, A. and F. Çakicioğlu-ÖZkan, *CO2 and N2 Adsorption on the Acid (HCl, HNO3, H2SO4 and H3PO4) Treated Zeolites* Adsorption, 2005. **11**(0): p. 151-156.

33. Menendez, J.A., et al., *On the Modification and Characterization of Chemical Surface Properties of Activated Carbon:In the Search of Carbons with Stable Basic Properties.* Langmuir, 1996. **12**(18): p. 4404-4410.

34. Choi, S., J.H. Drese, and C.W. Jones, *Adsorbent Materials for Carbon Dioxide Capture from Large Anthropogenic Point Sources.* ChemSusChem, 2009. **2**(9): p. 796-854.

35. Zelenak, V., et al., *Amine-modified ordered mesoporous silica: Effect of pore size on carbon dioxide capture.* Chemical Engineering Journal, 2008. **144**(2): p. 336-342.

36. Li, H., et al., *Design and synthesis of an exceptionally stable and highly porous metal-organic framework.* Nature, 1999. **402**(6759): p. 276-279.

37. Yaghi, O.M. and H. Li, *Hydrothermal Synthesis of a Metal-Organic Framework Containing Large Rectangular Channels.* Journal of the American Chemical Society, 1995. **117**(41): p. 10401-10402.

38. Ferey, G., *Hybrid porous solids: past, present, future.* Chemical Society Reviews, 2008. **37**(1): p. 191-214.

39. Tranchemontagne, D.J., et al., *Secondary building units, nets and bonding in the chemistry of metal-organic frameworks.* Chemical Society Reviews, 2009. **38**(5): p. 1257-1283.

40. Ma, S., et al., *Metal-Organic Framework from an Anthracene Derivative Containing Nanoscopic Cages Exhibiting High Methane Uptake.* Journal of the American Chemical Society, 2007. **130**(3): p. 1012-1016.

41. Rowsell, J.L.C., et al., *Hydrogen Sorption in Functionalized Metal Organic Frameworks.* Journal of the American Chemical Society, 2004. **126**(18): p. 5666-5667.

42. Rowsell, J.L.C. and O.M. Yaghi, *Effects of Functionalization, Catenation, and Variation of the Metal Oxide and Organic Linking Units on the Low-Pressure Hydrogen Adsorption Properties of Metal Organic Frameworks.* Journal of the American Chemical Society, 2006. **128**(4): p. 1304-1315.

43. Millward, A.R. and O.M. Yaghi, *Metal Organic Frameworks with Exceptionally High Capacity for Storage of Carbon Dioxide at Room Temperature.* Journal of the American Chemical Society, 2005. **127**(51): p. 17998-17999.

44. Bourrelly, S., et al., *Different Adsorption Behaviors of Methane and Carbon Dioxide in the Isotypic Nanoporous Metal Terephthalates MIL-53 and MIL-47.* Journal of the American Chemical Society, 2005. **127**(39): p. 13519-13521.

45. Dybtsev, D.N., et al., *Microporous Manganese Formate:A Simple Metal Organic Porous Material with High Framework Stability and Highly Selective Gas Sorption Properties.* Journal of the American Chemical Society, 2003. **126**(1): p. 32-33.

46. Natesakhawat, S., et al., *Adsorption Properties of Hydrogen and Carbon Dioxide in Prussian Blue Analogues M3[Co(CN)6]2, M = Co, Zn.* The Journal of Physical Chemistry C, 2006. **111**(2): p. 1055-1060.

47. Prestipino, C., et al., *Local Structure of Framework Cu(II) in HKUST-1 Metallorganic Framework:鈥?Spectroscopic Characterization upon Activation and Interaction with Adsorbates.* Chemistry of Materials, 2006. **18**(5): p. 1337-1346.

48. Britt, D., et al., *Highly efficient separation of carbon dioxide by a metal-organic framework replete with open metal sites.* Proceedings of the National Academy of Sciences of the United States of America, 2009. **106**(49): p. 20637-20640.

49. Caskey, S.R., A.G. Wong-Foy, and A.J. Matzger, *Dramatic Tuning of Carbon Dioxide Uptake via Metal Substitution in a Coordination Polymer with Cylindrical Pores.* Journal of the American Chemical Society, 2008. **130**(33): p. 10870-10871.

50. Demessence, A., et al., *Strong CO2 Binding in a Water-Stable, Triazolate-Bridged Metal Organic Framework Functionalized with Ethylenediamine.* Journal of the American Chemical Society, 2009. **131**(25): p. 8784-8786.

51. Yazaydin, A.O., et al., *Enhanced CO2 Adsorption in Metal-Organic Frameworks via Occupation of Open-Metal Sites by Coordinated Water Molecules.* Chemistry of Materials, 2009. **21**(8): p. 1425-1430.

52. Bae, Y.-S., et al., *Carborane-based metal-organic frameworks as highly selective sorbents for CO2 over methane.* Chemical Communications, 2008(35): p. 4135-4137.

53. Demessence, A., et al., *Strong CO2 Binding in a Water-Stable, Triazolate-Bridged Metal-Organic Framework Functionalized with Ethylenediamine.* Journal of the American Chemical Society, 2009. **131**(25): p. 8784-8786.

54. Farrusseng, D., et al., *Heats of Adsorption for Seven Gases in Three Metal-Organic Frameworks: Systematic Comparison of Experiment and Simulation.* Langmuir, 2009. **25**(13): p. 7383-7388.

55. Park, K.S., et al., *Exceptional chemical and thermal stability of zeolitic imidazolate frameworks.* Proceedings of the National Academy of Sciences, 2006. **103**(27): p. 10186-10191.

56. Han, S.S., S.-H. Choi, and A.C.T. van Duin, *Molecular dynamics simulations of stability of metal-organic frameworks against H2O using the ReaxFF reactive force field.* Chemical Communications. **46**(31): p. 5713-5715.

57. Kaye, S.S., et al., *Impact of Preparation and Handling on the Hydrogen Storage Properties of Zn4O(1,4-benzenedicarboxylate)3 (MOF-5).* Journal of the American Chemical Society, 2007. **129**(46): p. 14176-14177.

58. Wang, Q., et al., *CO2 capture by solid adsorbents and their applications: current status and new trends.* Energy & Environmental Science, 2011. **4**(1): p. 42-55.

59. Eic, M. and D.M. Ruthven, *A new experimental technique for measurement of intracrystalline diffusivity.* Zeolites, 1988. **8**(1): p. 40-45.

60. Brandani, S. and D.M. Ruthven, *Analysis of ZLC desorption curves for gaseous systems.* Adsorption-Journal of the International Adsorption Society, 1996. **2**(2): p. 133-143.

61. Brandani, S., M.A. Jama, and D.M. Ruthven, *ZLC Measurements under non-linear conditions.* Chemical Engineering Science, 2000. **55**(7): p. 1205-1212.

62. Ruthven, D. and F. Brandani, *ZLC Response for Systems with Surface Resistance Control.* Adsorption, 2005. **11**(1): p. 31-34.

63. Brandani, S., et al., *Heat effects in ZLC experiments.* Adsorption-Journal of the International Adsorption Society, 1998. **4**(3-4): p. 275-285.

64. Brandani, F., D. Ruthven, and C.G. Coe, *Measurement of Adsorption Equilibrium by the Zero Length Column (ZLC) Technique Part 1:Single-Component Systems.* Industrial & Engineering Chemistry Research, 2003. **42**(7): p. 1451-1461.

65. Ruthven, D.M. and Z. Xu, *Diffusion of oxygen and nitrogen in 5A zeolite crystals and commercial 5A pellets.* Chemical Engineering Science, 1993. **48**(18): p. 3307-3312.

66. al, B.e., *Transport Phenomena.* 1960.

67. Cavenati, S., C.A. Grande, and A.E. Rodrigues, *Adsorption Equilibrium of Methane, Carbon Dioxide, and Nitrogen on Zeolite 13X at High Pressures.* Journal of Chemical & Engineering Data, 2004. **49**(4): p. 1095-1101.

68. Mofarahi, M., et al., *Design of CO2 absorption plant for recovery of CO2 from flue gases of gas turbine.* Energy, 2008. **33**(8): p. 1311-1319.

69. Karl, T.R. and K.E. Trenberth, *Modern Global Climate Change.* Science, 2003. **302**(5651): p. 1719-1723.

70. Keeling, C.D., et al., *Interannual extremes in the rate of rise of atmospheric carbon dioxide since 1980.* Nature, 1995. **375**(6533): p. 666-670.

71. Yazaydin, A.O., et al., *Screening of Metal-Organic Frameworks for Carbon Dioxide Capture from Flue Gas Using a Combined Experimental and Modeling Approach.* Journal of the American Chemical Society, 2009. **131**(51): p. 18198-18199.

72. Rosi, N.L., et al., *Rod Packings and Metal-Organic Frameworks Constructed from Rod-Shaped Secondary Building Units.* Journal of the American Chemical Society, 2005. **127**(5): p. 1504-1518.

73. Wong-Foy, A.G., A.J. Matzger, and O.M. Yaghi, *Exceptional H2 Saturation Uptake in Microporous Metal Organic Frameworks.* Journal of the American Chemical Society, 2006. **128**(11): p. 3494-3495.

74. Dietzel, P.D.C., et al., *An In Situ High-Temperature Single-Crystal Investigation of a Dehydrated Metal–Organic Framework Compound and Field-Induced Magnetization of One-Dimensional Metal–Oxygen Chains.* Angewandte Chemie International Edition, 2005. **44**(39): p. 6354-6358.

75. Yazaydn, A.O., et al., *Screening of Metal-Organic Frameworks for Carbon Dioxide Capture from Flue Gas Using a Combined Experimental and Modeling Approach.* Journal of the American Chemical Society, 2009. **131**(51): p. 18198-18199.

76. Zhao, Z., Z. Li, and Y.S. Lin, *Adsorption and Diffusion of Carbon Dioxide on Metal Organic Framework (MOF-5).* Industrial & Engineering Chemistry Research, 2009. **48**(22): p. 10015-10020.

77. Skoulidas, A.I., *Molecular Dynamics Simulations of Gas Diffusion in Metal Organic Frameworks:Argon in CuBTC.* Journal of the American Chemical Society, 2004. **126**(5): p. 1356-1357.

78. Babarao, R. and J. Jiang, *Diffusion and Separation of CO2 and CH4 in Silicalite, C168 Schwarzite, and IRMOF-1: A Comparative Study from Molecular Dynamics Simulation.* Langmuir, 2008. **24**(10): p. 5474-5484.

79. Duncan, W.L. and K.P. Moller, *The effect of a crystal size distribution on ZLC experiments.* Chemical Engineering Science, 2002. **57**(14): p. 2641-2652.

Nomenclature

c = fluid-phase sorbate concentration (mol/m^3)

c_0 = initial fluid-phase sorbate concentration (mol/m^3)

C = total molecular density (mol/m^3)

D = intracrystalline diffusion coefficient (m^2/s)

D_0 = corrected diffusivity, defined by eq 6 (m^2/s)

D_m = molecular diffusivity (m^2/s)

F = volumetric fluid flow of the purge fluid (cm^3/min)

K = dimensionless Henry's adsorption constant

L = dimensionless ZLC parameter

q = adsorbed-phase sorbate concentration (mol/m^3)

q^* = adsorbed-phase sorbate in the solid (mol/m^3)

R = sorbent particle radius (m)

t = time (s)

V_s = volume of the solid in the ZLC cell (m^3)

V_g = volume of the gas in the ZLC cell (m^3)

y = mole fraction in the gas phase

β = roots of Eq 3.7

γ = ratio of the fluid capacity for the sorbate to that of sorbent

ε_P = the void fraction of the pellet

τ = the tortuosity of the macropores